The effects of surface cooling on the stability of a flat-plate boundary layer in subsonic flow

MSc thesis

Kristie Goorden

22 December 2023

Delft University of Technology
Faculty of Aerospace Engineering
Department of Flow Physics and Technology

Author: Kristie Goorden
Chair: Prof. dr. Marios Kotsonis
Daily supervisor: Dr. Theo Michelis

To Madelief, who has taught me more than any research ever could.

Acknowledgement

There is no such thing as an individual project, but if one project were to come close, it would not be this one.

There is a colossal group of people that I am lucky to thank for the help and support that they have given me over the course of my thesis work. First of all, I thank my daily supervisor Theo for the fact that he was, indeed, a daily supervisor to me. I wonder if he knows how much it helped me, that his door was usually open in the literal sense, so that I did not even have to knock. His approachability reaches further than an invite to ask lots of questions though; there was always room to talk about something other than physics, too. In case of a setback, he had a surprisingly effective way of comforting me with the words 'all in good time', either said out loud or some other way. And to make me laugh, which may eventually be the most important thing we do in life. To anyone who reads this and has a choice of thesis supervisor ahead of them: pick Theo.

Secondly, I would like to thank my chairman Marios for his catching enthusiasm for all things transitioning. He has stirred my interest for the subject of boundary layers even more since I started this project with him. Moreover, I want to compliment him on the unique way in which he manages his research group. The atmosphere and friendships among all staff and students are most definitely a result of his efforts and style, and I realize how lucky I am to have been part of them for a while.

It is only a short jump from there to everyone else who I have been working (simultaneously) with in the Low Speed Laboratory, all of whom I am very grateful to for their openness. I have seldom felt so welcome in a place full of strangers, which it quickly ceased to be. It soon became the wondrous place where incredible ambition and endless complaining go hand in hand, and in spite of the crazy hours, everybody somehow manages to take care of their colleagues as well. It was warm and fuzzy and I hope you know that I have the utmost respect for you all.

Outside of the lab, I was in good hands with my housemates and friends. Special thanks to Liesbeth, Barbara, Maura, Suze, Lies and Diede for putting up with me during the crucial moments at home, and to Kirsten for the beautiful equilibrium of pep talks and laments that we shared on the campus lawns. I owe a great deal of thanks to both my sisters, who were there for me at the other end of the line, day and night. Nothing compares to the certainty that someone will always pick up. Marjolijn, although forever young at heart, possesses a kind of wisdom by which she never fails to comfort me. And then we laugh. Pia is the type of sister that would drop everything to show up at your doorstep in a glimpse, when you let her know something is wrong. And then we laugh again.

All this being said, I am well aware that the only people without whom none of this would be possible, are my parents. They have loved me, cheered me on and encouraged me to keep on striving for what I want most, for all these years. I know they are proud of me, but I am mostly proud to be their daughter.

I conclude by thanking my dear friend Madelief, who could not see the end of this project. How I wish she was here to celebrate it, as that was her astonishing talent. I am grateful for everything she has taught us about life, although there was only so much that we managed to understand.

And to whoever is up there with her, thank you for the music.

Abstract

The transition behaviour of a boundary layer with zero pressure gradient in a low-subsonic freestream is examined for a set of wall temperatures below the freestream temperature. Solutions of the boundary layer provided by both an incompressible and a compressible numerical flow solver are compared to wind tunnel measurements on a uniformly cooled section of a flat plate. The compressible solver features a temperature dependence of the fluid properties, which proves to be crucial for modeling the stability of a thermal boundary layer. Thermal images of the surface show that the spanwise-averaged transition front moves downstream with decreasing wall-to-freestream temperature ratio. At the streamwise station where no frictional heating due to turbulent structures is observed, T-S waves are detected in the measured velocity fluctuation profiles. The experimental data show good correspondence with the numerical linear stability predictions here. Further downstream, where streaks of transition occur, T-S waves can no longer be distinguished, and it is likely that non-linear effects have overtaken the boundary layer flow here. The absolute amplitude and the amplitude growth rate of the velocity perturbations both decrease with the wall temperature in the region where T-S waves are seen, and even more in the non-linear region. It is concluded that uniform surface-cooling stabilizes the boundary layer on a flat plate in an incompressible freestream, but a variable-fluid property solver is required to model the stability characteristics.

Contents

List of Figures

List of Tables

Nomenclature

Greek symbols

α	complex streamwise wavenumber
α_i	wave amplification factor
α_r	real streamwise perturbation wavenumber or mode
β	complex spanwise wavenumber
β_H	Hartree parameter
δ^*	boundary layer displacement thickness
δ_{99}	99% boundary layer thickness
η	wall normal distance in boundary layer thickness units (y/δ_{99})
λ	wavelength
μ	dynamic viscosity
ω	angular wave frequency
ϕ	stream function
ψ	amplitude function
ρ	density
τ	shear stress
ε	convergence error

Letters

A	wave amplitude
a	speed of sound
b	span
c_r	wave phase velocity
D_f	friction drag
e	Euler's number
f	frequency
k	conductive heat transfer coefficient
L	flatplate length
m	Falkner-Skan similarity parameter
N	amplitude growth rate or N-factor
p	pressure

s	arbitrary streamwise coordinate
T	temperature
t	time
u	velocity in streamwise direction
V	voltage
v	velocity in wall-normal direction
w	velocity in spanwise direction
x	streamwise distance from the flat-plate leading edge
y	wall-normal distance from the flat-plate surface
z	spanwise distance from the flat-plate mid-line
Pr	Prandtl number
Re	Reynolds number

Subscripts and superscripts

$\bar{(\ )}$	non-dimensional parameter
$(\ )^+$	wall coordinate
$(\ )_0$	at the leading edge
$(\ )_w$	at the wall ($y = 0$)
$(\ )_\infty$	in the freestream
$(\ )_{\mathrm{aw}}$	for an adiabatic wall
$(\ )'$	perturbation quantity

1 Introduction

CO_2-emissions as a consequence of kerosene-fuelled aviation are estimated to increase by 2% per year in the three decades ahead [1]. This growth is due to the increasing demand for and access to air transport [2] and exists despite the aircraft efficiency improvements anticipated by the ICAO in the years to come [3].

Hydrogen appears to be a promising alternative to kerosene, as its specific energy is about three times higher than that of Jet A [4] and its combustion products contain no CO_2. However, the use of hydrogen as an aviation fuel has two major disadvantages in terms of storage. Firstly, tank walls should be able to withstand its high volatility. Moreover, the required tank volume is large due to the very low density of H_2 at flight conditions. The envisioned solution is cryogenic storage, where the gas is compressed and stored in liquid form (below 20.46 K, commonly referred to as LH_2). In this state, the required volume for an equal amount of energy is about four times larger with respect to kerosene [5]. The cryogenic state of course imposes new heavy requirements on the fuel tank, but there is an additional benefit: when expanded back to a its gaseous state before combustion inside the aircraft, the H_2 will decrease in temperature and could therefore serve as a coolant for aerodynamic surfaces. Researchers expect, that surfaces cooled below the temperature of the in which an aircraft moves, will reduce the drag it experiences.

This concept was first introduced by Reshotko [6] and by Brewer et al. [7]–[9] in the late 1970's and further developed by Cunnington & Parmley [10] shortly after. Their publications conclude the following:

- for all favorable pressure gradients and for adverse pressure gradients op to an upper limit (depending on the chord Reynolds number), the transition Reynolds number shows an inverse relation with the ratio of wall to freestream temperature (T_w/T_e), according to the current models;
- the transition Reynolds numbers found in wind tunnel experiments of cryogenic wall cooling are up to a factor 10 smaller than model predictions at the same temperature ratio, which is most likely due to the noise level and turbulence intensity of the tunnel flow;
- for a classic aircraft design, fuselage wall cooling is not profitable, as the added cooling system weight will be larger than the fuel weight saving: it is recommended to cool only the wings, and thus it suffices to focus on wing geometries in future research on the concept;
- taken into account the weight of the envisioned storage, cooling and propulsion system, the approach is expected to improve the lift-to-drag ratio in cruise by 27%, leading to fuel savings between 15% and 27.8%;
- the effect of compressible three-dimensional flow phenomena, predominantly crossflow, is not taken into account in the current models and should be further investigated in order to validate these outcomes.

In summary, introducing a surface cooling system in hydrogen aircraft seems to be a viable concept. However, before diving deeper into the designs of such systems, it should be established that surface cooling does, in fact, lower the drag forces experienced by a body in a fluid flow, and to what extent. It has been shown in many works before, that a laminar boundary layer induces a higher drag coefficient than a turbulent one. The question therefore is really, does surface cooling cause the boundary layer's transition to turbulence to move downstream?

From a theoretical viewpoint, this was well argued before the conceptual studies of Reshotko and his fellow researchers were carried out. Linear stability theory, describing how small perturbations of the velocity are amplified in the linear region of a boundary layer, were used to predict the point of to breakdown into turbulence. Lees and Lin [11], [12] and Schubauer and Skramstad [13] published early works on the theory in the second half of the 1940s. A prediction method for transition to turbulence resulting from these plublications, was set up by Van Ingen [14] in 1956 and later extended to different flow types by himself and others. Mack [15] provided a summary of the state of the art of stability theory in 1984, which is still highly adequate today.

Linear stability was validated in experiments on flat plates subject to heating [16], [17], suction and blowing [18], [19], [20] and hypersonic freestreams [21], [22]. Missing from the body of work is an experimental study in which the plate is steadily cooled to below the freestream temperature in a subsonic flow, the combination that would hold for the hydrogen-cooled aircraft under cruise conditions.

As a first attempt to fill this gap, an experimental study of the boundary layer stability on a cooled flat plate is presented in the current work. The experiment was conducted in the Low Speed Laboratory of TU Delft. The outcomes are used to validate a numerical model previously designed by the research group. The case of the flat plate is intended to asses the suitability of the numerical model in its current state to predict the stability of a boundary layer on an internally cooled structure. It should lay the groundwork for future research cases, moving closer toward the boundary layer on a cooled aircraft wing at cruise altitude, entailing updates to the numerical model in each step.

A formulation of the current research problem follows from the theoretical framework summarized in chapter 2, and is presented in its last section. The numerical model as well as the experimental setup used to achieve the established research are described in detail in chapter 3 and chapter 4, respectively. The results are presented and discussed in chapter 5. Chapter 6 lists the conclusions drawn from these results. Finally, an evaluation of the current work yielding recommendations for future research, is discussed in chapter 7.

2 Background

A summary is given of the theoretical physics behind the expected behaviour of airflow over of a cooled flat plate, as well as the numerical and experimental work done so far to validate the theory. Section 2.1 outlines how the drag of a body is influenced by viscosity and the laminar-to-turbulent transition location on its surface. The relation of this transition location to the amplification of flow perturbations, known as linear stability theory, is presented in section 2.2. Sections 2.3 and 2.4 treat previous quantitative research to validate the stability theory in a numerical and experimental way, respectively. Finally, the current research goals derived from the remaining knowlegde gap are presented in section 2.5.

2.1 Mechanisms of viscous drag

The fuel consumption of any aircraft depends on its weight and the drag forces that act on it. The main contributors to the overall drag are the form drag due to the size and shape of the body, lift-induced drag and skin friction drag (or viscous drag). Since for an existing aircraft the first two generally cannot be altered, the focus lies on lowering the viscous drag with fuel savings in mind. Viscous drag is directly caused by the existence of a boundary layer between surface and freestream, due to the no-slip condition which dictates that the velocity at the wall equals 0. The relation between the drag force working on a body and its boundary layer are roughly governed by two characteristics of the latter: the boundary layer thickness and the nature of the flow inside it. The thicker the layer, the larger the surface of the body normal to the mean flow direction virtually becomes. The influence of the laminar or turbulent nature of the boundary layer is treated in the subsection that follows.

2.1.1 The influence of viscosity and laminar-turbulent transition on skin friction

Skin friction on a body's surface exists by the virtue of the viscosity of the fluid through which it moves. The viscous drag of a surface equals the integral of the wall shear stress over that surface, in the case of a two-dimensional flow:

$$D_f = b \int \tau_w(s) ds, \tag{1}$$

where s represents the streamwise coordinate. The wall shear stress τ_w depends on the viscosity and the slope of the velocity profile at the wall:

$$\tau_w = \left[\mu \frac{\partial u}{\partial y} \right]_w \tag{2}$$

It can be seen directly from equation 2 that τ_w increases with viscosity, i.e., a lower viscosity of the fluid results in a smaller drag force. For a gas, the viscosity decreases when the gas is cooled down. This means that a decrease of wall shear stress, and thus of friction drag, can be achieved by subtraction of heat from a gas flow.

A similar relation holds for the aerodynamic heating rate at the wall. The higher the temperature gradient in y-direction at the wall, the more heat is transferred in the opposite direction: $\not{q} = -k(\partial T/\partial y)_w$. A non-adiabatic, cooled wall offers the possibility for heat to flow through the surface, away from the boundary layer. This counteracts the effect of aerodynamic heating, and therefore prevents heat accumulation that would cause a rise in viscosity at the surface.

However, not only the diminution of viscosity contributes to viscous drag reduction. As can be noted from the formula for wall shear stress given above, a higher mean velocity gradient at the wall causes a higher shear stress. This high gradient, corresponding to a fuller velocity profile in the near-wall region, is typical of turbulent boundary layer flow. In other words, a turbulent boundary layer in a gas flow with the same viscosity causes the viscous drag to be larger than for a laminar boundary layer.

For the total boundary layer over an aerodynamic surface, this means that the larger the laminar portion, the lower the viscous drag (c.f. equation 1). It is therefore advantageous to delay the transition front in space. Subsection 2.2.4 elaborates further on ways to accomplish this.

2.1.2 Compressibility effects on pressure drag

In the case of compressible flow, an assumption that may well be valid in cruise [23], the effects of wall-cooling point in the same direction as for the incompressible case. Theoretical research of the compressible case dates back to the 1960s. An analytical investigation was carried out by Ball [24], based on similarity solutions for a laminar boundary layer with adverse pressure gradient. It shows that the boundary layer becomes thinner when cooled, from which a drag reduction follows through the (two-dimensional) displacement thickness principle [25]. Moreover, the boundary layer's reverse flow-portion was shown to decrease with decreasing wall temperature, inducing a pressure differential caused by flow separation, and thereby reducing the viscous drag. Shortly after the publication of Ball's work, research began to focus not so much on the reduction of viscous drag or pressure drag as a whole, but rather on the spatial delay of laminar-turbulent transition in the boundary layer.

2.2 Linear stability theory

The transition to turbulence is marked by instability of the flow: a lack of its resistance to local disturbances, so that these are no longer damped out but able to grow in the streamwise direction. Disturbances with respect to the mean flow occur in a boundary layer due to various factors of receptivity, such as surface roughness and small variations in fluid properties. The characteristics of the behaviour of small disturbances are described by linear stability theory. One application of this theory is to determine the Reynolds number at which a flow becomes unstable, i.e. its critical Reynolds number[1].

2.2.1 Governing equations of boundary layer stability

The theory of boundary layer stability departs from the Navier–Stokes equations (1822–1850), in which the velocity components, pressure, temperature and density are superimposed by their mean and small perturbation values. With the introduction of normal mode solutions

$$[u', v', w', p', T', \rho']^T = [\tilde{u}(y), \tilde{v}(y), \tilde{w}(y), \tilde{p}(y), \tilde{T}(y), \tilde{\rho}(y)]^T \exp[i(\alpha x + \beta z + \omega t], \tag{3}$$

a single fourth-order equation is obtained to represent the perturbed flow. The observation that the instabilities having the lowest critical Reynolds number for a given perturbation wavelength in an incompressible shear flow are indeed two-dimensional was later proven to be valid for all incompressible shear flows and became known as Squire's theorem [27]. For the two-dimensional incompressible case, where the spanwise components of the velocity and wavenumber vectors are both zero, the fourth-order equation reduces to the eigenvalue problem known as the Orr–Sommerfeld equation (1907–1908). The incompressible Orr–Sommerfeld problem is treated in subsection 2.2.3.

When compressibility is taken into account, the perturbation quantities in equation 3 remain to be described by a system of five equations, given in non-dimensional form in Appendix A. A distinction can be made between temporal and spatial amplifications of the modes. If the perturbations have complex frequency ω, it can be concluded that a positive imaginary part $\omega_i > 0$ indicates a temporally amplified wave. Spatial amplification of perturbation waves can be described for α and β chosen complex, so that a two-dimensional steady flow where $\beta = \omega = 0$ leaves only the positive amplification factor $-a_i > 0$ to indicate instability. It is because of this convenient simplification that the spatial theory is maintained throughout the current work.

For any stability problem given a certain base flow, the amplification factor can be plotted against the Reynolds number to determine the stability of the flow. This has lead to the concept of a curve of neutral stability: the line corresponding to $a_i = 0$ in the plane of Re and any quantity that characterizes the perturbation. (Examples can be found in figure 2.1.) Obviously, the challenge remains to solve for $\varphi(y)$ to allow for the other flow variables to be extracted.

---

[1] Note that some textbooks, c.f. Schlichting [26], use the term *indifference Reynolds number* for marginal amplification. The label of critical Reynolds number is in these reserved for the point of turbulent breakdown.

2.2.2 The role of viscosity

It was discovered already by Prandtl (1904) and Taylor (1915) that viscosity has a destabilizing effect on a boundary layer flow. The simplified boundary layer equations for a flat plate in a steady, compressible flow show the influence of the viscosity gradient in wall-normal direction through the x-momentum equation (4b).

$$\frac{\partial}{\partial x}(\rho u) + \frac{\partial}{\partial y}(\rho v) = 0 \tag{4a}$$

$$\rho\left(u\frac{\partial u}{\partial x} + v\frac{\partial u}{\partial y}\right) = -\frac{\partial p}{\partial x} + \frac{\partial}{\partial y}\left(\mu\frac{\partial u}{\partial y}\right) \tag{4b}$$

$$-\frac{\partial p}{\partial y} = 0 \tag{4c}$$

The boundary conditions read:

$$y = 0 : \qquad u = v = 0, \qquad\qquad y = \infty : \qquad u = U_\infty \tag{5}$$

Tollmien [28] supplemented the work of Lord Rayleigh [29] by proving that a point of inflection in the subsonic boundary layer velocity profile—i.e. a point y_s where $\left[\partial^2 u/\partial y^2\right]_{y_s}$ changes sign—is not only a necessary, but a sufficient condition for instability to occur. A compressible extension to the inflection point criterion can be stated as follows:

$$\left[\frac{\partial}{\partial y}\left(\rho\frac{\partial u}{\partial y}\right)\right]_{y_s} = 0, \tag{6}$$

provided that $u(y_s) > U_\infty - a_\infty$ [11]. Both are however inviscid effects: in the presence of an inflection point, the flow will become unstable regardless of friction forces. The influence if viscosity on the stability of a flow is explained by Heisenberg's criterion for the incompressible case [30]: for any neutral perturbation with finite wavelength and non-zero phase velocity that exists in an inviscid fluid (the infinite Reynolds number limit), a perturbation of that same wavelength is unstable in the real fluid for a finite Reynolds number. The criterion is extended to compressible flows as follows [12]: a subsonic, neutral perturbation of non-zero wavelength in an inviscid compressible flow, would be unstable in a viscous compressible flow at a finite Reynolds number.

A change in viscosity brought on by cooling of the fluid, though, may have a significant effect on the stability. Assuming variable viscosity, the curvature of the velocity profile at the wall can be expressed as follows:

$$\left(\frac{\partial^2 U}{\partial y^2}\right)_{y=0} = \left[-\frac{1}{\mu}\frac{\partial \mu}{\partial y}\frac{\partial U}{\partial y}\right]_{y=0} \tag{7}$$

The viscosity increases with temperature, so for $T_w < T_\infty$, the viscosity gradient in y will be positive. Given that the velocity gradient is also positive, it is concluded that the curvature of the profile is negative at the cooled wall. Since the curvature is known to remain negative as $y \longrightarrow \infty$, no point of inflection has to occur throughout the profile.

Viscous instabilities may also occur when there is no inflection point in the boundary layer profile. However, the viscous instability generally has a higher critical Reynolds number and a smaller amplification rate. The neutral curves for two types of instabilities are drawn in the α, Re-plane in figure 2.1.

It was Schlichting who expressed the amplification factor of the most amplified mode in terms of the Reynolds number for a Blasius boundary layer in 1933 [26]. This resulted in the curve of neutral stability that is obtained by plotting the Reynolds number for zero amplification against (a function of) the perturbation frequency. The two characteristics that stand out from the curve, are 1) that is has two distinct branches and 2) that both branches reach an asymptotic value as $Re_x \longrightarrow \infty$. This observation sparked efforts to establish asymptotic solutions to the Orr–Sommerfeld problem. These solutions are treated in the next section of this chapter.

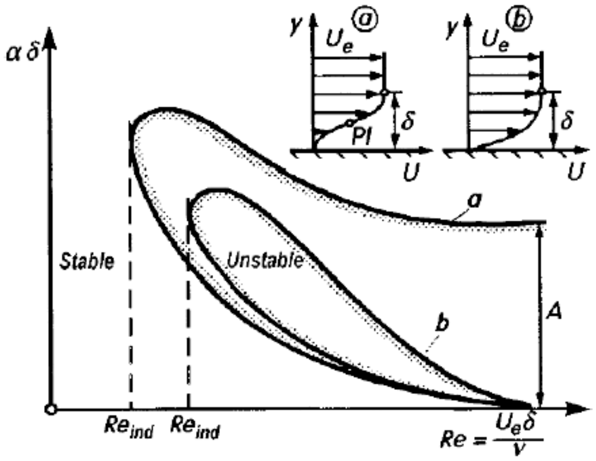

Figure 2.1: The shapes of the curve of neutral stability for (a) an inviscid instability and (b) a viscous instability without point of inflection [26]

2.2.3 Onset of boundary layer transition: the Tollmien-Schlichting wave

When the Reynolds number exceeds its critical value, the initial disturbances with respect to the base flow are no longer damped out. The various types of amplified instabilities that may occur as a consequence can be either two-dimensional waves (called Tollmien–Schlichting or T–S waves, after their discoverers [31], [32]) or three-dimensional phenomena (such as crossflow instabilities). As mentioned before, Squire's theorem for incompressible shear flows tells us that the primary instabilities in a plate boundary layer are mostly two-dimensional. Since this literature study supports experimental work on a flat plate in a quasi-two-dimensional flow, it focuses solely on the T–S instability type. Note that for certain wing designs as well as for highly cooled structures, the most unstable disturbance modes may belong to crossflow instabilities [11], [15]. Additionally, at high Mach numbers, supersonic instabilities can dominate the boundary layer transition [15].

T–S waves correspond to the most unstable eigenmode of the velocity perturbations and exist in the linear flow region. At higher Reynolds numbers, non-linear effects take over and eventually, the flow breaks down into turbulence. This process is sketched in figure 2.2.

A T–S wave is essentially a streamwise oscillation of the fluid flow. Unlike the "usual" wave types such as sound waves, in which an oscillation of the pressure is propagated through a medium, a T–S wave entails mass transfer and thus concerns an oscillation of the medium itself. This behaviour can already be recognized in an incompressible flow. Application of the method of small perturbations to the incompressible boundary layer leads to the Orr–Sommerfeld equation. This subsection contains a summary of this derivation, based on the books by Schlichting [26] and Schmid and Henningson [33], and a review article by Mack [15].

Under the parallel-flow assumption, the two-dimensional base flow is given by

$$U(y), \qquad V = W = 0, \qquad P(x, y), \tag{8}$$

and is subject to the perturbations quantities

$$u'(x, y, t), \qquad v'(x, y, t), \qquad p'(x, y, t). \tag{9}$$

These add up to the following total flowfield:

$$u = U(y) + u'(x, y, t), \qquad v = v'(x, y, t), \qquad w = 0, \qquad p = P(x, y) + p'(x, y, t) \tag{10}$$

When plugging these flow quantities into the Navier–Stokes equations and neglecting any second-order perturbation terms (multiplications of two perturbation quantities or their derivatives), the following set

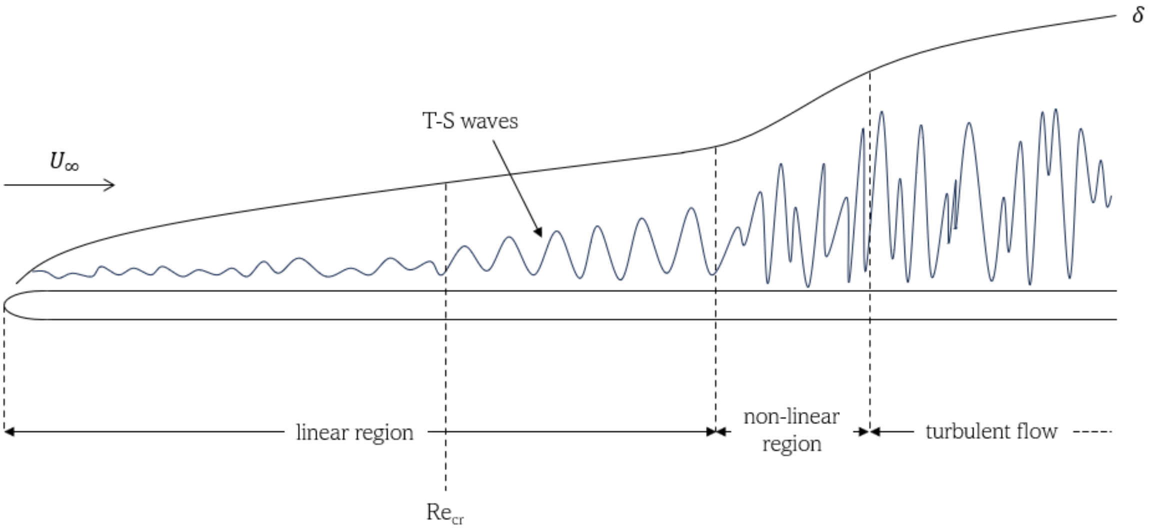

Figure 2.2: Laminar-to-turbulent transition in the boundary layer on a flat plate, where disturbances are generated between the leading edge (left) and Re$_{\text{cr}}$

of equations results:

$$\frac{\partial u'}{\partial x} + \frac{\partial v'}{\partial y} = 0 \tag{11a}$$

$$\frac{\partial u'}{\partial t} + U\frac{\partial u'}{\partial x} + v'\frac{\partial U}{\partial y} + \frac{1}{\rho}\left(\frac{\partial P}{\partial x} + \frac{\partial p'}{\partial x}\right) = \nu\left(\frac{\partial^2 u'}{\partial x^2} + \frac{\partial^2 U}{\partial y^2} + \frac{\partial^2 u'}{\partial y^2}\right) \tag{11b}$$

$$\frac{\partial v'}{\partial t} + U\frac{\partial v'}{\partial x} + \frac{1}{\rho}\left(\frac{\partial P}{\partial y} + \frac{\partial p}{\partial y}\right) = \nu\left(\frac{\partial^2 v'}{\partial x^2} + \frac{\partial^2 v'}{\partial y^2}\right) \tag{11c}$$

The baseflow must satisfy the Navier–Stokes equations too, so that:

$$\frac{1}{\rho}\frac{\partial P}{\partial x} = \nu\left(\frac{\partial^2 U}{\partial y^2}\right) \tag{12a}$$

$$\frac{1}{\rho}\frac{\partial P}{\partial y} = 0 \tag{12b}$$

Subtracting (12a) from (11b) and (12b) from (11c) simplifies the system to

$$\frac{\partial u'}{\partial x} + \frac{\partial v'}{\partial y} = 0 \tag{13a}$$

$$\frac{\partial u'}{\partial t} + U\frac{\partial u'}{\partial x} + v'\frac{\partial U}{\partial y} + \frac{1}{\rho}\frac{\partial p'}{\partial x} = \nu\left(\frac{\partial^2 u'}{\partial x^2} + \frac{\partial^2 u'}{\partial y^2}\right) \tag{13b}$$

$$\frac{\partial v'}{\partial t} + U\frac{\partial v'}{\partial x} + \frac{1}{\rho}\frac{\partial p'}{\partial y} = \nu\left(\frac{\partial^2 v'}{\partial x^2} + \frac{\partial^2 v'}{\partial y^2}\right) \tag{13c}$$

At this point, by way of trial solution to the flow, the stream function ϕ is introduced:

$$\phi(x, y, t) = \varphi(y)e^{i(\alpha x + \omega t)} \tag{14}$$

Note that the amplitude function φ depends only on the wall-normal coordinate y, and that the wave-like behaviour of the disturbance described here corresponds to the normal-mode solution given in (3) with $\beta = 0$. The parameters ω and α now represent the angular frequency and complex wavenumber of the T–S wave, respectively.

The velocity perturbation components can now be expressed in terms of the wave parameters:

$$u'(x, y, t) = \frac{\partial \phi}{\partial y} = \frac{\partial \varphi}{\partial y} e^{i(\alpha x + \omega t)} \tag{15a}$$

$$v'(x, y, t) = -\frac{\partial \phi}{\partial x} = -i\alpha\varphi e^{i(\alpha x + \omega t)} \tag{15b}$$

By inserting these components in the momentum equations (13b) and (13c) and eliminating the pressure terms, the incompressible Orr–Sommerfeld equation is obtained:

$$(U - c)\left(\frac{d^2\varphi}{dy^2} - \alpha^2\varphi\right) - \frac{d^2U}{dy^2}\varphi = -\frac{i\nu}{\alpha}\left(\frac{d^4\varphi}{dy^4} - 2\alpha^2\frac{d^2\varphi}{dy^2} + \alpha^4\varphi\right) \tag{16}$$

where $c = \omega/\alpha$, so that c_r is the phase velocity of the T–S wave in the streamwise direction.

It is now clear to see, that for a given base flow, the amplitude of the disturbances is coupled with the wavenumber. The relation to the Reynolds number appears through the kinematic viscosity ν, and becomes clearer when writing the Orr–Sommerfeld equation in non-dimensional form [26].

In the analysis of a boundary layer flow, either measured or modeled, the shape function is often used to identify the local state of transition. The following definition of the shape function σ is handled here:

$$\sigma(y) = \sqrt{\frac{1}{N}\sum_{i=1}^{N}(u_i')^2} \tag{17}$$

Because a T–S wave is associated with a variation in streamwise velocity, it can easily be recognized in the shape function of a flow. In a (y, σ)-plot, a single-mode perturbation appears as a second peak just above an existing peak near the wall, where the base flow velocity is small so that disturbances are relatively large. See figure 2.3 for an example, where a linear stability model is compared with particle image velocimetry (PIV) data. As soon as the non-linear region is entered and more modes come into play, the plot will deviate from this shape.

2.2.4 Boundary layer control techniques

The first efforts to control the transition process of the boundary layer with the aim of drag reduction date back to the nineteenth century [35]. Since then, numerous flow control methods have been developed. Ways to control a flow are generally divided into two categories: active and passive techniques. The active category includes all mechanisms that require energy input, such as suction or blowing, synthetic jets and plasma actuators. In the light of fuel savings, passive control is therefore preferred. Examples of passive techniques are the placement of vortex generators and of (discrete) roughness elements. Surface cooling requires energy input and is thus classified as active flow control—although this is debatable if a residual flow from the fuel system is used for the cooling.

Many of the methods focus on spatially delaying transition by moving the location of the critical Reynolds number further downstream. Others are concerned with the mitigation of the turbulent boundary layer thickness or the delay or re-attachment of separated flows. Because surface cooling is aimed at transition delay, the other methods are omitted here.

The crux of transition delay is to alter the boundary conditions of the flow such that the solution to the stability problem changes. In the case of suction, the wall-normal velocity at the wall changes from zero (the non-permeability condition) to some negative value. The effects on the stability are comparable to those of a pressure drop: 1) the boundary layer thickness decreases as the mass flow is partly directed through the surface, so that the transition to turbulence happens further downstream, and 2) the velocity profile near the wall changes shape in such a way that the formation of an inflection point is delayed [26]. The asymptotic Bussmann suction profile [36], where the wall-normal velocity component $v_w \sim 1/\sqrt{x}$, the shape factor $H = \delta^*/\theta$ takes on a value of 2. This value is significantly lower than that of a typical

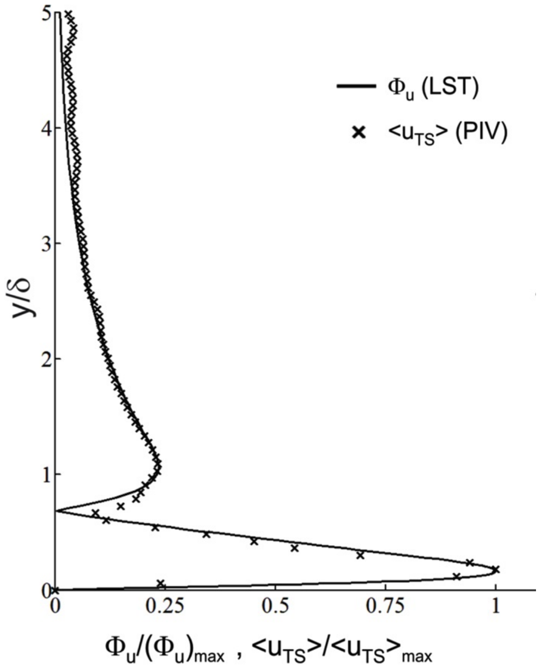

Figure 2.3: Shape function plots, compared for a linear stability model and PIV measurements [34]. The upper, low amplitude peak indicates the presence of a T–S wave.

profile without suction, where $H = 2.59$, and, as a consequence, the location where the Reynolds number is critical lies much further downstream.

The adiabatic wall condition corresponding to a cooled surface has a strong analogy with suction. Through the ideal gas law, $p = \rho RT$, it is readily seen that a decrease in temperature causes an actual pressure drop, causing the boundary layer flow velocity to increase and its thickness to decrease. The influence of a wall temperature below the freestream temperature can therefore be assumed to cause a change in shape factor similar to that of suction. Its relation to the velocity profile and the inflection point criterion was already given in subsection 2.2.2.

2.3 Numerical solutions to the boundary layer and linear stability equations

In order to apply the predictions obtained by linear stability theory to experiments or designs, they will need to be be quantified. This means that the stability equations, either incompressible or compressible, are to be solved. Several methods have been tried out for this, of which the most successful ones are treated here. The selection is restricted to analysis of non-adiabatic walls specifically.

2.3.1 Asymptotic solution for non-adiabatic wall flows

The energy equation complementing the boundary layer equations (4a)–(4b) reads:

$$\rho c_p \left(u\frac{\partial T}{\partial x} + v\frac{\partial T}{\partial y} \right) = \frac{\partial}{\partial y}\left(k\frac{\partial T}{\partial y} \right) + \mu \left(\frac{\partial u}{\partial y} \right)^2 \tag{18}$$

In the case of a non-adiabatic wall with a steady temperature distribution at the wall, additional boundary conditions are introduced:

$$y = \infty : \qquad T = T_\infty \qquad\qquad y = 0 : \qquad T = T_w(x) \neq T_\infty \tag{19}$$

The effect of a non-adiabatic wall condition on the solution to the Orr–Sommerfeld problem can be studied through the influence of a fluid's temperature on its density and viscosity, where, per definition, the variable density implies the assumption of compressibility. Compressible stability cases were widely studied in the 1940s, both theoretically [11], [12] and experimentally [13]. The starting point for the analysis is the same perturbation method that is used for the characterization of T–S waves (see subsection 2.2.3), but applied to the compressible boundary layer equations.

Theoretical investigation pointed out that a trade-off must exist for the non-adiabatic wall: in the case of cooling, the change in distribution of the product of density and vorticity has a stabilizing effect, but the decrease of kinematic viscosity near the wall destabilizes the flow. With the introduction if temperature-dependent viscosity, it can be shown by making use of von Kármán's momentum integral approximation, that surface heating should have a destabilizing effect on the flow and surface cooling causes the opposite [37].

Computations of two-dimensional base flows were initially carried out under the assumption of parallel flow, yielding similarity solutions for the laminar part of the boundary layer. Lees and Lin [11] applied the Squire transformation to the compressible perturbation equations. This greatly simplifies the system under the embedded assumption that the most unstable perturbation mode is two-dimensional. However, they predicted that there is no guarantee that Squire's theorem holds for non-adiabatic walls. Also, when superimposing three-dimensional disturbances on the two-dimensional ones present in the Lees–Lin equations and subsequently simplifying by transformation, the procedure does no longer give a definitive prediction of whether two- or three-dimensional instabilities occur first. Dunn and Lin [38] proposed a simplification by neglecting the viscous dissipation term in the energy equation and subsequently applying a transformation analogous to Squire's, obtaining the so-called Dunn–Lin equations. For adiabatic flows, the Mach number at which three-dimensional disturbances take the upper hand in the transition was found to lie between 1 and 2. It was discovered later, that for highly cooled boundary layers at high subsonic Mach numbers (above $M \approx 0.9$), the most unstable disturbances are indeed three-dimensional [39].

Although useful for the aforementioned discovery, numerical solutions of the flowfield obtained using the parallel flow assumption did not comply very well with the data points found in experiments for high Reynolds numbers—even in the fully laminar region of the boundary layer. The agreement was step-wise improved over time, accounting for non-parallel terms by using various approximations and expansion methods [7], [40]–[43].

Gersten and Herwig [42] developed a reference temperature method to predict the stability of flows for an arbitrary variation of temperature-dependent fluid properties. The quantitative property variation was approximated by a Taylor series expansion. They performed their calculations for low-speed, incompressible flows, and concluded that an overall decrease in temperature of the boundary layer due to wall cooling would result in a lower critical Reynolds number.

This conclusion was somewhat adjusted when Herwig and Schäfer repeated the analysis for the compressible case later on [43]. Now, it was found that the wall-normal viscosity gradient caused by wall cooling has a stabilizing effect. This contradicted the reference temperature as drawn up in [42] and paved the way for a new Taylor series-based variable-property method, now expressing the properties as a function of temperature, pressure and wall-normal coordinate. The researchers succeeded in extending their approximation to all Newtonian fluids by taking only the Prandtl number as the input. This allowed them to identify the nature of the relation between critical Reynolds number and wall-to-freestream temperature, which turned out not to be linear, as assumed by Wazzan et al. [44]. Figure 2.4 shows the theoretical relation found and a comparison with the earlier predictions.

Over the course of the 1980s, the performance of computers caught up with that of the asymptotic heuristic methods. These numerical methods offer room for a different type of improvements than the asymptotic calculations so far.

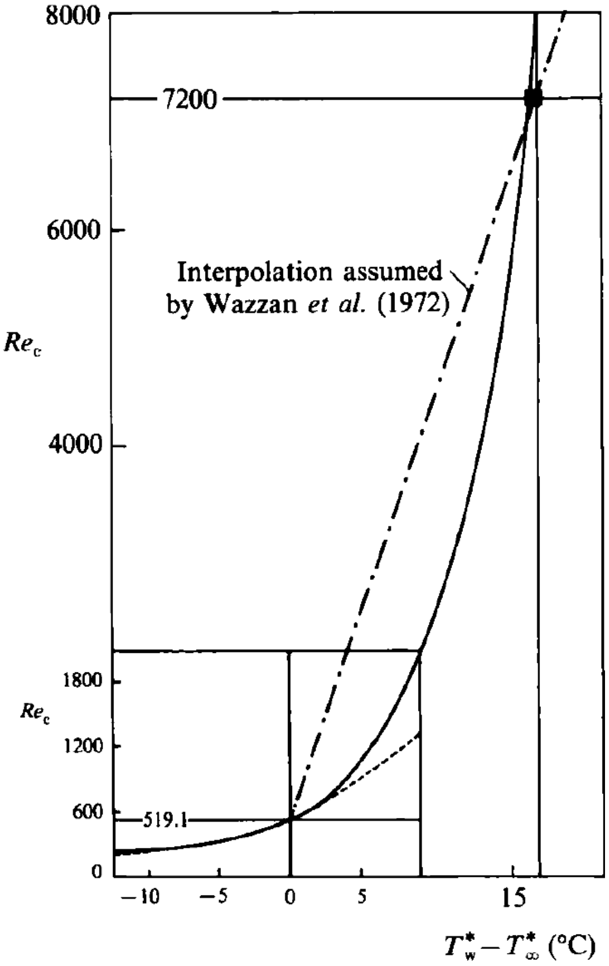

Figure 2.4: Comparison of asymptotic and non-asymptotic results. Dashed line: asymptotic results for $|T_W^* - T_\infty^*|/T_\infty^* \longrightarrow 0$; ■: first data point from Wazzan et al. (1972) [43]

2.3.2 Discrete computational solution methods

Computational codes differ from the asymptotic methods in the sense that they work with discrete spatial and temporal distributions, instead of continuous variables. Also, they are generally of an iterative nature: where the asymptotic procedure directly seeks to leave an error of the smallest possible order, the numerical codes are designed to converge to a solution in multiple steps, reducing the error term in each iteration.

Solving for the stability of a boundary layer flow requires the temperature and velocity components throughout the flowfield as input. It is therefore important to accurately solve the boundary layer equations before looking into the stability. Since they form a parabolic system of differential equations, the boundary layer equations can be numerically solved by means of a finite-difference marching method, as proposed by Schlichting [26]. Because of the characteristic shape of the boundary-layer streamwise velocity profile, the accuracy of the numerical solution is improved by the use of Chebyshev nodes on which the differentiation matrices are set up [45], where the y-coordinates of the nodes are computed by:

$$y_k = \cos\left(\frac{(k-1)\pi}{N-1}\right) \qquad k = 1, 2, ..., N \tag{20}$$

The coordinates, as well as the pseudo-spectral differentiation matrices, are subsequently mapped onto the physical domain $[0, y_i, y_{max}]$ [46]. Using an inflow condition based on a (compressible) Falkner-

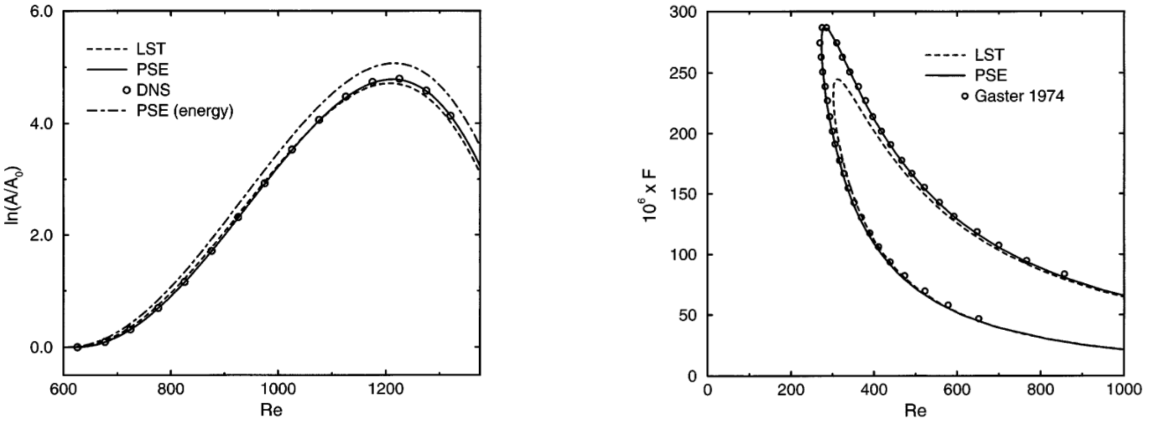

(a) Growth rates for modes with $f = 86 \cdot 10^6$ and different wavenumbers $\beta = \beta^* \nu / U_\infty$ according to PSE (full symbols) and linear stability theory (open symbols). (Data of Bertolotti 1991 [53].)

(b) The neutral curves of the linear stability theory and for non-parallel flow according to PSE and Gaster (1974) [49]. (Data of Bertolotti et al. 1992 [52].)

Figure 2.5: Comparisons of the results obtained by linear stability theory, Gaster's approximation, the parabolized stability equations, and DNS [50]

Skan-Cooke solution with equivalent Hartree parameter, the boundary layer variables can be solved for.

In contrast to the boundary layer system of equations, the Orr–Sommerfeld equation is a fourth-order differential problem. Orszag [47] was the first to successfully set up a numerical method to determine critical Reynolds numbers in Poiseuille flows, using the QR matrix eigenvalue algorithm after Chebyshev collocation (the Chebyshev tau method) [48]. The method proved valid for all nearly-parallel flows. For a flow that is non-parallel, such as a rapidly growing boundary layer, the parabolized stability equations, or PSEs, yield a more accurate result. The parabolic behaviour of the solution to the equations of motion was first pointed out by Gaster [49], who proposed an approximation of the spatial growth rate of instabilities in terms of the group velocity c_g (instead of the usual phase velocity) $\alpha_i \approx -\omega_i / c_g$. This allows for the spatial growth rate to be obtained from ω_i, which can be solved for more easily than the complex quantity α. Gaster subsequently set up a numerical prediction method for the curve of neutral stability via the kinetic energy integral. The PSEs were developed for different flow types by Herbert and several of his colleagues [50]–[52]. Their results overlapped with both DNS (figure 2.5a, see subsection 2.3.3 for more on DNS) and those of Gaster (figure 2.5b).

When deploying the same pseudo-spectral differentiation method used for solving the boundary layer equations [46] in solving the Orr–Sommerfeld equation, the use of clamped boundary conditions—i.e. $u(\pm 1) = u'(\pm 1) = 0$—is recommended [45]. The use of these boundary conditions avoids the emergence of spurious eigenvalues, as happens when using the spectral tau method [54].

We now have a complete numerical model in place to provide us with an unambiguous prediction for the stability of a perturbed boundary layer flow, given any set of velocity and temperature boundary conditions. The validation of the linear-stability based prediction model is discussed in section 2.4. First, the particular case of a non-adiabatic wall of which the temperature is not uniform, is highlighted.

2.3.3 Solutions for non-uniform streamwise temperature distributions

It was discovered in non-adiabatic surface experiments, that the distribution of the wall temperature can be of crucial influence on the boundary layer's stability. A wide variety of heating and cooling equipment configurations has been examined numerically to establish guidelines for their stabilizing or destabilizing effects. The bulk of these models was developed for hypersonic flow, which demonstrates the first signs of transition on a body much further upstream than a low-speed flow would.

In the case of a transitional or turbulent boundary layer, linear stability theory no longer suffices to predict the flow dynamics. Direct numerical simulation (DNS) is a grid-based method to solve the Navier–Stokes equations without assuming a turbulence model. It is therefore that DNS is convenient for the investigation of the most upstream part of the non-linear region, where the character of the non-linearities in usually unknown. Many of the non-uniform temperature, hypersonic models were built using DNS, or a combination of linear stability theory and DNS.

As a general conclusion, it can be stated that a negative streamwise wall temperature gradient can stabilize the boundary layer, but the transition behaviour depends strongly on the placement of the cooling or heating sources. This is illustrated by a few examples. Full-surface, strong cooling of a body in hypersonic flow has a destabilizing effect [22], [54]–[56]. However, when placed at an arbitrary streamwise location in the linear region, a spanwise unrolled cooling strip usually stabilizes the boundary layer flow in its proximity [55]. But when a thin cooling strip is placed just upstream of the instability synchronisation point—the point where the phase speeds of the slow and fast modes synchronize, c.f. [57]—the flow is stabilized, and the same effect is achieved when a heating strip is placed just downstream of the synchronisation point. The longer (in streamwise direction) the cooling strip upstream of the synchronisation point, the more the unstable modes are suppressed, and this mechanism holds for hypersonic flows as well [22], [55].

The effects of a non-uniform temperature distribution on the stability of incompressible flow are not a popular topic of research. This may be due to their relative simplicity: the temperature boundary condition is easily plugged into a linear stability solver.

2.4 Previous experimental work on non-adiabatic boundary layer stability

The accuracy of the numerical methods for solving the stability equations as discussed in the previous section need validation through experiment. Preferably, the influences of all flow conditions are isolated by researching them separately. Flow that can be assumed incompressible over a uniformly cooled or heated surface is therefore treated first. The influence of compressibility and non-uniformity of the wall temperature are discussed in sections 2.4.2 and 2.4.3, respectively.

2.4.1 Uniform heating and cooling of subsonic boundary layers

One of the first profound experimental investigations of the stability of the incompressible boundary layer over a non-adiabatic wall was done by Liepmann and Fila in 1947 [58]. This research confirmed the predictions by Tollmien and Schlichting regarding the point of inflection in a heated boundary layer velocity profile. The experiment was carried out at a very low Subsonic Mach number ($M = 0.024$), so that it is safe to say that no compressibility effects played a role. Boundary layer profiles were measured with hot wires, where the raw measurements were corrected according to a procedure based on King's law [59], accounting for variation of density and thermal conductivity of air with temperature. This procedure is still used today. The criterion of transition handled here, was the first appearance of turbulent bursts detected in the output of an oscilloscope [60]. A plot of the transition Reynolds number against the heated wall temperature is shown in figure 2.6. Note that it concerns higher Reynolds numbers than the critical Reynolds number as discussed in previous sections, since the first instabilities occur in the linear region, where no turbulent bursts exist.

The plot clearly shows an increase in transition Reynolds number as the wall temperature decreases. A quantitative correlation in the form of equation (21) was not concluded, but can be easily derived, since the adiabatic wall temperature in this low-speed experiment is approximately equivalent to the actual wall temperature.

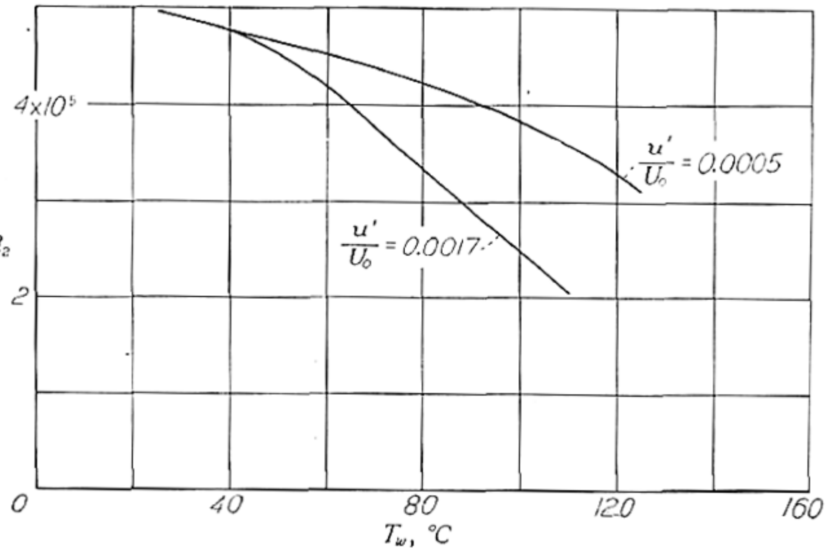

Figure 2.6: Wall temperature dependence of the transition Reynolds number R_2 for a heated flat plate in a freestream of $U_\infty = 8.19$ m/s and $T_\infty \approx 20$ ^{o}C. The upper branch represents the data measured at a freestream turbulence level of $[u'/U_0]_\infty = 0.0005$; the upper branch corresponds to $[u'/U_0]_\infty = 0.0017$ [58].

2.4.2 Uniform heating and cooling of transonic and supersonic boundary layers

The influence that compressibility has on boundary layer stability in practice is to be shown in higher-Mach number experiments. Many of the first experiments involving a wall temperature below freestream temperature were conducted in the hypersonic regime, as a consequence of the discovery that a relatively cold region occurs behind a shock wave. The effect of surface-cooling in this regime turned out to be opposite to the subsonic findings: it destabilizes the flow [21], [22], [46]. An important contribution was that of Bertram et al. (1968) for the NASA Langley Research Center [21], in which several transformations from compressible to constant-density boundary layers were examined for flat plates and delta wings in hypersonic flow. Due to the extreme aerodynamic heating of the boundary layer at high Mach numbers, very low ratios of wall temperature to adiabatic-wall temperature can be reached—provided that powerful wall cooling equipment is at hand. The research showed that even wall temperatures extremely close to stagnation temperature have a minor effect on the skin friction and heat transfer coefficient. These measurements were in a accordance with the then available numerical prediction methods, such as the reference temperature method and the Spalding–Chi correlation, using Coles' transformation theory [61].

In 1980, measurements done on an actively cooled, ten-degree azimuthal angle cone in a large number of subsonic and supersonic wind tunnels were collected by Dougherty and Fisher [62]. They were able to detect linear instabilities: the presence of T–S waves was confirmed by means of microphones. In addition, pitot tubes were used to identify flow transition at the surface. The data from the entire collection were fitted to a curve with approximately 20 percent maximum error. A representation of all these data is given in figure 2.7. The plot shows the relation between the non-adiabatic-to-adiabatic transition Reynolds number and wall temperature. Note that, although the critical Reynolds numbers were obtained in this experiment, they are not included in this figure.

On top of the existence of a curve fit, a surprisingly simple empirical power relation between wall temperature ratio and transition Reynolds number ratio appeared:

$$\frac{Re_{xT}}{Re_{xT,aw}} = \left(\frac{T_w}{T_{aw}}\right)^{-7} \tag{21}$$

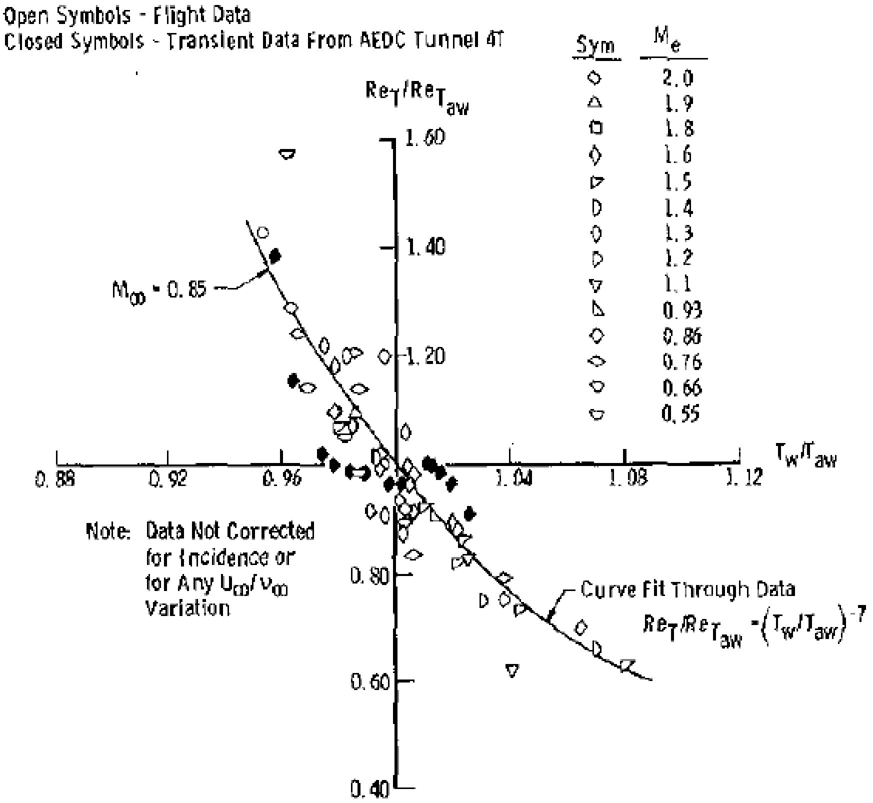

Figure 2.7: Curve fit of collected wind tunnel measurements on a 10-degree cone [62]

It is likely that the accuracy of the quantitative outcomes of wind tunnel research has increased over the years, as measurement techniques have become more refined. On top of that, the experiments on the cone were subject to largely varying turbulence intensities of the freestream.

Over the course of the 2010s, a series of research was carried out in the Cryogenic Lüdwig-Tube at DLR Göttingen to confirm the predicted effect of surface cooling on a flat plate with high measurement accuracy [63]–[65]. Temperature-sensitive paint was used to identify the transition front on the plate. The measurements were done over a range of wall temperature ratios and pressure distributions, both positive and negative. A significant reduction of the transition Reynolds number with decreasing wall temperature ratio was measured. Again, this Reynolds number represents the streamwise location where nonlinearities turn up; the onset of transition will be located further upstream. The results for positive pressure gradients showed good correspondance with the power law found for the cone (eq. 21). Different empirical correlations were established for varying Hartree parameters, however, they all obeyed the aforementioned power law with a certain negative power. The results are plotted and compared to the -7 law in figure 2.8.

The effect of the wall temperature ratio proved to be more pronounced for more favourable pressure gradients, indicating that the effects of the two distinguished quantities cannot be linearly added up. This is an important consideration for the application of the concept to wing surfaces. For the flat plate with (nearly) zero pressure gradient, the measurements were well fitted to a curve with power -4.

The research at DLR was performed in a cryogenic tube. Its measurement procedure entails cooling down of the complete tube including the model, and subsequently running air of a higher temperature through the tunnel. The measurements are short (usually 1 second in total) to avoid unsteady temperature

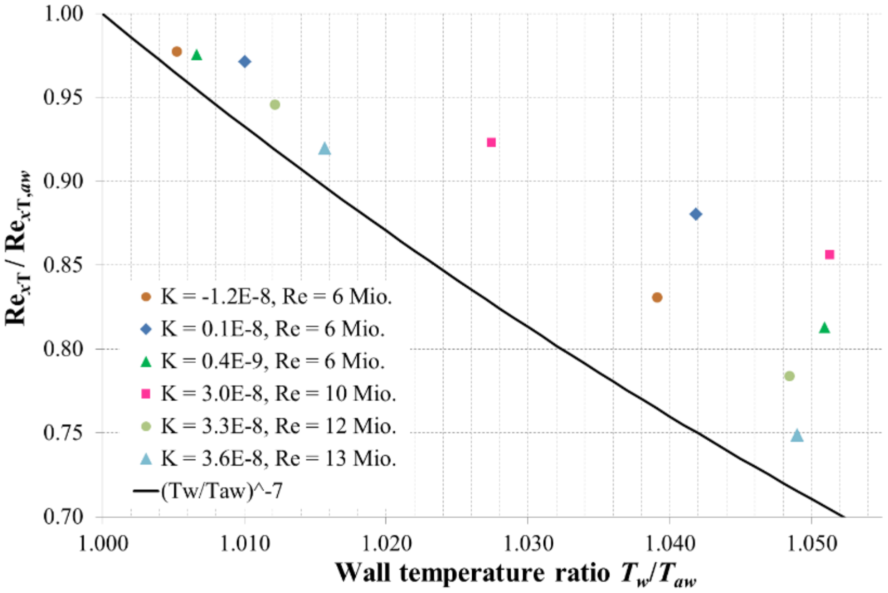

Figure 2.8: Comparison between measurements in the cryogenic Lüdwig-Tube and the power law in equation 21 [63]

effects. This is the reason why temperature-sensitive paint was used: it identifies the transition front in a quick-responding, non-intrusive manner. Velocity profiles and shape functions were not obtained in this research, so that T–S waves could not be identified.

2.4.3 Non-uniform heating and cooling

Similar to the computational research field, non-uniformity of the wall temperature has been a topic of interest in experiments as well. In 1987, a study was published by Landrum and Macha [16], in which they extensively described the behaviour of a locally heated flat plate in an accelerated low-speed flow. Note that the pressure gradient throughout this experiment was non-zero. However, the results gave many intriguing insights in the effects of temperature distribution in incompressible flow. Leading-edge heating, when compared to the adiabatic case where the pressure gradient is still negative, results in spatial delay of the the first T–S waves. In addition, the band of amplified frequencies is narrower, the growth rate smaller and the transition takes place over a longer distance. This result was later confirmed for a zero pressure gradient flat plate [17]. For an insulated (adiabatic) wall in a heated airflow, the boundary layer is stabilized as the insulation is removed on the trailing edge side, due to the relative cooling-down of the wall downstream.

Experimental studies of the effect of a non-uniform temperature distribution on the stability of compressible flow are have not yet been published.

2.5 Reasearch problem and objectives

The theoretical framework behind the stability of the boundary layer on a non-adiabatic surface has been cast into discrete mathematical solvers, which need validation by experiment. Not all numerical models arising from the theory have yet been put to the test, and the knowledge gaps are scattered over a wide range of flow types. The simplest of the not yet validated flow models is that of the steady, two-dimensional, subsonic boundary layer flow over a uniformly cooled flat plate. (Note that some experimental data is available for the unsteady and heated cases.)

It is a attempted to validate this model in the current research by answering the following research question:

What is the effect of steady, uniform wall cooling on the stability of the boundary layer on a flat plate in a subsonic flow?

The research goal is twofold: to answer the question above by means of an experiment, and to validate whether the available numerical models correctly predict the behaviour of the flow as observed in the experiment.

The analysis focuses on three distinctive aspects:

1) the agreement between the expected and observed flow phenomena involved in the boundary layer's transition to turbulence;

2) the influence of compressibility effects on the boundary layer's behaviour, and the resulting necessity to take these effects into account in a computational model;

3) the consequences of a wall heat flux for the practicalities of the experiment, and for the retrieved data and post-processing routine.

3 Numerical approach

The flowfield is approximated by a mathematical model created in MATLAB. The code solves for the boundary layer equations first; the obtained solution serves as input for a linear stability analysis. The main components of the solver structure are shown in the overview in figure 3.1.

The assumptions on which the model is based are explained in this chapter, followed by a short breakdown of each of the building blocks.

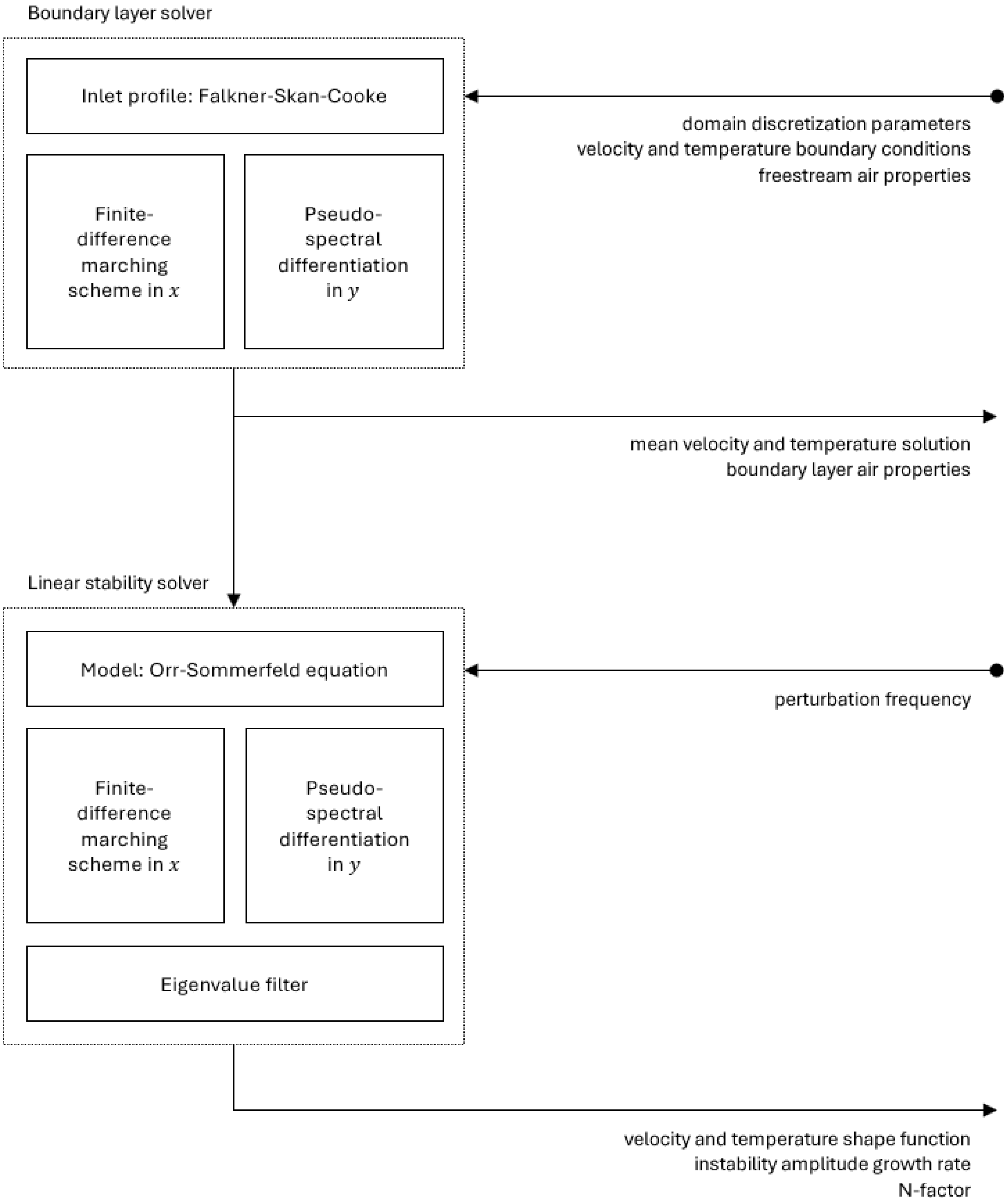

Figure 3.1: Schematic of the computational code

3.1 Flow assumptions

In order to mathematically model the boundary layer flow, several assumptions were made, some of which conveniently simplify the flowfield. These assumptions are expected to hold in the experiment as well.

3.1.1 Fluid properties

The solvers are based on the flow of a calorically perfect gas, i.e. its specific heat capacities c_V and c_P are assumed constant. The ideal-gas law inherently applies. The gas is further assumed to obey Sutherland's law for the viscosity as a function of temperature. The compressible solver take the temperature-dependence of the fluid's properties into account, whereas the incompressible solvers assume constant properties throughout the domain.

3.1.2 Freestream parameters

The base flow outside the plate's boundary layer in assumed to be steady, i.e. independent of time. Moreover, it is uniform in all directions, with the base flow velocity components known to be

$$U(x,y,z) = U_0, \qquad V(x,y,z) = 0, \qquad W(x,y,z) = 0 \tag{22}$$

The freestream can thus be considered one-dimensional, with streamwise coordinate x. The parallel-flow assumption holds in the freestream.

Since all its velocity derivatives are zero, the base flow is irrotational by definition and does not allow for linear wave formation either. Without any form of artificial flow perturbation, the freestream's turbulence intensity would therefore be zero and no transition would set on in the modeled boundary layer. To induce transition, a "clean" acoustic wave is superimposed on the freestream velocity: a sinusoidal perturbation of constant angular frequency that propagates with the speed of sound. The total components of the freestream velocity now become:

$$U(x,y,z,t) = U_0 + U'(x,y,z,t), \qquad V(x,y,z,t) = V'(x,y,z,t), \qquad W(x,y,z,t) = W'(x,y,z,t) \tag{23}$$

Although the perturbation component U' depends on both space and time, its characteristic time scale is much smaller than that of the base flow—which, in this model, is infinitely large. Due to its sinusoidal character, the superimposed acoustic wave is therefore steady when time-averaged, so that the freestream can be qualified as time-averaged steady as well. Since perturbations are damped out in the laminar part of the boundary layer, the acoustic wave is assumed not to influence the solution to the laminar boundary layer equations. The frequency of the acoustic wave comes into play in the stability analysis.

3.1.3 Compressibility

The compressibility assumption is what distinguishes the two types of numerical models that are assessed, see also section 3.2. Compressibility effects are assumed to be negligible under the circumstances of the experiment. Whether this assumption is valid, is studied in the current work, by comparing the two different models: one that is based on the incompressible Navier–Stokes equations and one based on the compressible ones. This results in different boundary layer equations as well as different stability equations. In the compressible case, the density and viscosity of the fluid —which, in this model, is always air —are not constants, but depend on the local static pressure.

Whether or not the flow is assumed to be compressible thus influences the assumptions made regarding equations behind the code, and the role of the viscosity. Both topics are further discussed in the following subsections.

3.1.4 Viscosity

Near the wall, the viscosity of the air is considered not to be negligible compared to the streamwise velocity, so that the Reynolds number is always finite. As discussed in chapter 2, taking the fluid's viscosity into account is necessary for the analysis of flow transition, since many of the occurring phenomena are viscous effects. The variability of the viscosity depends on whether the flow is assumed to be compressible.

Further away from the wall, the airflow can be considered inviscid. This is the same distinction that Prandtl made when deriving his boundary layer equations, on which the current boundary layer solver is based. For the full equations, see section 3.2.

3.1.5 Simplifications of the boundary layer flowfield

Like the freestream, the flow inside the boundary layer is steady when time-averaged. The parallel-flow assumption is also valid in the boundary layer, so that the solver is not suited for modelling large streamwise gradients due to non-streamlined geometries such as steps and humps. It was stated in the previous paragraph, that the freestream has only one spatial dimension. In the boundary layer, however, gradients exist in the wall-normal direction, since the streamwise velocity increases with distance from the wall. Velocity perturbations may exist in all directions, although only those in the x- and y-direction are considered, since the cross section of the boundary layer is assumed to be infinitely constant in the z-direction. In conclusion, the velocity components in the boundary layer are given by:

$$u(x, y, z, t) = u_0(x, y) + u'(x, y), \qquad v(x, y, z, t) = v'(x, y) \tag{24}$$

Furthermore, inside the boundary layer the following holds:

$$u \gg v, \qquad \frac{\partial u^2}{\partial^2 y} \gg \frac{\partial u^2}{\partial^2 x} \tag{25}$$

This leads to the form of the boundary layer equations presented in subsection 3.2.1.

The boundary layer is modeled as a Falkner-Skan flow over an almost-flat plate, i.e. for a very small wedge angle β, so that its solution slightly deviates from the Blasius solution. This is to account for the (small) favourable pressure gradient that establishes in a wind tunnel—or any other flow volume of finite cross section—due to the formation of a boundary layer. This approach allows for an inflow condition to be drawn up from the known boundary conditions. Similarity solutions are assumed for the remainder of the laminar part of the boundary layer.

3.2 Mathematical model behind the solvers

Two distinct numerical models are available to solve for the boundary layer: one assuming an incompressible flow, and one accounting for compressibility effects. Because the experiment will be carried out at a very low Mach number (approximately 0.05), it is expected that compressibility effects can be neglected. This is verified by running both the compressible (CBL) and incompressible (IBL) solver with boundary conditions corresponding to the experimental cases and comparing the solutions. It should be noted, however, that the velocity output of the CBL is not only linked to the temperature field through the compressibility assumption, but also via the temperature dependence of certain fluid properties, regardless of compressibility effects. This dependence may also be true for an incompressible boundary layer flow, but will not resonate in the IBL's output. Therefore, it is decided to use only the CBL solutions for the comparison of the two linear stability solvers as described in the next subsection. To illustrate the differences between the two approaches, both boundary layer solvers are explained and compared first.

3.2.1 Governing equations for the time-averaged boundary layer

The two-dimensional flowfield consists of a freestream of uniform velocity U, and a boundary layer with edge velocity $u_e = U$. The viscous portion of the boundary layer is described by the Navier–Stokes equations, which can be somewhat simplified depending on the applied compressibility assumption. This yields Prandtl's boundary layer equations for incompressible flow, which read as follows:

$$\text{mass continuity:} \qquad \frac{\partial u}{\partial x} + \frac{\partial v}{\partial y} = 0 \tag{26a}$$

$$x\text{-momentum:} \qquad \rho \left(u\frac{\partial u}{\partial x} + v\frac{\partial u}{\partial y} \right) = -\frac{\partial p}{\partial x} + \mu\frac{\partial u^2}{\partial y^2} \tag{26b}$$

$$y\text{-momentum:} \qquad -\frac{\partial p}{\partial y} = 0 \tag{26c}$$

For compressible flow, equations (26a)–(26b) are replaced by (4a)–(4b), and the system is supplemented with the energy equation (18).

The compressible boundary layer solver accounts for compressiblity effects by deriving the values of density and viscosity from the known freestream temperature and Mach number and the prescribed wall temperature.

3.2.2 Governing equations for the boundary layer stability

The velocity, temperature and fluid property solutions of the boundary layer solver serve as inputs for the linear stability solvers. As well as for the boundary layer solution, the incompressible and compressible stability solution are compared. In the incompressible case, the Orr–Sommerfeld equation (16) is to be solver. For the compressible approach, the single equation is replaced by the system (39–43).

Both the ILST and CLST models require an input that alters the velocity boundary condition, namely the initial perturbation frequency f. This corresponds to the acoustic forcing frequency applied in the wind tunnel experiment, see subsection 4.2.

The stability solution includes the growth rate $-\alpha_i$ of the perturbations at each streamwise station for a given perturbation frequency. From these growth rates, an N-factor is derived as follows:

$$N = -\int_{x_{\text{ds}}}^{x} \alpha_i dx \tag{27}$$

3.2.3 The non-adiabatic wall condition

The model enables two different thermal boundary conditions prescribed at the solid wall: the heat transfer normal to the wall, or the isothermal wall temperature distribution. Both boundary condition types are steady and therefore depend on x alone. Because the current research is aimed at establishing a correlation between wall temperature are transition behaviour, the isothermal boundary condition is employed.

The temperature distribution at the wall is obtained from infrared measurements of a cooled flat plate in a flow. Since the temperature input is set to depend on the streamwise coordinate alone, the spanwise mean of the measured temperature is used.

It is seen from the governing equations, that the (wall) temperature appears exclusively in the energy equation. Solving for the complete temperature distribution therefore requires the other two variables in this equation, namely u and v to be determined first. The solution to u is obtained from the x-momentum equation, where the pressure x-derivative is computed with the known edge velocity. The Falkner–Skan–Cooke method produces a v-profile which is assumed to be constant at every streamwise station for now. The true v-distribution is later computed through the continuity equation.

The wall cooling condition affects the flow's temperature profile in the sense that it will show an inflection point (or even two), as opposed to the profile that forms in an adiabatic-wall boundary layer due to frictional heating alone.

3.2.4 The Falkner-Skan inflow condition

The inflow conditions, i.e. the velocity and temperature profiles at the upstream domain boundary, are obtained from a Falkner–Skan–Cooke (FSC) model. It is important to bear in mind that this inflow condition is only valid for very low Mach numbers. Following the FSC model, the external velocity u_e is given by:

$$x_e = U_0 \left(\frac{x}{L} \right)^m , \tag{28}$$

where L is the length of the surface in streamwise direction. For a flat plate, the similarity parameter m is approximately constant. It is obtained from the Hartree parameter β_H:

$$m = \frac{\beta_H}{2 - \beta_H} \tag{29}$$

The Hartree parameter is computed from the pressure coefficient C_p on the flat plate [66]:

$$\beta_H = \left(\frac{1}{2} - \frac{1 - C_p}{x \frac{dC_p}{dx}} \right)^{-1} \tag{30}$$

The pressure distribution over the flat plate used in the wind tunnel experiment is presented in section 4.2. Integration of experimentally determined pressure data and the pressure coefficients found using a Navier–Stokes solver, both result in a chordwise-averaged Hartree parameter of approximately 0.01, so that $m \approx 0.005$.

Note that even though the Falkner–Skan–Cooke theory is often used to compute similarity solutions, this cannot be done for the current boundary layer. Similarity solutions are only verified under the assumptions of unity Prandtl number and ratio of specific heat capacities [67]–[69], which do not hold for the airflow modeled here.

3.2.5 Non-dimensionalization of parameters

If the flow is assumed to be compressible, a non-dimensionalization of the flow variables is required to enable a solution to the boundary layer equations. Scaling parameters originate from either the boundary layer edge or the freestream. The following non-dimensionalizations are evaluated:

$$\begin{gathered} \bar{x} = \frac{x}{\delta_0} \qquad \bar{y} = \frac{y}{\delta_0} \qquad \bar{u} = \frac{u}{U_0} \qquad \bar{v} = \frac{v}{U_0} \\ \bar{T} = \frac{T}{T_\infty} \qquad \bar{p} = \frac{p}{p_a} \qquad \bar{\mu} = \frac{\mu}{\mu_\infty} \qquad \bar{k} = \frac{k}{k_\infty} \qquad \bar{\lambda} = \frac{-\frac{2}{3}\mu}{\lambda_\infty} \end{gathered} \tag{31}$$

The scaling parameter δ_0 represents the Blasius length scale:

$$\delta_0 = \sqrt{\frac{\nu x_{\text{ref}}}{U_0}}, \tag{32}$$

with x_{ref} set to the starting point of the domain. All input variables to the boundary layer solver are initially scaled, and transformed back to physical quantities after the marching procedure is completed. The resulting quantities are non-dimensionalized again before they are fed into the stability solver.

3.2.6 Domain discretization and finite-difference scheme

In order to solve any of the two sets numerically, a discretization of the flowfield is required in both x and y.

The coordinate spacing is linear in the x-direction and therefore simply depends on the number of discretization points for a given domain length L. To avoid a singularity at the leading edge, the computational domain starts at some (small) $x_{\mathrm{ds}} > 0$. The solution to the boundary layer equations is found by iteration, using a forward-marching finite-difference scheme in which all previous streamwise stations are taken into account.

At each streamwise location, the spacing in y is set up by means of the Chebyshev collocation method, and the derivatives in the y-direction are prepared in the associated pseudo-spectral differentiation matrices as proposed by Weideman and Reddy [45], see paragraph 2.3.2.

The employed marching method involves the solution at a number of upstream stations, depending on the chosen order of the finite-difference scheme. A scheme of order 2 was found to be sufficient for the modelling of the considered flowfields, so that the initial guess at a certain streamwise station is simply equal to that at the previous station. An iterative computation is subsequently carried out, solving for the temperature, viscosity and velocity components up to the following convergence errors:

$$\varepsilon_T = \frac{T_i - T_{i+1}}{T_e}, \qquad \varepsilon_u = \frac{u_i - u_{i+1}}{u_e}, \qquad \varepsilon_v = \frac{v_i - v_{i+1}}{v_{i+1}}, \qquad \varepsilon_\mu = \frac{\mu_i - \mu_{i+1}}{\mu_{i+1}} \tag{33}$$

3.2.7 Eigenvalue filtering

The linear stability solver delivers the eigenvalues and eigenvectors that form the solution to the (non-dimensional) stability problem. A filter is applied to identify incorrect eigenvalues by comparing the eigenfunctions with an exponential fit:

$$\phi(y) = e^{-i\alpha_r y} \tag{34}$$

The real part of the wavenumber, α_r, thus represents the eigenvalue in this problem. The convergence threshold is adapted to the number of sign switches in the slope of the eigenfunction. All eigenvalues within the set threshold are maintained in the filter output.

3.3 Validation of the computational model

To the author's knowledge, no experimental or DNS (direct numerical simulation) data have been published on the effects of surface-cooling on a flow's transition behaviour in the subsonic regime. However, a numerical model was previously made by Ren and Kloker [70] to capture the influence of the wall-to-freestream temperature ratio for three-dimensional boundary layers in non-ideal fluids. The researchers simulated the boundary layer flow by means of a parabolic Navier–Stokes (PNS) model. The solution was fed to a compressible linear stability (CLST) solver, based on the same set of equations as the solver used in the current research. Both the compressible boundary layer solver (CBL) and CLST used in the current research, were compared to the results of Ren and Kloker by Barahona [71]. The comparison was carried out for a wall-cooling as well as a wall-heating case.

The boundary layer integral quantities as computed with the PNS model and the CBL, respectively, are plotted in figure 3.2. The figure shows that all profiles are nearly identical for both models. The results obtained with the two different CLSTs are plotted in the form of the instability amplitude growth rate (figure 3.3) and the N-factor (figure 3.4). The agreement between these stability characteristics is again very accurate.

It is concluded that both the CBL and CLST models used in the current research comply with the models by Ren and Kloker. This provides, however, no direct information on their compliance with experimental or direct numerical results.

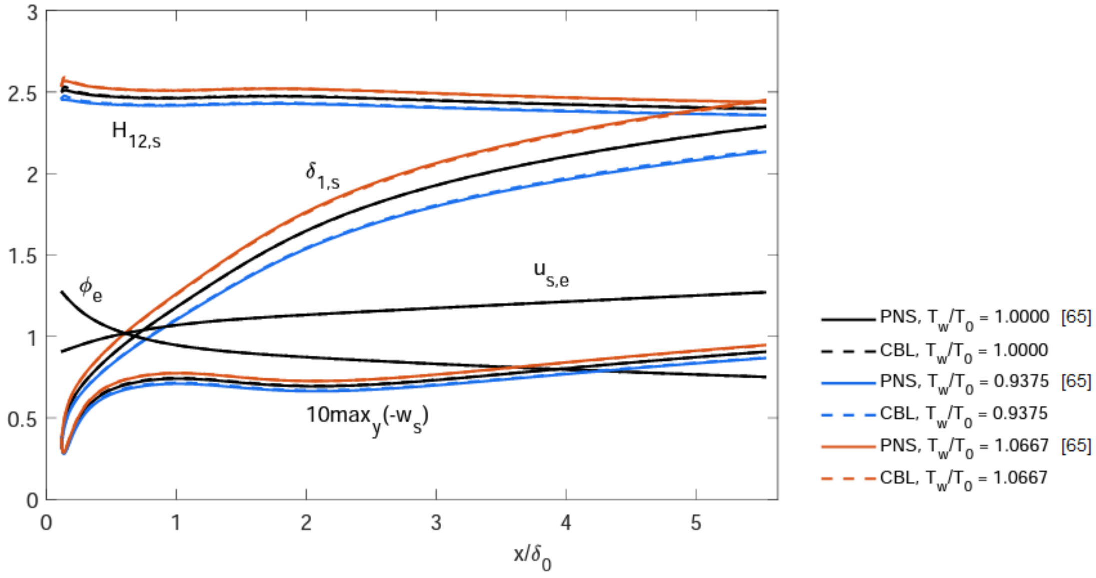

Figure 3.2: Boundary layer integral quantities, compared for the CBL solver used in this research and the PNS solver by Ren and Kloker [70], adapted from [71]

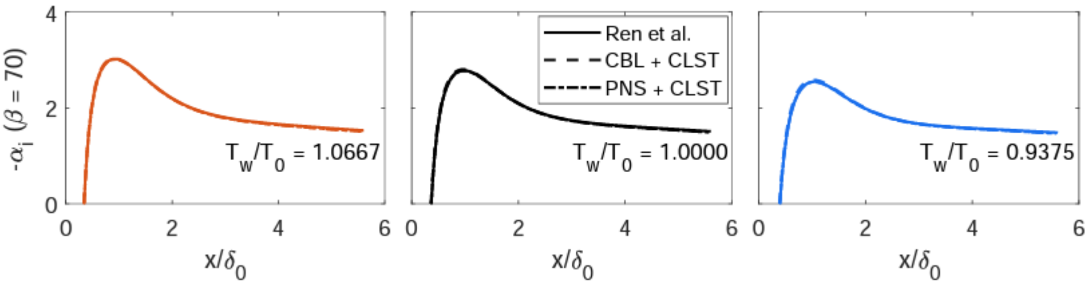

Figure 3.3: Instability amplitude growth rates, compared for the CLST solver used in this research and the CLST solver by Ren and Kloker [70], adapted from [71]

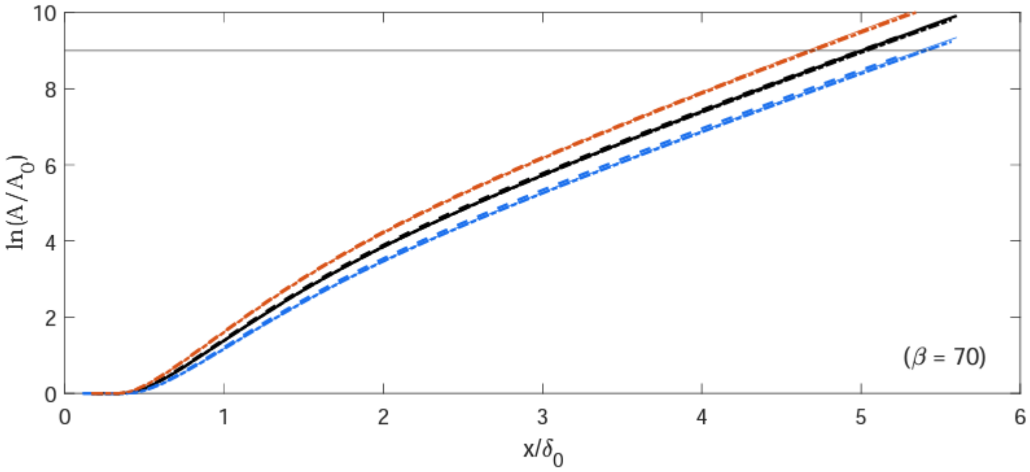

Figure 3.4: N-factors for β = 70, compared for the CLST solver used in this research and the CLST solver by Ren and Kloker [70], adapted from [71]. Legend corresponds to figure 3.2

4 Experimental approach

The experiment was designed to comply with the assumptions described in section 3.1. In line with this, the measurement methods were chosen such that they affect the flow in the least possible way. A detailed description of the experimental setup conducted to achieve this, is provided in this chapter.

4.1 Wind tunnel facililty

Measurements were performed in the anechoic tunnel (A-tunnel) at the Low Speed Laboratory of Delft University of Technology. The A-tunnel is a vertical, open-jet, closed-loop facility that was designed for aeroacoustic research and flow transition and control purposes. A schematic is shown in figure 4.1.

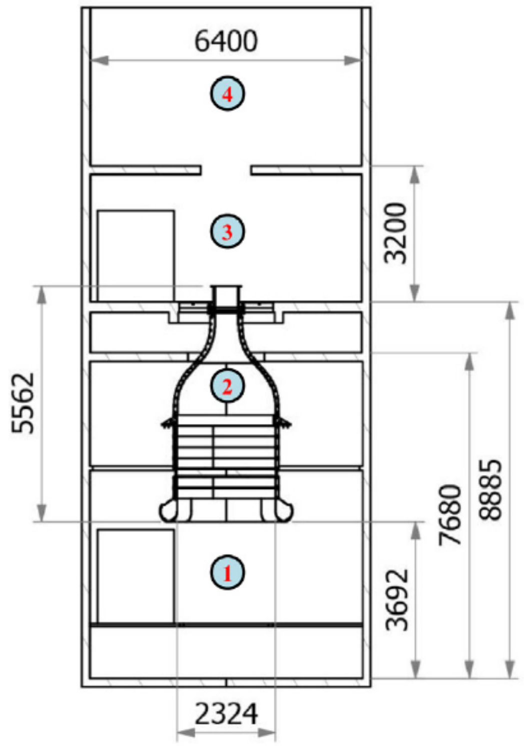

Figure 4.1: Nozzle extension "Delft 50×50" [72]

Figure 4.2: ◂ Schematic side view of the A-tunnel facility [72], with: 1) settling chamber; 2) contraction shape featuring the rounded inlet lip, flow straightener, anti-turbulence screens and converging outlet nozzle; 3) open-jet test section inside an anechoic plenum; 4) fans and collector room (dimensions in mm)

The test section is located at the number 3 in figure 4.1. An extension is placed on the nozzle outlet (see figure figure 4.1) which serves to adapt the test section's cross section. The outlet of the nozzle extension has a square 50cm × 50cm cross section. On the top edges, a transparent enclosure is set up in which the test model is placed. Overview images of the test section in shown in Appendix B.

Several flow characteristics were determined to asses the aerodynamic performance of the tunnel (see [72]). The mean flow was found to be uniform up to a maximum velocity deficit of $(U - U_\infty)/U_\infty = -0.8\%$ in the most near-wall part of the recommended measurement area at $U_\infty = 34$ m/s. At lower freestream velocities, the relative deficit was smaller. Since the tunnel is operated at 16.7 m/s in the current research, the expected mean flow uniformity is considered sufficient. The recorded turbulence intensity $\sqrt{u^2}/U$ remains below 0.1% for the operational freestream velocity. Lastly, peaks in the spectral density of the measured velocity fluctuations in the test section are observed at frequencies invariant to the freestream velocity. In fact, the peaks even occur at $U_\infty = 0$, indicating that they are due to noise in the data acquisition system. The insensitivity of the peaks to frequency points out that there is a standing wave

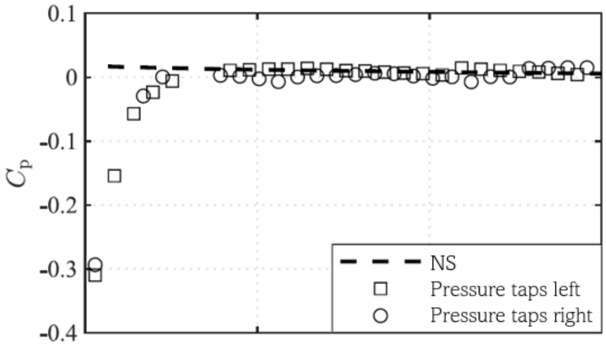

Figure 4.3: Modeled and measured pressure distribution over the flat plate, adapted from [73]

in the jet column. Measurement errors caused by these fluctuation peaks can be avoided by bypassing the corresponding frequencies during experiments. They can however not be predicted in advance, since the exact frequencies depend on the geometry of total of the nozzle, test model and measurement equipment in in place. Details regarding the anechoic design of the A-tunnel can be found in [72].

The temperature of the freestream is measured in the settling chamber. Since the temperature cannot be kept uniform throughout the facility and the measurement location is at approximately 6m from the test section, the recorded value may well differ from the real freestream temperature at the height of the flat plate. Moreover, the airflow is known to warm up as the tunnel is in use for several hours in a row. To diminish this uncertainty, the temperature is additionally measured in the test section by cold-wire anemometry, see also section 4.4. All measurements were conducted at freestream temperatures between 19.7^oC and 21.4^oC. The humidity of the air is not measured during the current experiment.

4.2 Flat plate model and cooling system

The flat-plate model consists of a 20 mm thick main body with a cutout for a separate cooled insert, shown in figure 4.5 and 4.6. The main body has a width of 495 mm and a length of 1000 mm including the elliptical leading edge and an adjustable trailing edge. The streamwise non-dimensional coordinate x/L therefore coincides with $\frac{x}{1000}$ and for convenience, it is decided to stick with the dimensional form to indicate streamwise locations throughout this work. The aluminium main body features a modified super-elliptical leading edge [74] and sharp, adjustable-angle trailing edge, all of which have a smooth, black, low-reflective surface. The flat plate is installed in the test section with the leading edge facing the freestream. Two streamwise arrays of pressure taps are present, that were used in previous research by

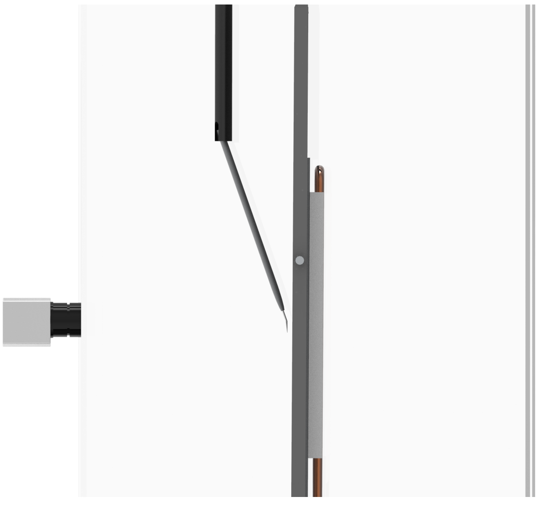

Figure 4.4: Side view of the test section with the flat plate, liquid cold plate (right), infrared camera (left) and hot wire probe (from top)

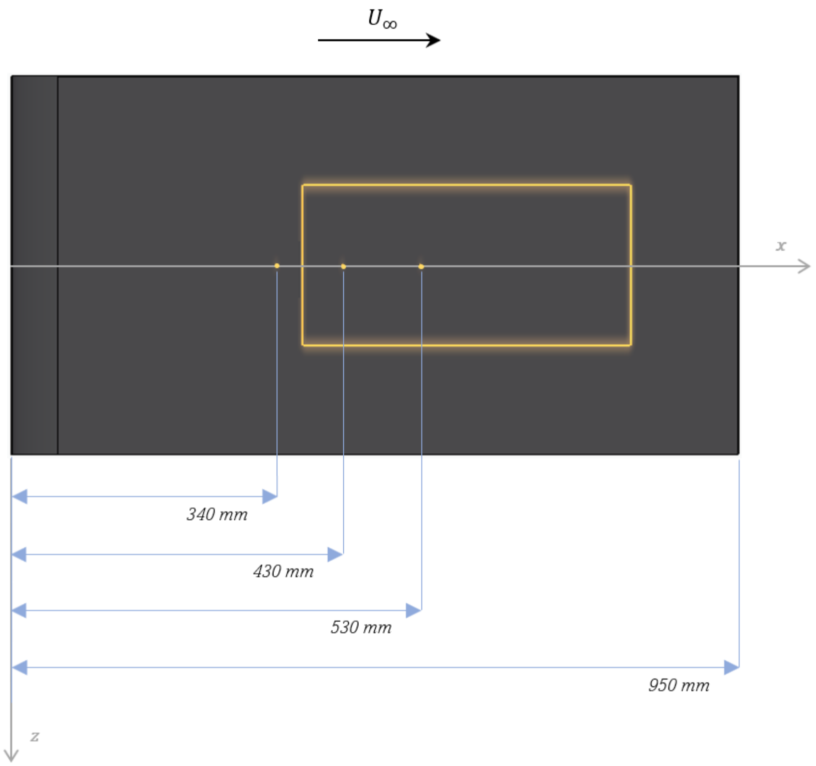

Figure 4.5: Measurement side of the flat plate, with the locations of the cooled insert and the measurement points in yellow

the plate's designers [73] to establish the pressure coefficient at a freestream velocity of 20.9 m/s, which is considered close enough to the 16.7 m/s in the current experiment. The result is depicted in figure 4.3. To avoid upstream effects of a thick boundary layer on the back surface, zigzag tape is placed near the leading edge on the rear side of the plate. Note that the tape is not depicted in figure 4.6.

The observed pressure gradient is slightly favorable due to the formation of boundary layers over the plate and wall in the constant-cross section test section. Its value serves as an input to the boundary layer solver as described in chapter 3.

The acrylic insert is laser-cut to fit the cutout in the main body, see figure 4.5. The insert is cooled by means of a so-called liquid cold plate: a thick aluminium plate housing a configuration of copper pipes that allow for a coolant to flow through. A 6 mm stainless steel layer with the dimensions of the insert is mounted to the flat side of the liquid cold plate, serving to maintain a uniform distribution of the

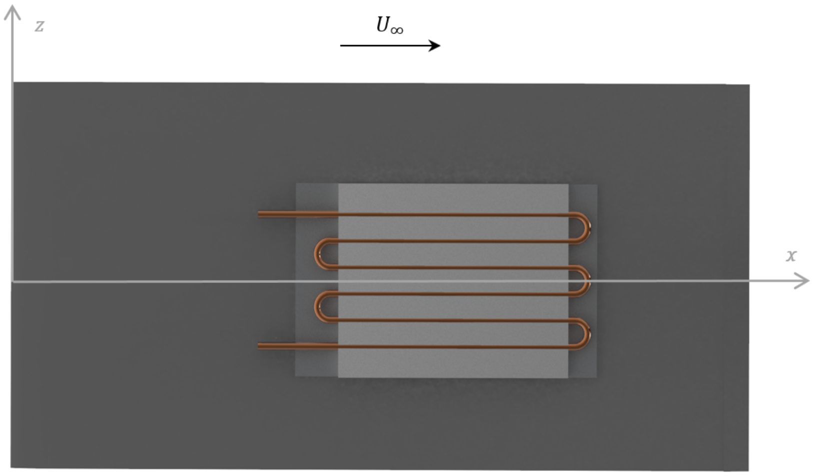

Figure 4.6: Rear side of the flat plate, showing the (disconnected) cooling system

temperature throughout the surface. Steel was selected for its low heat capacity and thermal conductivity compared to aluminium, so that it enables faster temperature switches during the experiment. The steel sheet is glued to the 3 mm acrylic insert. High-conductivity glue is applied to again secure fast and uniform response to the temperature settings and to avoid hot or cold spots on the surface that bolts may cause. The choice for acrylic is based on both its suitability for laser-cutting and its insulating quality, which is convenient in this non-adiabatic wall model. Rubber rings around the bolts that keep the steel and acrylic layer in place, allow for careful flush-mounting of the insert's surface with the main body. The acrylic surface is spray-painted in matt black, to reach an emissivity coefficient as close to 1 as possible. During the experiment, the liquid cold plate is covered with reflective tape in order to diminish heat losses though the back side. Drawings of the layered model are given in figure 4.7 (the rubber rings are not shown here). The total back view of the flat plate with the cooling system can be found in figure 4.6. For more details of the test model, see Appendix B.

The two copper pipe ends are connected to the inlet and outlet of a circulation cooler. The coolant hoses exit the test section through the back wall. To minimize the influence of noise on the acoustic signal, the cooler is placed outside the plenum. The air-cooled circulation machine is based on a thermostat system for refrigerant R449A. The coolant temperature can be selected on a user panel with an accuracy of 0.1 ^{o}C. Furthermore, the flow rate can be adapted to match the heat transfer demands of the experiment. Since both the freestream velocity and the wall-to-freestream temperature difference are small in the current experiment, the flow rate is fixed at the lowest value of 6 l/min. Six different wall-to-freestream temperature ratios are examined, ranging from 0.9576 to 1.0.

Figure 4.4 shows the test section configuration of the flat-plate model and the required measurement equipment for the experiment. The equipment is further treated in the following sections.

Transition is triggered by an acoustic signal of known frequency that is emitted by a speakerbox placed in the collector room. The experiment is conducted in a range of sound frequencies for which the formation of T–S waves is most clearly captured in the infrared camera's field of view. A test sweep has yielded 290, 295 and 300 Hz as the most suitable experiment frequencies. Figure 4.8 shows the combinations of temperature ratio and acoustic frequency included in the experiment.

Measurements are performed at three streamwise locations (see figure 4.5) and a total of 42 to 45 wall-normal coordinates, depending on the x-location. Each data point is measured for a duration of 2 seconds with a recording frequency of 51.2 kHz. The freestream velocity of 16.7 m/s is unvaried during the campaign, with the exception of quiescent-air measurements for each wall temperature setting, required for a wall heat conduction correction. More on this procedure follows in subsection 4.4.2.

(a) Cross-sectional view in the x, y-plane with the different layers for the heat transfer design indicated

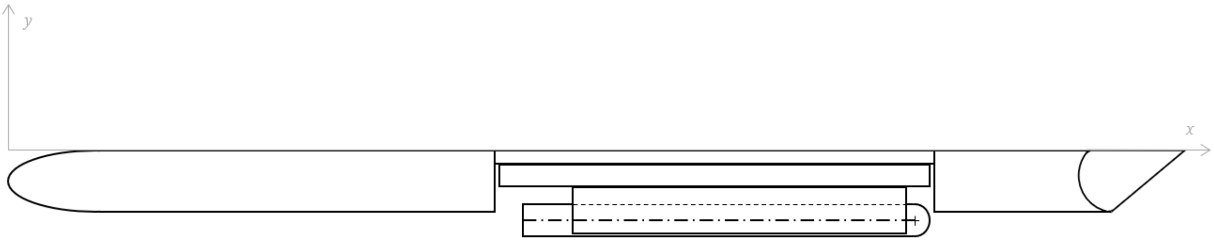

(b) Schematic cross-sectional view in the x, y-plane with the relevant dimensions indicated

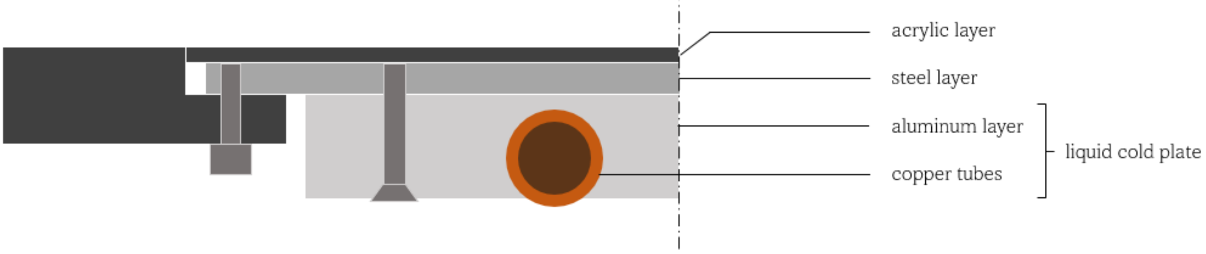

(c) Cross-sectional view in the y, z-plane with the different layers for the heat transfer design indicated

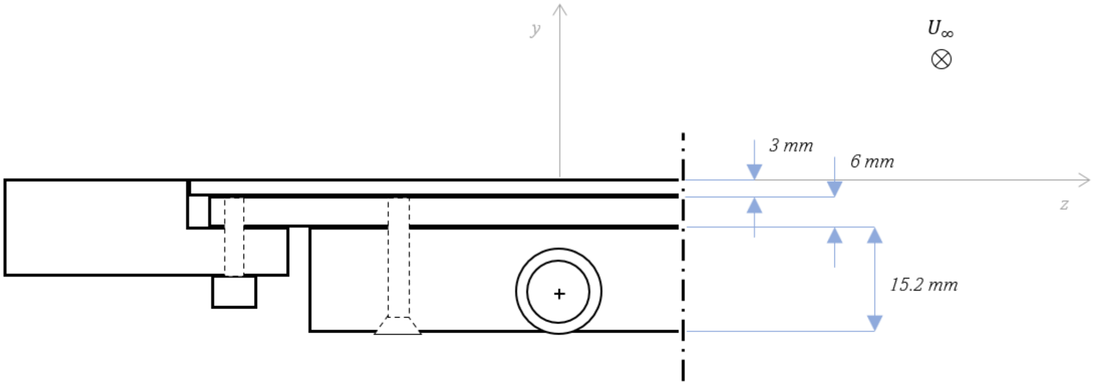

(d) Cross-sectional view in the y, z-plane, schematic

Figure 4.7: Details of the layered structure of the experimental flat plate

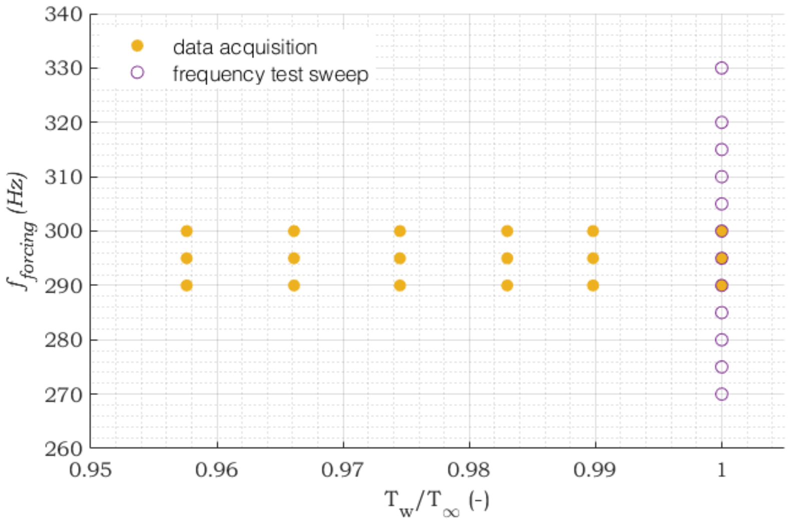

Figure 4.8: Combinations of wall-to-freestream temperature ratio and forcing frequency, pre-examined and included in the experiment

4.3 Quantitative infrared thermography

The purpose of surface temperature measurement in the experiment is twofold: to visualize the front of instability perpendicular to the freestream; and to identify the real-time temperature distribution of the surface on which the examined boundary layer exists. For the latter purpose, the thermography will be carried out simultaneously with the other measurement technique, i.e. wire anemometry. It is therefore important to use a non-intrusive technique for the temperature measurement. Infrared thermography satisfies this requirement.

4.3.1 Thermography equipment

An Optris PI 640i infrared camera [75] is used for the thermography. The camera has an optical resolution of 640 × 480 pixels and a thermal sensitivity of 40 mK. The manufacturer indicated accuracy is ± 2 ^{o}C or ± 2%, whichever is greater. In the low-temperature range of the current experiment, where the absolute temperature will not exceed 25 ^{o}C, nor will the wall-to-freestream temperature difference be larger than 12.5 ^{o}C, the expected accuracy is 2 ^{o}C. Although a possible error of 2 ^{o}C will not effect the behaviour of the boundary layer as predicted by the computational model much, it is a rather high number when it comes to the identification of the transition front. To adhere to the non-intrusive nature of the measurement method, the camera is placed just outside the test section, with the lens face flush with the test section wall. This positioning, in combination with the selected lens, fits the complete cooled insert in the camera's field of view. A circular cutout having the diameter of the lens is made in the wall, to avoid any reflection and refraction of the radiation to be measured.

The influence on the thermography of both the humidity in the tunnel and a wall emissivity coefficient that is presumably slightly lower than 1, cannot be directly accounted for. To best account for these uncertainties, the infrared camera is calibrated using a Pt100 temperature sensor, a device that is insensitive to both factors. The calibration procedure entails simultaneous temperature measurements by the infrared camera and the Pt100 mounted to the wall, in thermal equilibrium. In the applied temperature range, the Pt100 sensor has an accuracy of approximately 0.2 ^{o}C [76]. The setup for the thermal calibration is depicted in figure B.10 of Appendix B. A geometric calibration is carried out by placing a two-dimensional geometry of contrasting marks, i.e. points of very high or low emissivity, at known coordinates on the model surface. A white sheet with imprinted black dots is used for this.

4.3.2 Post-processing of the thermography data

The post-processing procedure for the infrared thermography measurements is presented in figure 4.9.

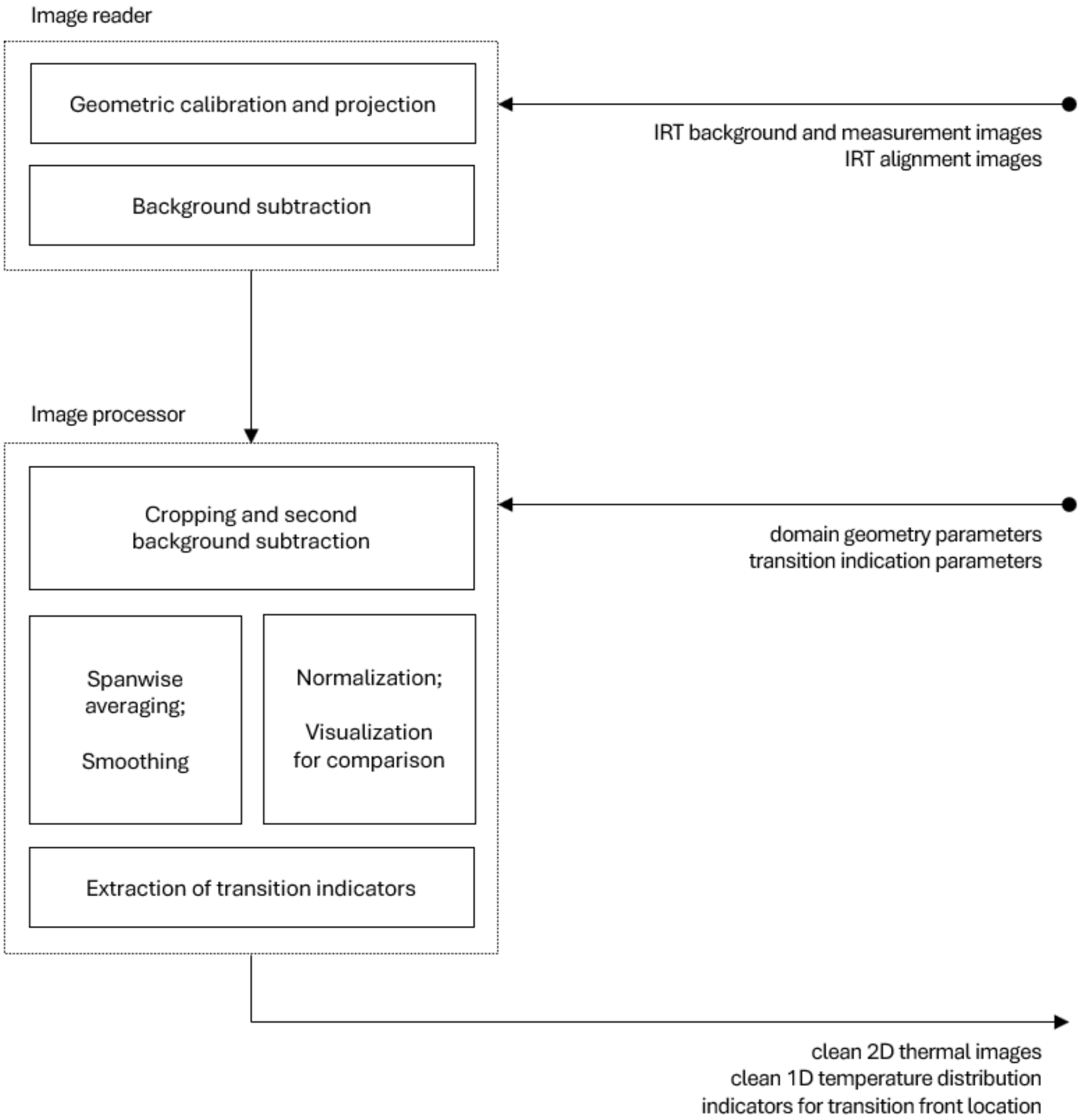

Figure 4.9: Schematic of the post-processing code for the infrared thermography measurements

As described in the previous paragraph, a simple geometric calibration procedure delivers the streamwise and spanwise coordinates for the recorded images. The measured temperatures are coupled to their corresponding coordinates, yielding two-dimensional thermal images. Boundaries for cropping a ”clean” image are set in both directions, ranging from the lowest measured temperature to the end of the cooled insert in the x-direction and enclosing a sufficiently spanwise-invariant region in the z-direction.

Two distinct ways to compare the flow transition fronts for different temperature setting are applied, roughly distinguished in a one-dimensional and a two-dimensional analysis. In the former, it is attempted to find the streamwise location where the spanwise mean temperature profile reaches its maximum. The second method entails a visual comparison of the thermal images. Both require some image processing in order to enable a valid comparison of the different cases. The difference between raw and processed

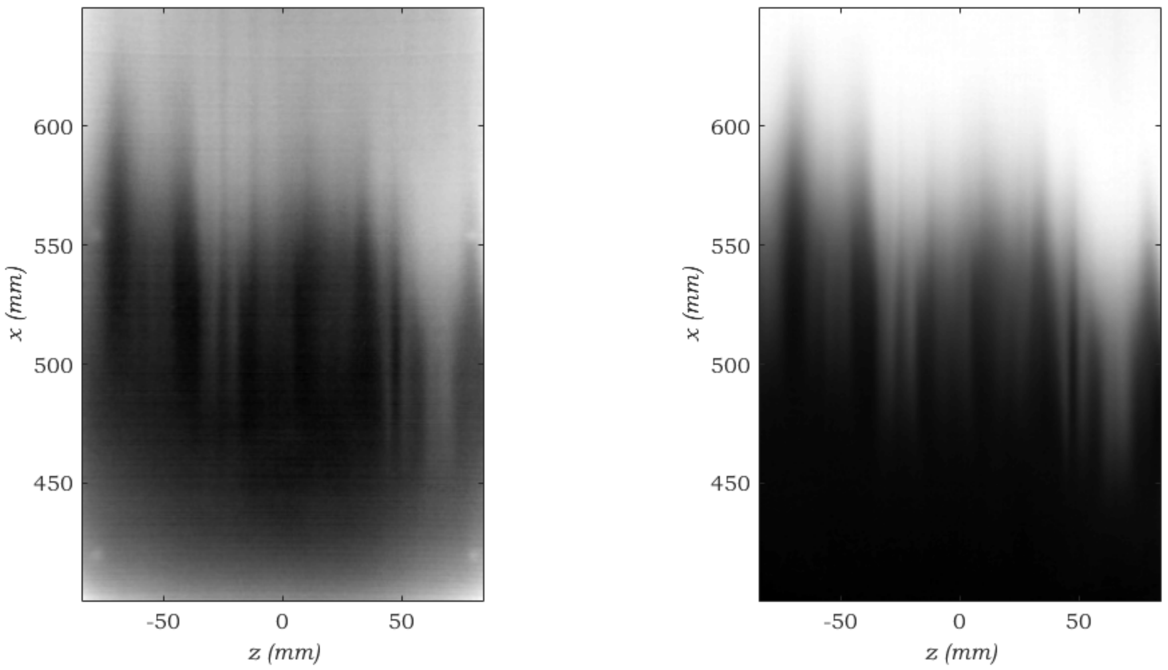

(a) Raw

(b) Processed

Figure 4.10: Example infrared thermography images, before and after the image processing routine

images is depicted in figure 4.10, pointing out the upgrade in workability with the data after processing. The processing routine in described in the following.

A typical method to identify the transition front by means of thermography, is to subtract a so-called background image, recorded at zero freestream velocity, from the images measured. The resulting images reveal the isolated effects of surface heating due to unstable flow structures. This allows for the transition front to be defined by a certain increase of the surface temperature, where the same threshold can be maintained for all cases. Since in the current experiment the surface is actively cooled down to varying absolute temperatures, the temperature increase at the transition front is different for each case, so that the aforementioned method does not suffice for comparing the different cases. To solve this issue, extra processing steps are introduced. Firstly, the difference between measurement and background temperature on the uncooled portion of the plate is subtracted from the image, to avoid discrepancies in the zero point between the wall temperature cases. Next, a one-dimensional and a two-dimensional visualization of the temperature distribution are made. The former is a spanwise average of the thermal image, aimed at highlighting the characteristics of the streamwise temperature rise that are expected to be indicators of flow transition. The spanwise mean distribution is smoothened by numerically computing its cumulative integral, and subsequently computing the numerical gradient of this integral. The characteristics of interest are the streamwise locations of the maximum gradient of the smoothened distribution and of the point where it reaches 99% of its maximum value. To rule out catching outliers, both locations are detected by means of a moving average on a sufficiently large streamwise range. Comparison of the two-dimensional thermal images with the blunt eye requires normalization of the data. Because the various wall temperature cases show very little differences, they are plotted in separate contour plots for clarity.

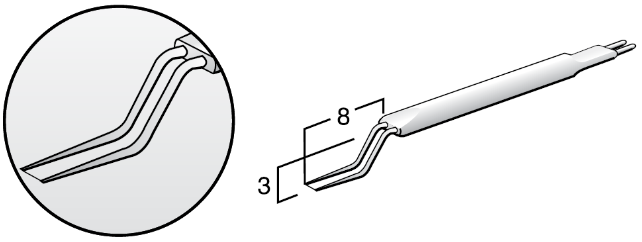

Figure 4.11: Single-wire boundary layer probe design (dimensions in mm)
© 2023 Dantec Dynamics A/S

4.4 Constant-current and constant-temperature anemometry

Anemometry is employed to record both the velocity and temperature profiles in the boundary layer. In order to maintain the best possible similarity of the flow during the two measurements, one is done as the wire probe moves toward the wall, and the other follows directly as the probe moves back out of the boundary layer. The targeted wall-normal coordinates at which the output voltages are recorded range from $y_{\min} = y(u = 0.1U_\infty)$ to $y_{\max} = 3\delta_{99}$. Their values are estimated using the computational model. The distribution of the coordinates in $[y_{\min}, \delta]$ is obtained by projecting a set of Chebyshev nodes on the interval, such that the density of coordinates increases with proximity to the wall. Five exponentially distributed coordinates are added to reach $y = 4\delta_{99}$, to ensure that the complete boundary layer is captured. The smallest y-coordinate is empirically determined with the wind tunnel running, at the point where $u = 0.1U_\infty$. This smallest distance to the wall is kept constant throughout the experiment (as well as the freestream velocity). A single-tungsten-wire boundary layer probe is used, that is designed to allow for very close approximation of the solid wall (see figure 4.11). The same probe is used for both the velocity and the temperature measurements. After each profile recording, the probe cable is switched between the sockets of the constant-temperature and constant-current machines.

4.4.1 Anemometry equipment

The constant-temperature anemometry (CTA) data is delivered by a TSI IFA-300 hot-wire anemometer connected to a Labview program. The latter converts the anemometer's output voltage to velocity through a procedure that is tailor-made for the A-tunnel facility and requires a single set of calibration data for the complete measurement campaign. This procedure uses the wind tunnel's overall temperature, measured in the settling chamber, to compute the air properties required for the calibration. Since the temperature differences in the examined boundary layers are quite large, the converted velocity values are only used to estimate the point where $u = 0.1U_\infty$. The non-converted output voltages are then fed to the post-processing routine, which is described in paragraph 4.4.2.

To extract the temperature data, a DISA 55M constant-current anemometer (CCA) is utilized. The probe resistance R_p is relates to the probe temperature T_p as follows:

$$R_p - R_{20} = \alpha_{20}(T_p - T_{\text{ref}}) \tag{35}$$

The reference values in this equation are further explained in Appendix C. The system's circuit current is constant, so that the output voltage is linearly related to the temperature of the flow—that is, within a certain temperature range for which the thermal coefficient for the wire's resistance is constant. Since no calibration data are available for the constant-current anemometer, a calibration procedure was designed: together with a Pt100 temperature sensor, the wire probe was placed in a closed volume of air of which the temperature can be varied. A pre-cooled mini fridge, slowly arriving back at room temperature, proved suitable. The acquired temperature-voltage relation is shown in figure B.11 of Appendix B. The observed relation is linear up to a 0.03 error, so that it can be concluded that the thermal coefficient is indeed constant in the measured regime. The temperature range of the calibration fully covered that of the experiment, making one-to-one conversion possible.

A short version of the operating manual for the DISA 55M was written for future users and is included in Appendix C.

4.4.2 Post-processing of the anemometry data

Figure 4.12 shows the order of post-processing operations for anemometry, yielding the corrected velocity and temperature data from the boundary layer.

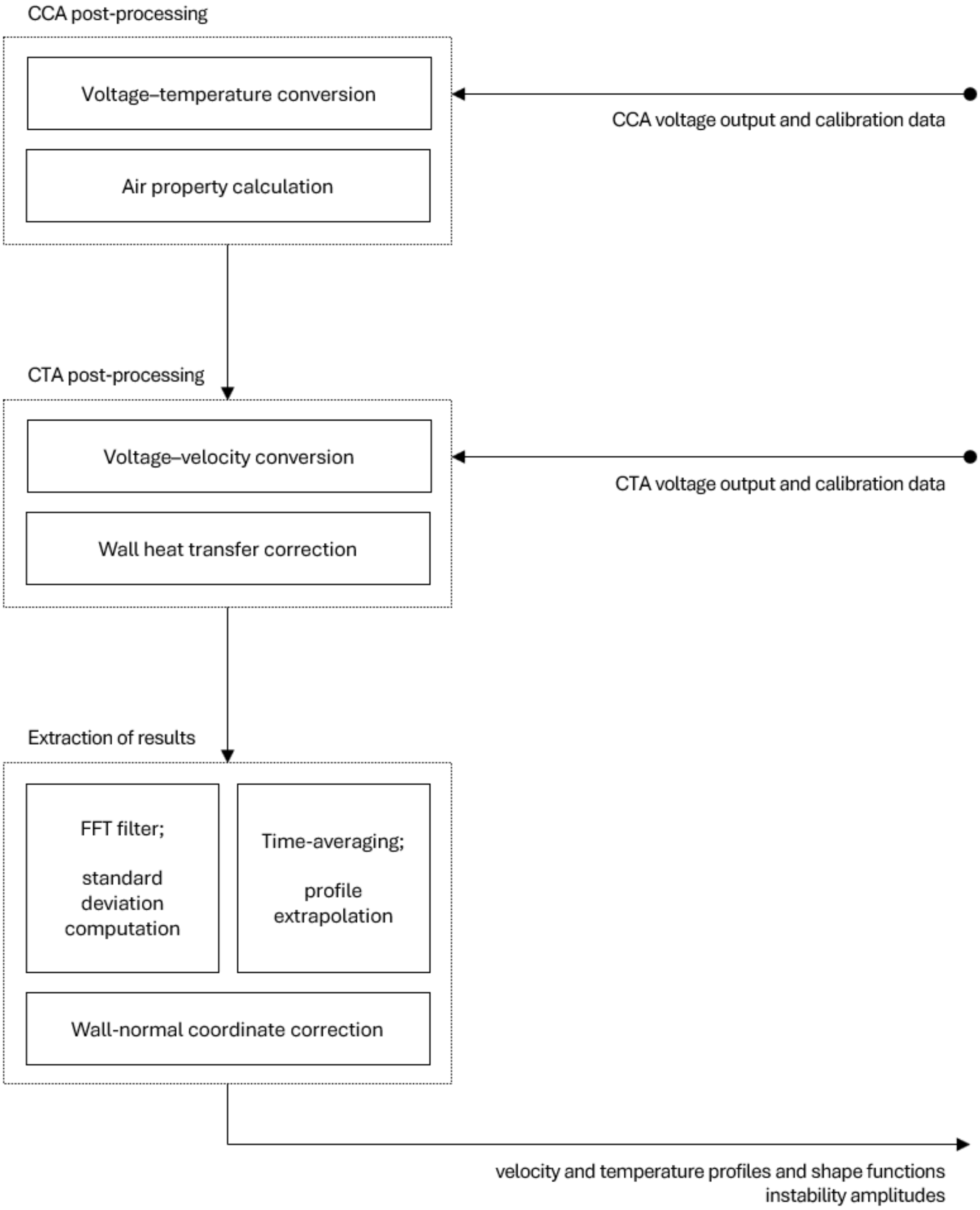

Figure 4.12: Schematic of the post-processing code for the hot and cold wire anemometry measurements.

Temperature profiles can be obtained directly from the CCA voltage output by linear interpolation. Under the assumption that the spatial coordinates of the data points for the CTA measurements correspond to those of the CCA measurements, the temperature data can be used to compute the local air properties required for the voltage-velocity conversion. The calculation method for the air properties was proposed by Smits and Zaragola [77] and is applicable to both incompressible and compressible flow.

The conversion from output voltage to temperature is based on a procedure designed for measuring flows with largely varying temperatures by Hultmark and Smits [78]. A polynomial relation is assumed between voltage V and velocity u:

$$\frac{u}{\nu} = f\left(\frac{V^2}{k\Delta T}\right), \tag{36}$$

where the fluid properties ν and k are evaluated at the film temperature $T_f = \frac{1}{2}(T_{\mathrm{wire}} + T_a)$ and T_{wire} is simply the temperature setting of the CTA. ΔT is defined as the difference between the wire temperature and the local air temperature. Hultmark and Smits propose a fourth-order polynomial fit for the function f, which was checked to be a good approximation for the relation in the current experimental temperature range as well: the error between the calibration values and the corresponding polynomial values does not exceed 0.027 in u/ν. The data fit is plotted in figure B.12b of Appendix B.

Temperature and velocity profiles are obtained by time-averaging the recorded data per data point. The resulting velocity profiles are yet to be corrected for possible conductive heat transfer from the hot wire to the solid wall. To this end, CTA measurements are done for each wall temperature setting in quiescent air. The recorded voltage is subtracted from the voltage measured with the tunnel running—a procedure suggested by Ikeya et al. [79]. It should be noted, that the share of natural convection in the total heat transfer amount is much larger for the quiescent air measurements, so that the conduction effect is not isolated here. The procedure has nevertheless proven to yield a valid approximation of the wall heat effects, in both laminar and turbulent boundary layers. The examination of the method entailed a comparison of corrected near-wall velocity measurements with the relation for wall coordinates $u^+ = y^+$, that is generally assumed valid in the viscous sublayer. The same comparison is carried out in the current post-processing routine. For details regarding the wall heat effect correction, see Ikeya et al. [79].

To transform the temperature and velocity data to shape functions, root-mean-square (RMS) values are determined at each wall-normal station. Prior to this, a Fourier transform is computed on each data point, and a band-pass filter is applied to remove the DC mean component and possible resonance peaks. The peak amplitude A of a resulting "clean" RMS profiles is divided by a reference peak amplitude A_0, measured in a fully laminar region. The logarithm of this ratio corresponds to the N-factor:

$$N = \ln\left(\frac{A}{A_0}\right) \tag{37}$$

The exact wall-normal coordinates at which the measurements are taken, however, remain unknown. An estimate for the wall-normal coordinates is made using the non-slip condition $u(y = 0) = 0$, and the assumption that the velocity profile is linear near the wall. A linear extrapolation is constructed based on the data points for which $u \leq 0.35U_\infty$. From the extrapolation's intersection with the y-axis, a vertical shift is found that is applied to both the velocity and temperature profiles, so that the non-slip condition is met. This process is visualized in figure 4.13. The shift is applied to the time-averaged velocity and temperature profiles as well as the shape functions.

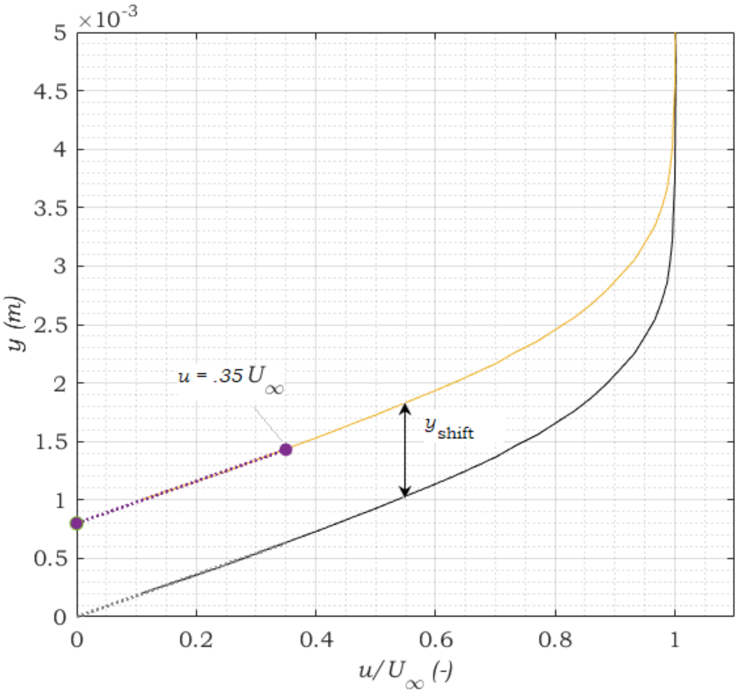

Figure 4.13: Correction procedure for the wall-normal coordinates of the anemometry measurements by linear extrapolation. The yellow line represents the unshifted profile; the purple dotted extension is used to find the location of the wall. The shifted profile is plotted in black

.

5 Discussion of the results

The outcomes of the incompressible and compressible computational models and the wind tunnel experiment are presented, compared and discussed in this chapter. First, the methods of modeling, measuring and post-processing, and their abilities to provide an answer to the research question, are evaluated in chapters 5.1 to 5.2.3.

The final results are discussed in chapter 5.4.

5.1 Note on the analysis of compressibility effects under the experimental conditions

All numerical results were obtained by adopting the temperature and velocity boundary conditions measured during the wind tunnel experiments as inputs to the numerical model. The influence of compressibility effects on the stability of non-adiabatic wall flows becomes apparent when comparing the experimental results to both the incompressible and compressible solver outcomes. Since not all the results of interest can be captured by all different solvers, this comparison is not applicable to certain topics. The incompressible boundary layer solver does not account for non-adiabatic wall conditions, so the outcome of the compressible boundary layer solver serves as the input to both linear stability solvers. The incompressible stability solver does not produce the velocity components required for shape functions, so that those can only be examined with a compressible approach.

A full comparison of the three methods in the form of the N-factor plotted against streamwise location is presented in subsection 5.4.3.

5.2 Evaluation of the experimental measurement methods

5.2.1 The wall heat transfer correction procedure

Upstream of the cooled insert, at $x = 340$ mm from the plate leading edge, the flow is assumed to be fully laminar. The correction for the effect of heat transfer from the hot wire to the wall on the measurements is evaluated by comparing the raw and corrected velocity profiles to the Blasius profile $y^+ = u^+$ for the laminar boundary layer. To that end, all three are plotted in one figure using logarithmic axes for clarity. See figure 5.1 for the comparison at $x = 340$ mm.

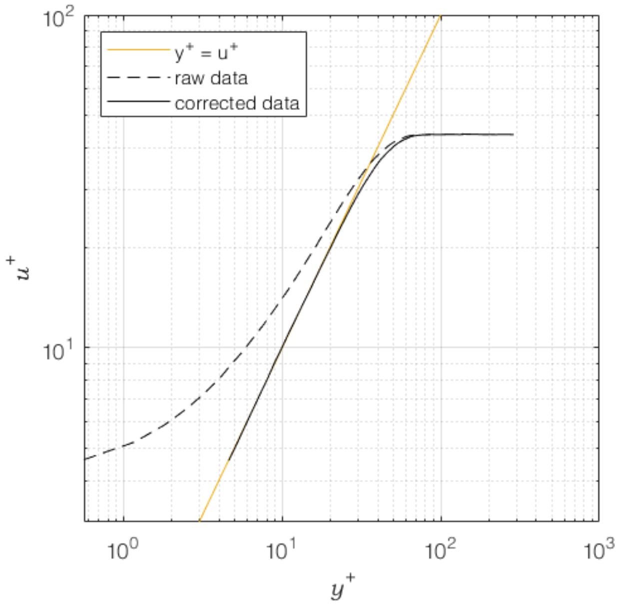

Figure 5.1: Comparison of the raw and corrected velocity profile at $x = 340$ mm, where the flow is expected to the fully laminar, including the Blasius solution for the laminar boundary layer

Up to $y^+ \approx 11$, the corrected data show excellent agreement with the Blasius profile at this station. Since the viscous sublayer of a turbulent boundary layer usually extends no further than $y^+ = 5$, it is assumed that the boundary layer on the plate is laminar at $x = 340$ mm. The corrected data should therefore follow the Blasius profile, and it is observed that the corrected procedure for wall heat transfer combined with the wall-normal shift of the profile yields accurate velocity magnitudes. Because of this, the same procedure is trusted in the post-processing of the velocity measurements at the downstream locations.

For the other measurement x-locations, the comparisons are depicted in figures 5.2 and 5.3. With the exception of the case $T_w/T_\infty = 0.9661$, the corrected profiles again correspond to the Blasius solution up to $y^+ \approx 11$ at $x = 430$ mm, which indicates that the boundary layer is still laminar here. The deviant character of the profile in figure 5.2e cannot be explained by anything other than an error in the quiescent air measurement, the velocity measurement itself or one of the experimental settings at the time of recording. At $x = 530$ mm, the corrected data do not obey as neatly to the $y^+ = u^+$ relation for the first wall coordinates. This can be another indication that the boundary layer flow is no longer linear at this station: the viscous sublayer of a turbulent boundary layer is significantly thinner than the linear part of a laminar boundary layer profile.

Note that differences in the wall shear stress cause the magnitudes of the first wall coordinates included in the plot to vary among the cases. The actual values of the wall-normal distance do not change here.

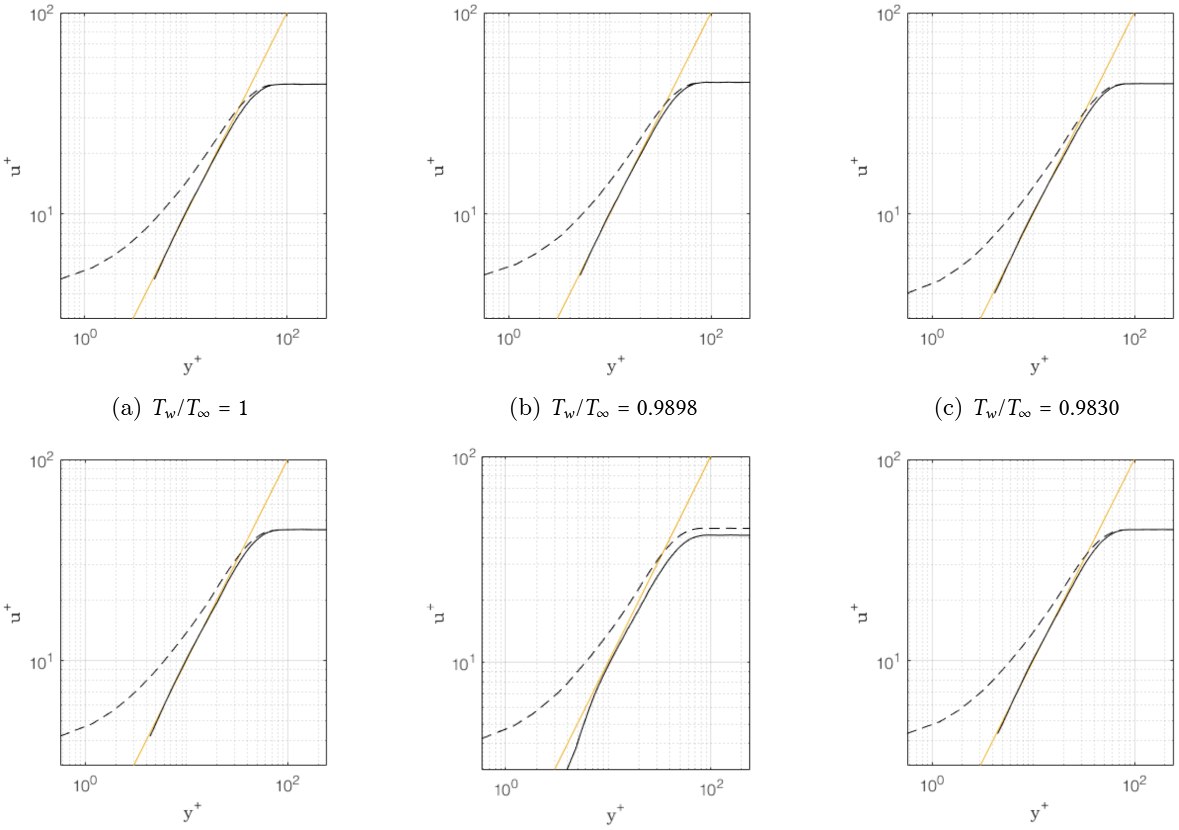

(a) $T_w/T_\infty = 1$

(b) $T_w/T_\infty = 0.9898$

(c) $T_w/T_\infty = 0.9830$

(d) $T_w/T_\infty = 0.9745$

(e) $T_w/T_\infty = 0.9661$

(f) $T_w/T_\infty = 0.9576$

Figure 5.2: Comparison of the corrected velocity profiles at $x = 430$ mm with the Blasius solution (legend corresponds to figure 5.1).

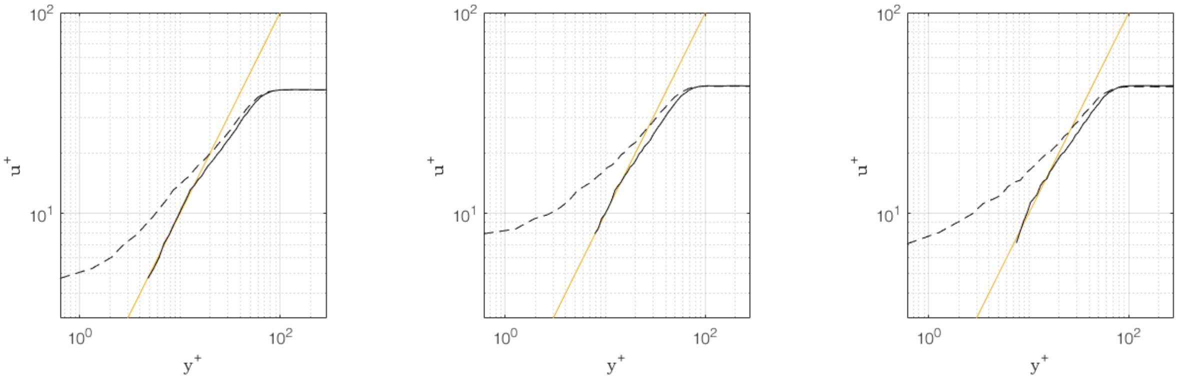

(a) $T_w/T_\infty = 1$ (b) $T_w/T_\infty = 0.9898$ (c) $T_w/T_\infty = 0.9830$

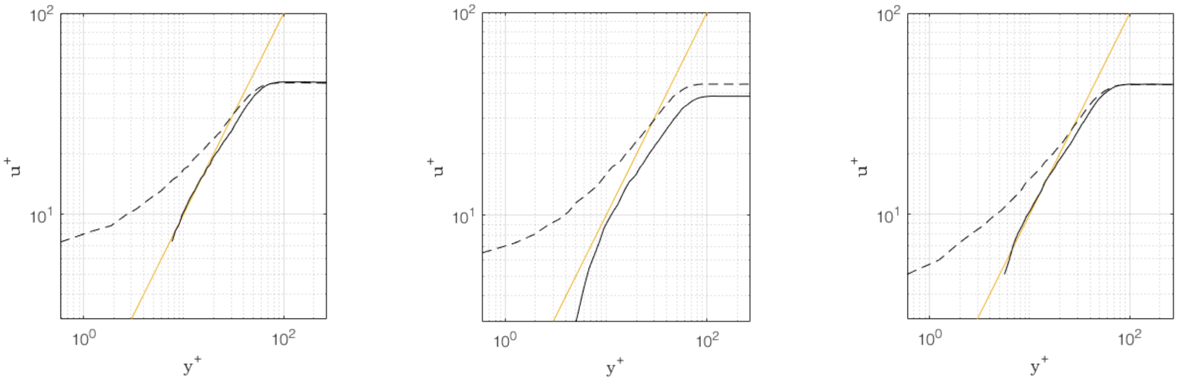

(d) $T_w/T_\infty = 0.9745$ (e) $T_w/T_\infty = 0.9661$ (f) $T_w/T_\infty = 0.9576$

Figure 5.3: Comparison of the corrected velocity profiles at $x = 530$ mm with the Blasius solution (legend corresponds to figure 5.1).

5.2.2 Acoustic forcing of the boundary layer transition

As described in chapter 4, a speaker is employed to force the laminar-turbulent transition of the boundary to take place on the cooled plate insert. The acoustic waves present in the test section as a result of this forcing method, are a type of Stokes wave of which the amplitude determines the receptivity of the boundary layer to anything that causes velocity perturbations, such as surface roughness and freestream turbulence. In the linear region of the boundary layer, all fluctuation amplitudes may be superimposed. Since the plate used in the experiment is very smooth and the turbulence level in the facility is very low, the amplitude of the Stokes wave is probably much larger than that of the velocity perturbations.

A spectral analysis of the measured velocity data confirms this assumption. Discrete Fourier transforms (DFTs) of the data acquired at the location of the T–S waves (see subsection 5.3 for how this location is established) are plotted in figures 5.4a and 5.4b for an example forcing frequency. At the two most upstream stations, the velocity fluctuations having a frequency of $f = 290$ Hz are far more amplified than the other frequencies in the spectrum. By evaluating DFTs at the location of the T–S waves for all forcing frequencies, it was confirmed that the frequency of the T–S waves is exactly that of the acoustic signal. For the most downstream station, the DFT at the wall-normal distance of the peak velocity fluctuation is given in figure 5.4c. At this station, fluctuations of other frequencies have an amplitude within the same order of magnitude as the fluctuation corresponding to the forcing frequency. However, this frequency remains the most amplified. This means that, even though a T–S wave is no longer detectable here (see again subsection 5.3 for an analysis), the fluctuations characterizing the boundary layer are still governed by the forcing frequency.

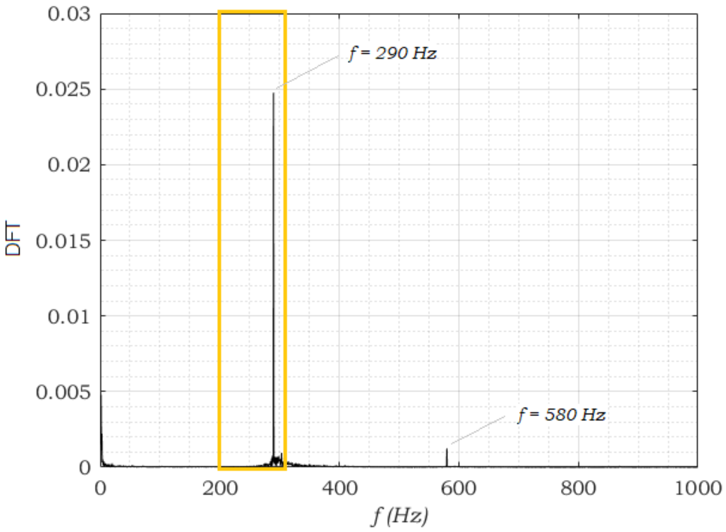

(a) x = 340 mm

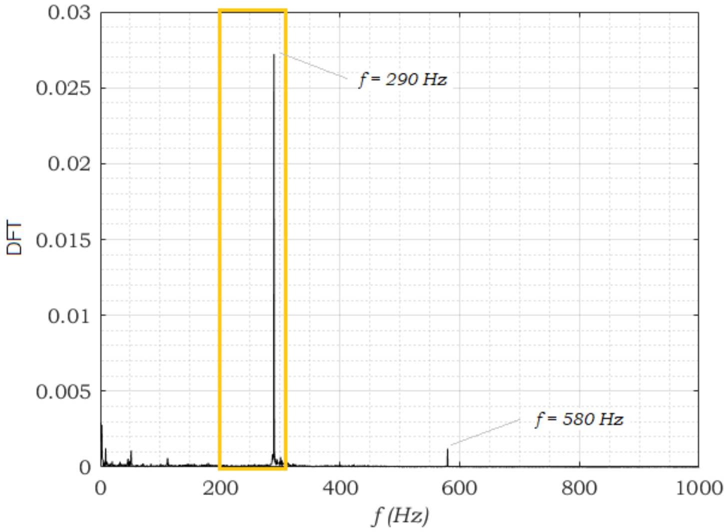

(b) x = 430 mm

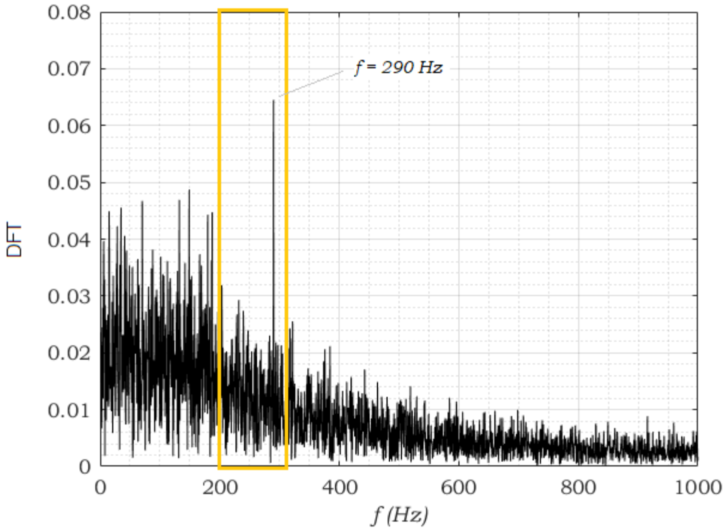

(c) x = 530 mm

Figure 5.5: Discrete Fourier transforms of the measured velocity data at the center of the T–S wave or at the wall-normal distance of the peak velocity fluctuation, at an acoustic forcing frequency of f = 290 Hz. Bounds of the applied band-pass filter are indicated in yellow

From linear stability analysis of the experimental data, the amplitude growth ratios α_i and wavenumbers α_r of the most unstable eigenmodes are obtained. These are compared to the solver predictions in figures D.1 and D.2 of Appendix D. Very little can be stated about the accuracy of these semi-experimental values. Could the wavenumbers be trusted, then they could be converted to wavelengths through the relation $\lambda = 2\pi/\alpha_r$. However, the phase velocity of the perturbations remains unknown, so that their temporal frequency cannot be determined. Because the amplitude of the Stokes wave is unknown, its influence on the onset of transition cannot be quantified. Moreover, the Stokes was is not included in the numerical models, so that the fluctuation amplitudes and N-factors derived from the experimental data cannot be directly compared to that numerical prediction if the influence is large. This will be further investigated in section 5.4.

In order to omit the noise and higher harmonics of the forcing frequency in the processed velocity signal, a Butterworth band-pass filter is applied. Figure 5.5 depicts the chosen frequency bounds in yellow, which were set to $[200,\ f_{\text{forcing}} + 20]$ Hz. This results in a filter width with a magnitude order of 100 Hz for all forcing frequencies. It was found, that 290 Hz fit the transition front in the infrared camera's field of view best. The flow velocity and temperature measurements recorded at this frequency are used to obtain the results in section 5.4, unless stated otherwise.

5.2.3 Thermal imaging of the transition front by infrared thermography

The beginning of flow transition was captured in the infrared thermography images of the cooled insert. The field of view almost entirely occupied by streaks in the streamwise direction, see figure 5.7 for two examples. All examined thermal images are included in Appendix D.

Streaks are a characteristic of the onset of transition by T–S waves and were therefore expected. It is likely that there are standing waves of higher harmonics of the transmitted acoustic frequency between the test section walls. Each wave causes a spanwise-periodic pattern of regions where the pressure in the boundary layer in relatively highly fluctuating. As a consequence, spanwise velocity fluctuations occur in the in-between regions, so that the flow is more susceptible to the formation of instabilities in these regions. This may cause a specific pattern in the transition region for each forcing frequency.

The presence of long streaks somewhat obstructs the transition front, making it less straightforward to assign a single streamwise location to it. Moreover, the transition front appears to be slightly skewed, so that it does not have a constant x-coordinate. This makes it especially difficult to define the streamwise transition front location from the infrared images. The two-dimensional thermal images are therefore not further used for the comparison between the different thermal boundary condition condition cases. They will be used to assess the state of transition on the various streamwise stations at which the velocity and temperature are recorded. This is elaborated on in the subsection that follows.

5.3 Reconstruction of the boundary layer flowfield

From the infrared thermography images (see for example figure 5.7), it becomes clear that turbulent structures that cause frictional heating of the wall are not yet present at $x = 430$ mm, but they are seen at $x = 530$ mm. The same thing is recognized in the discrete Fourier transforms in figure 5.5, showing relatively high amplitude peaks at frequencies other than the initial perturbation frequency at the downstream station, whereas the spectrum is almost clear of noise at $x = 340$ mm and $x = 430$ mm. These observed differences between the two investigated stations on the cooled part of the flat plate, indicate that the boundary layer transition phenomena can be assumed to behave linearly at the upstream station, and have begun to show non-linearities at the downstream station. The normalized velocity and temperature profiles obtained at the two streamwise stations on the cooled insert at an exemplary wall-to-freestream temperature ratio of $T_w/T_\infty = 0.9745$, are compared in figure 5.8. The normalized shape functions at the same temperature ratio are plotted in figure 5.9. Similarly to the wall coordinate plots in subsection 5.2.1, the velocity profile complies well with the Blasius solution at $x = 430$ mm, but deviates

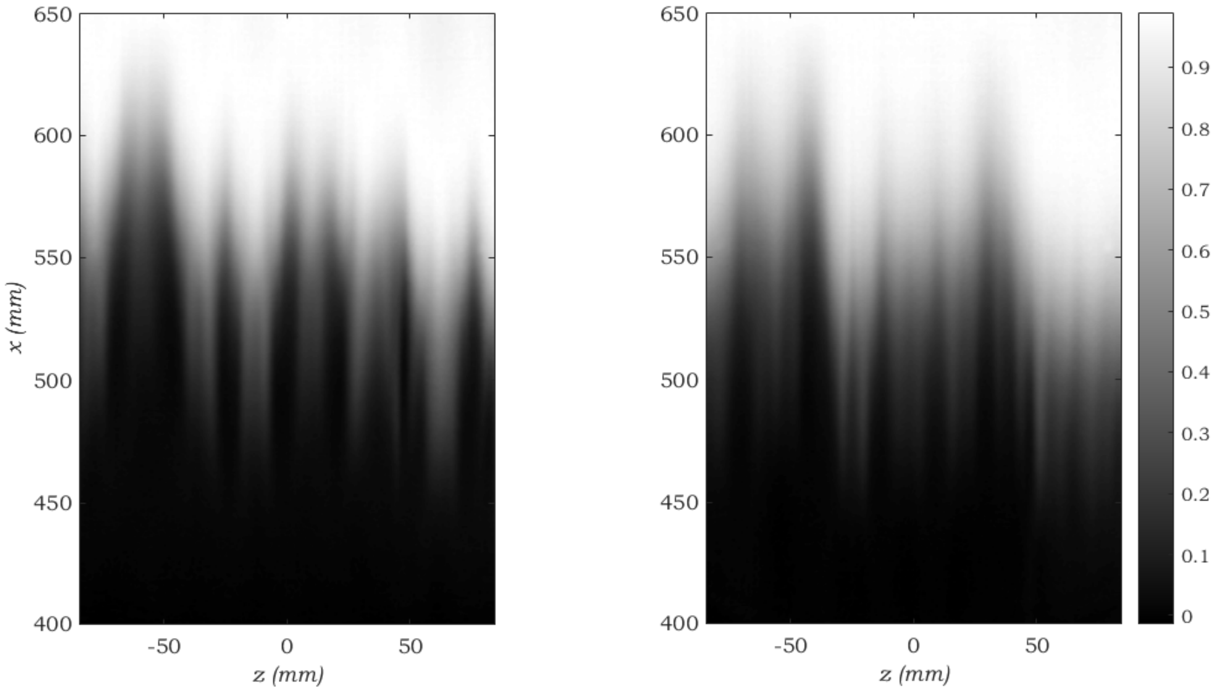

(a) f = 270 Hz (b) f = 330 Hz

Figure 5.7: Example thermal images of part of the cooled flat plate with acoustic forcing at two different frequencies.

from it at x = 530 mm. In the velocity shape function at the more upstream location, a T–S wave is recognized where the shape functions show a second lump, with a peak fluctuation amplitude located around $\eta = 1$. The characteristic T–S wave shape has disappeared from the plot at x = 530 mm, indicating that non-linear flow phenomena have taken over. The fluctuations can no longer be predicted by the linear solver at this point. Here, the velocity and temperature shape functions are highly correlated, adverting to turbulent structures in which the two quantities are coupled through convective contributions. (Had the measurements been simultaneous, the two shape functions would possibly coincide.) This confirms the differences in the boundary layer character between the two station that was observed in the infrared images and the spectral representations.

It is thus safe to state that the linear region of the boundary layer ends before it reaches x = 530 mm. The linear region can be reconstructed based on the profiles and shape functions obtained from the experimental data, which show good correspondence with the numerical predictions for all examined wall temperatures. Therefore, as expected, the linear region can be accurately modeled using the compressible boundary layer and linear stability solver for the current range of wall and freestream temperatures.

A visualisation of the boundary layer's characteristics is presented schematically in figure 5.10.

The profiles in figure 5.8 had already shown that the velocity boundary layer is much thicker the thermal boundary layer. When the profiles are compared to the shape functions, it becomes apparent that the T–waves are located above the thermal boundary layer. This explains why they cannot be captured by means of temperature measurements alone—something that would have been possible if they were inside the thermal boundary layer, as they carry mass. It is however not excluded that T–S waves can be detected in the temperature shape functions of a boundary layer with a much lower wall-to-freestream temperature ratio is a low-speed freestream. What further stands out, is that the thermal boundary layer is almost symmetrical in wall normal-direction in terms of perturbation amplitude, having its peak fluctuation value around 50% of its thickness. The wall-normal distance where the temperature

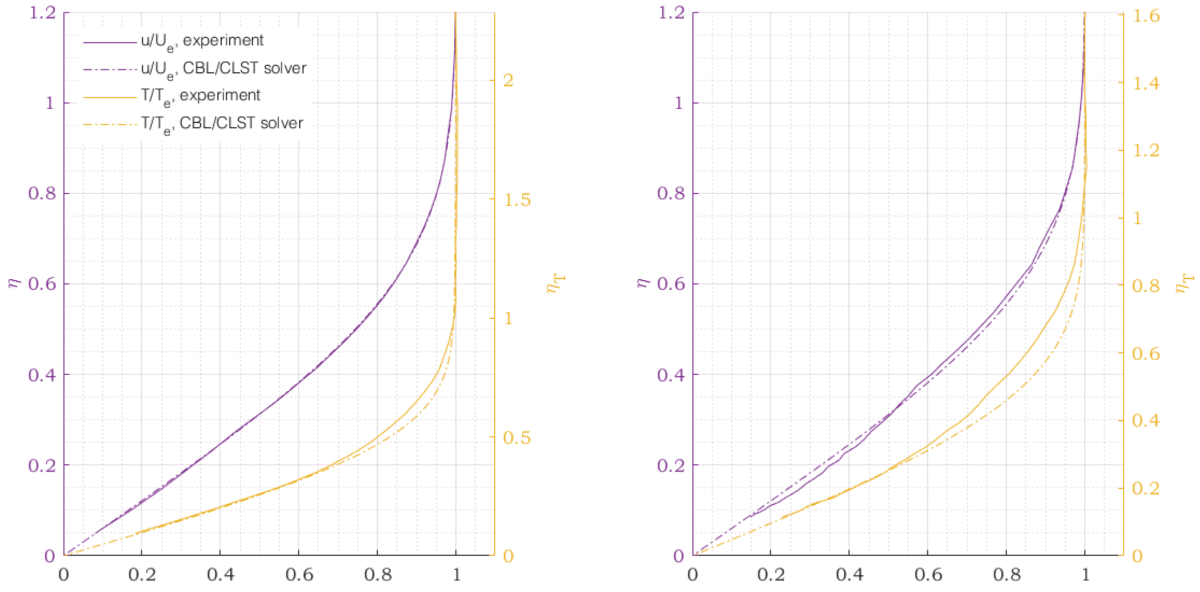

(a) x = 430 mm

(b) x = 530 mm

Figure 5.8: Normalized velocity and temperature profiles at two different streamwise stations on the cooled insert

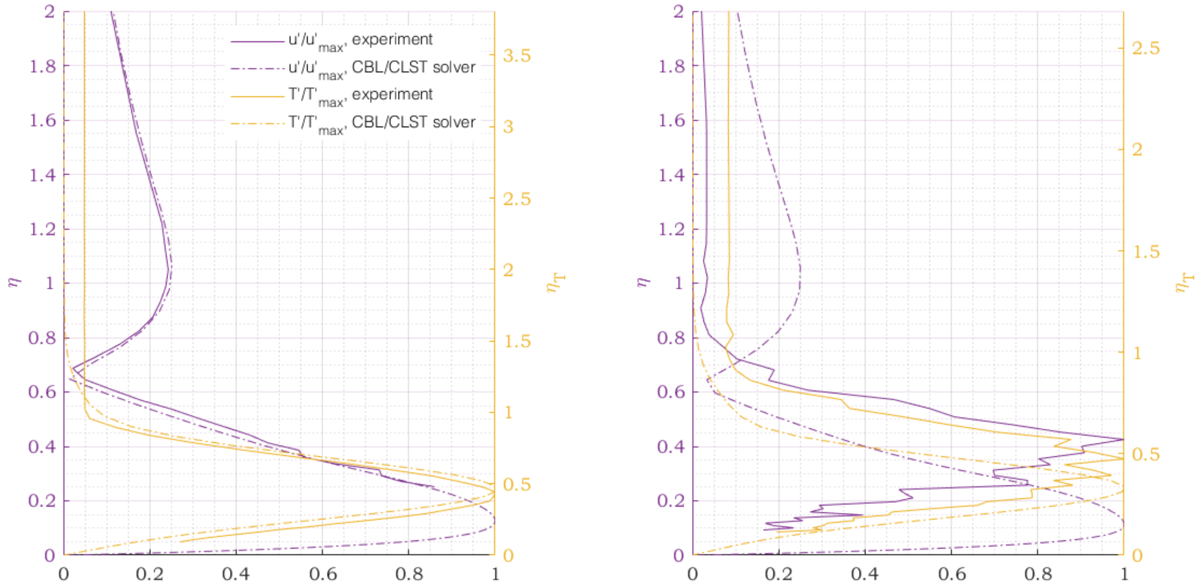

(a) x = 430 mm

(b) x = 530 mm

Figure 5.9: Normalized velocity and temperature shape functions at two different streamwise stations on the cooled insert

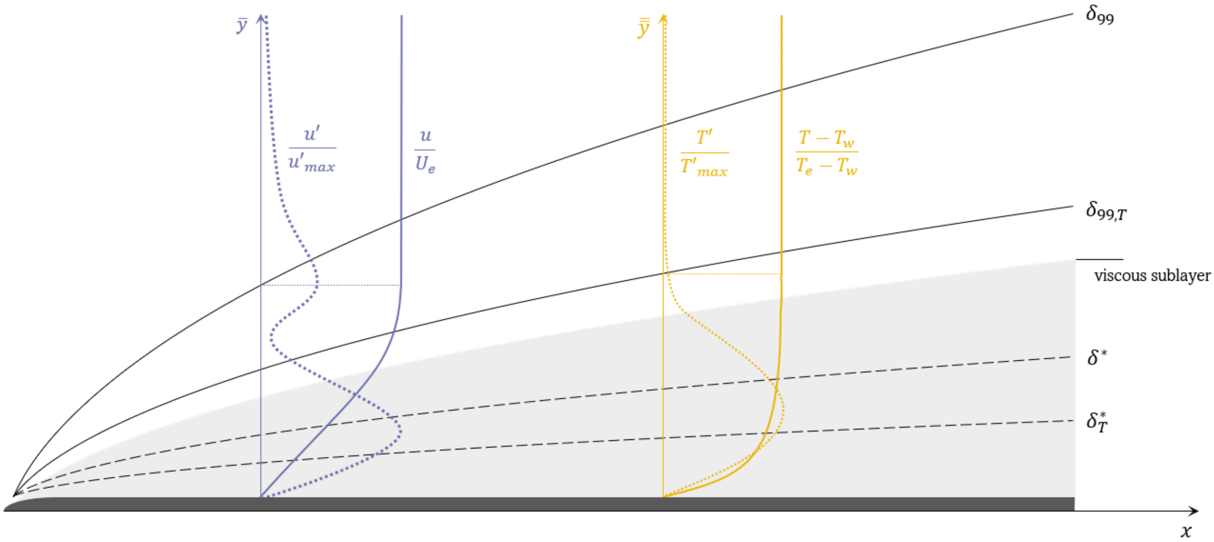

Figure 5.10: Schematic reconstruction of the linear region of the cooled flat-plate boundary layer

fluctuations start to deviate from the freestream fluctuation magnitude coincides with the 99% thermal boundary layer thickness, which nearly coincides with the viscous sublayer thickness.

5.4 The effects of wall cooling on stability and transition

5.4.1 Modification of the transition location from the observed wall temperature increase

The curves in figure 5.11 show the background-corrected temperature increase along the wall, ΔT^*, for several of the examined perturbation frequencies. Large images of the curves for each of the examined frequencies are included in Appendix D, as well as a plot including the standard deviations of the separate thermography recordings. Note that these are large compared to the mean plot lines, which indicates that results derived from this data are to be interpreted with care.

The locations of the maximum gradients of these curves appear to have no significant correlation with wall-to-freestream temperature ratio. This becomes clearer from figure 5.12, in which the relative average x-location of the maximum temperature gradient over all perturbation frequencies is plotted against T_w/T_∞. The values of x are normalized with the mean location of the maximum gradient for the least cooled-down wall, which serves as the reference case here. Standard deviations above and below the means are included in the plot. Figure 5.12 shows that all locations of the maximum temperature gradient are close to the reference location, and there is no detectable relation with the wall-to-freestream temperature ratio. It should be noted, that the magnitudes of the standard deviation increase with decreasing temperature ratio, which indicates that the uncertainty of the measurement is somehow related to the absolute heat build-up at the wall.

The streamwise location where 99% of the maximum measured temperature is reached, seems to increase with decreasing wall-to-freestream temperature ratio for the various perturbation frequencies. Figure 5.13 points out that this is true on average, with the exception of the case $T_w/T_\infty = 0.9661$.The average location where $\Delta T^* = .99\Delta T^*_{\mathrm{max}}$ is here referred to as $x_{.99}$ and is plotted in the figure against the wall-to-freestream temperature ratio. Again, the values of x are averaged over all frequencies and

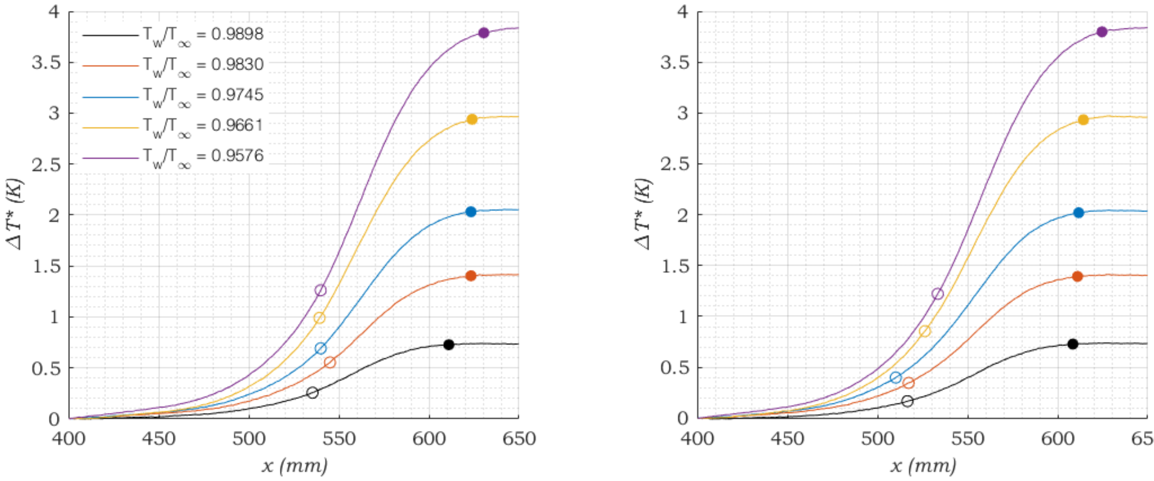

(a) f = 285 Hz (b) f = 290 Hz

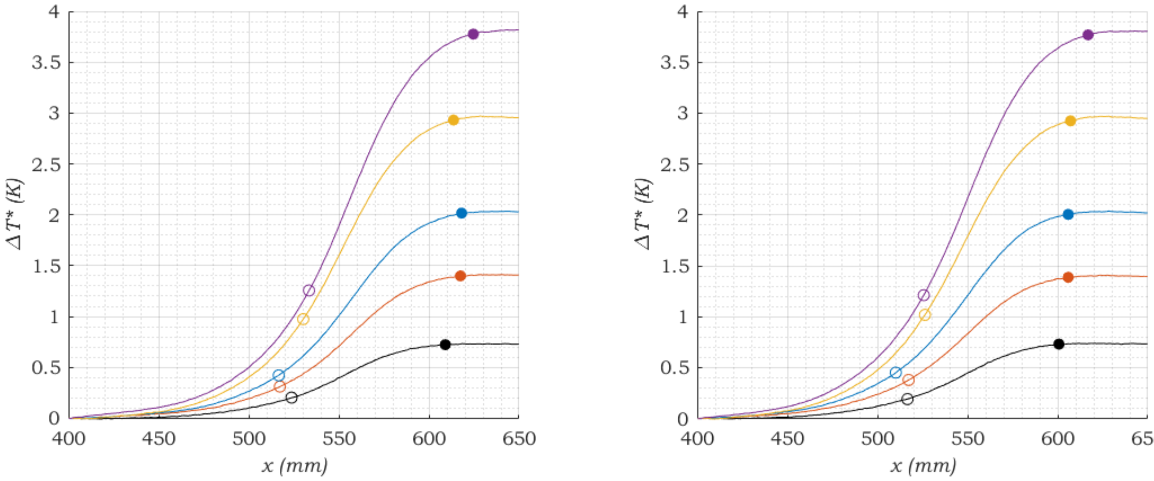

(c) f = 295 Hz (d) f = 300 Hz

Figure 5.11: Smoothed plots of the difference between measurement and background (speaker-off) thermography data, averaged over the span z, for different forcing frequencies f. Maximum gradients of the plotted lines are indicated by open circles ($\circ$); the points where 99% of their maximum values are reached are marked by closed circles ($\bullet$).

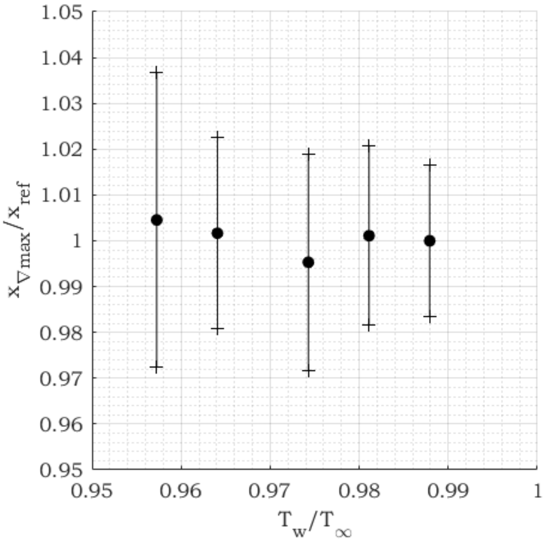

Figure 5.12: Relative locations of the x-station where 99% of the temperature increase is reached

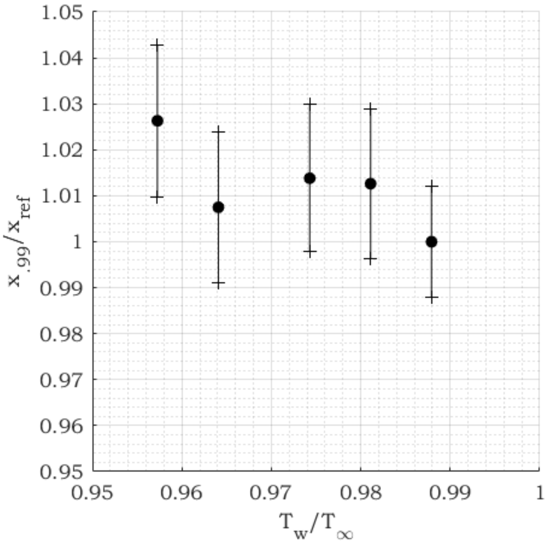

Figure 5.13: Relative locations of the x-station where the gradient of the temperature distribution is at its maximum

normalized. The seemingly inverse relation implies that transition is delayed by wall-cooling. A trend is visible, although no significant correlation can be derived from this plot.

5.4.2 Relative amplitude of the velocity and temperature perturbations

The amplitudes of the highest peaks detected in the FFT representations of the velocity are extracted at each wall-normal coordinate. The resulting profiles are the shape functions, depicted in figure 5.15 for each streamwise station and the highest and lowest wall-to-freestream temperature ratios on the insert.

At $x = 430$ mm, a T–S wave is recognized above approximately $\eta = 0.7$, with its peak amplitude just above $\eta = 1$. The lower lumps in the shape functions are due to the turbulent fluctuations in the viscous sublayer. The measured peak amplitudes in both lumps are compared for all wall-to-freestream temperature ratios in figure 5.16a. This comparison shows, that the amplitudes measured near the wall show no correlation with the wall temperature. The amplitudes of the T–waves, however, decrease with the wall temperature. A trend becomes even clearer further downstream, see figure 5.16b. (Note that the steps on the vertical axes are larger than in figure 5.16a. Even though T–S waves cannot be distinguished in the shape functions —on the contrary: the relative velocity fluctuations are close to zero at the y-coordinates where the lumps were located at $x = 430$ mm—the correlation between these small amplitudes and the wall temperature is even more pronounced here. The location of the single lump at $x = 530$ mm does not coincide with the viscous sublayer. The upper line in figure 5.16b shows the highest amplitudes measured in the spectrum, globally. With the exception of one outlier, a strong decay of the amplitude with decreasing wall temperature is observed. This means that the intensity of the non-linear fluctuations downstream, is affected by the wall temperature as well.

Spectral representations of the velocity fluctuations in the T–S wave and the non-linear region, are provided in the form of spectral density estimates in figures D.3 and D.4 of Appendix D. The pseudo-spectral density (PSD) of the velocity signal was estimated according to Welch's method [80]. Both images indicate that the spectral density of frequencies around that of the T–S wave decreases with the

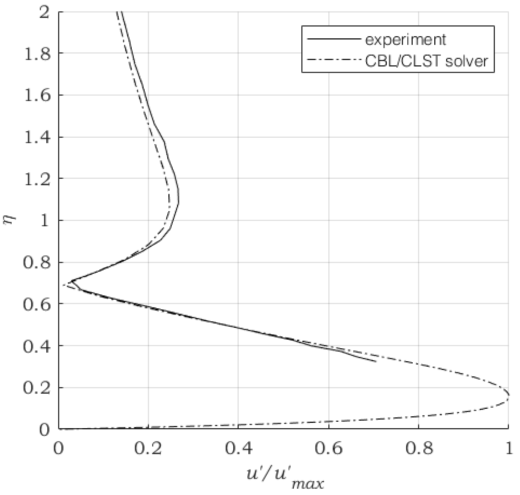

(a) x = 340 mm, T_w/T_∞=1

Figure 5.15: Velocity shape functions obtained from experimental data compared to the outcomes of the CBL/CLST solvers, at different streamwise distances from the plate leading edge and for two different wall-to-freestream temperature ratios.

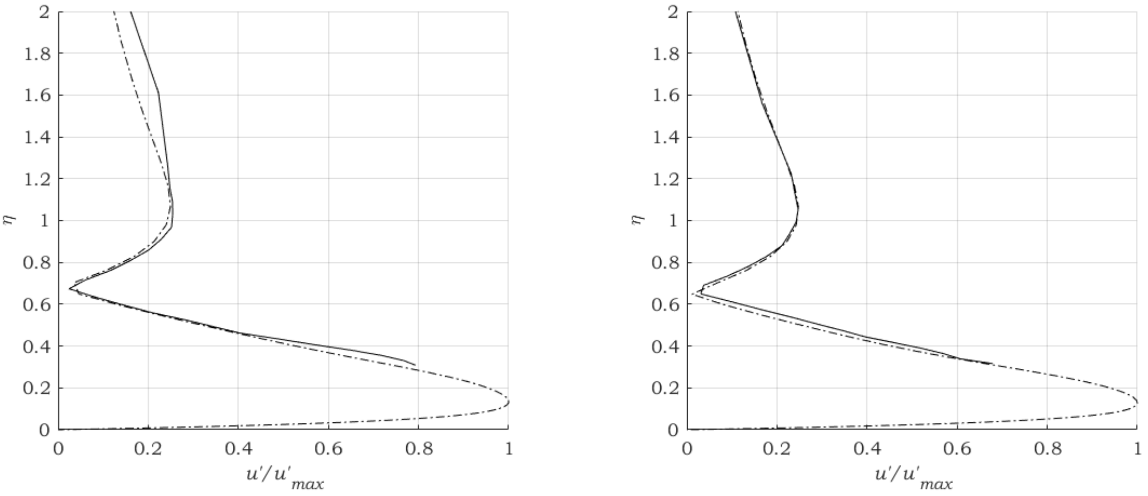

(a) x = 430 mm, T_w/T_∞=1

(b) x = 430 mm, T_w/T_∞=0.9576

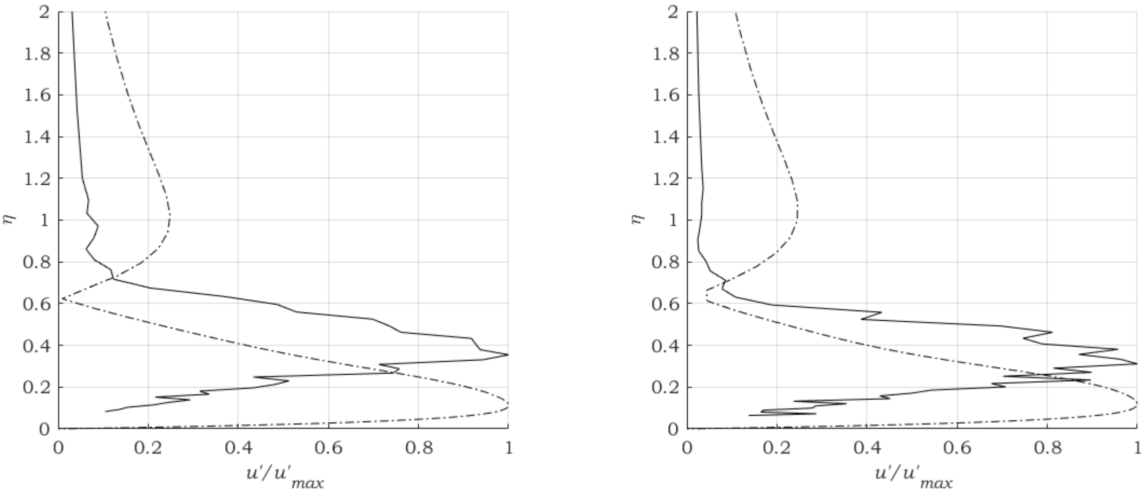

(c) x = 530 mm, T_w/T_∞=1

(d) x = 530 mm, T_w/T_∞=0.9576

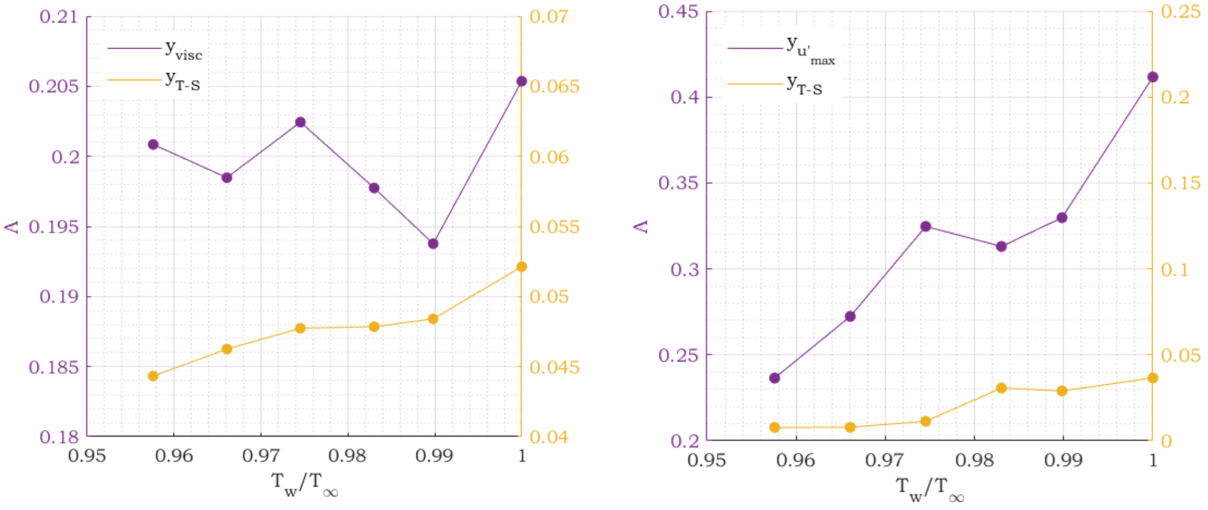

(a) x = 430 mm

(b) x = 430 mm

Figure 5.16: Peak amplitudes of the measured velocity fluctuations

wall temperature, but they do not provide an equally strong correlation as the peak amplitude method.

The correlation between velocity fluctuation amplitude and wall-to-freestream temperature ratio points at a stabilizing effect of wall cooling, which becomes more pronounced as the flow travels in streamwise direction. This importance of the streamwise development of the fluctuations becomes apparent in the following subsection, where N-factors are derived.

5.4.3 Growth rate of the velocity perturbation amplitude

In figure 5.17, the N-factors obtained from the experimental data are compared to the predictions made using both the incompressible and compressible stability for the boundary conditions of the experiment.

Since the amplitudes of the initial velocity perturbations during the wind tunnel experiment are not known, a reference amplitude is determined from the model solution by projecting the N-factor at x = 340 mm onto the solution. Since:

$$N|_{x=340} = \ln\left(\frac{A|_{x=340}}{A_0}\right), \tag{38}$$

the value of A_0 can be derived, assuming that the solver solution is correct at this x-location. A_0 is used as the reference amplitude to compute the N-factors at x = 430 mm from the measured amplitudes at those stations. These semi-experimental N-factors are denoted with an asterisk (*). Semi-experimental N-factors at x = 530 mm are omitted in figure 5.17, since this station is assumed to be in the non-linear region. They will be discussed later on in this subsection.

The incompressible N-factor distributions are nearly equal for all six cases, implying that the wall-to-freestream temperature ratio is of little influence on the perturbation amplitude growth when an incompressible approach is taken. It was expected in advance, that an incompressible model would suffice for Mach numbers as low as they were during the wind tunnel experiment, and that the addition of compressible features to the computation would therefore not change the outcomes significantly. However, even in the case that $T_w = T_\infty$, the N-factor output from ILST and CLST show considerable differences. This may be attributed to the two distinct evaluation methods for the inflow profiles inhabited in the two solvers. The same Hartree parameter serves as an input to both solvers, but results in slightly different

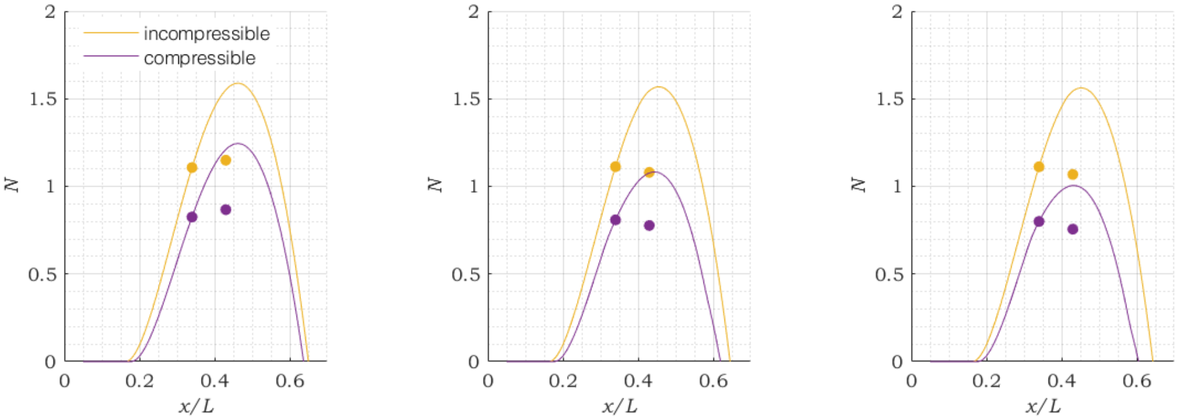

(a) T_w/T_∞ = 1 (b) T_w/T_∞ = 0.9898 (c) T_w/T_∞ = 0.9830

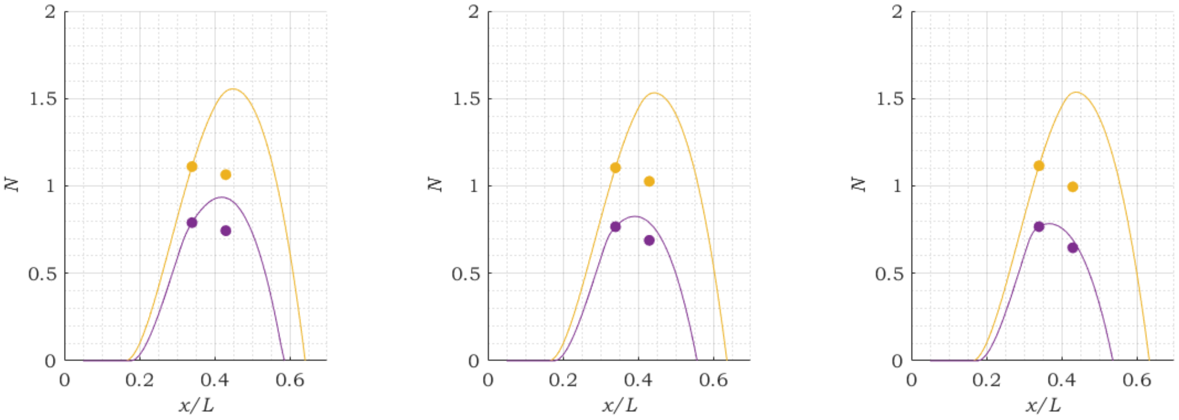

(d) T_w/T_∞ = 0.9745 (e) T_w/T_∞ = 0.9661 (f) T_w/T_∞ = 0.9576

Figure 5.17: Comparison of the N-factors found in the experiment (•) with those predicted by the ILST and CLST solver

inflow profiles depending on the compressibility assumption.

Furthermore, the difference between the compressible and incompressible solution increases as the temperature ratio moves away from 1. This is explained by the variable-property feature of the compressible solver. Where the ILST requires constant fluid properties, the CLST allows for temperature-dependencies. Variable fluid properties influence the local stability of a boundary layer even when the incompressible assumption is verified. This is clear to see from the Orr—Sommerfeld equation, which contains a constant kinematic viscosity ν. Would its magnitude be considered variable already in the streamwise direction alone, the equation would yield a different value of α at discrete streamwise stations than it would for a constant ν. Variable fluid properties are of even bigger influence in the boundary layer's transitional region. Transitional flow phenomena such as T–S waves entail local density gradients. The compressible solver, if applied with sufficient resolution, accounts for this. (Later on, when a turbulent mixing region is entered, this effect becomes less significant.) Although the aforementioned effects are technically not compressibility effects, they do make the CLST more suitable for the prediction of non-adiabatic wall flows. This is supported by the observation that the experimentally obtained N-factors show better correspondence with the compressible than the incompressible solution.

Some of the values of N^* are reasonably on-point, but significant discrepancies are seen between model solution and measurement for all wall-to-freestream temperature ratios. The most likely explanation for this, is the presence of a Stokes wave in the test section. If the amplitude of this wave was large, than most unstable modes were already much more amplified at the reference station $x = 340$ than predicted by the solver. This is supported by the observation that all computed N-factors are very low for a transitional boundary layer when compared to earlier findings: the onset of transition on an adiabatic flat plate is expected at N =7.8 [14], whereas the model predicts values no larger than 1.6. This means that the boundary layer was far from transitioning without the use of a forcing mechanism, and confirms the hypothesis that the Stokes wave has a much higher amplitude than the initial perturbations of the boundary layer velocity. It it then perfectly sensible, that the values of N^* do not follow the predicted curves, as their computation method relies on the N-factor at $x = 340$ mm. It also explains why the absolute amplitudes of velocity fluctuation at the locations of the T–S wave appear realistic, but the resulting estimated N-factors are off.

In general, the N-factors found semi-experimentally are closer to those predicted by the compressible solver than to the ILST outcomes. This is to be expected, since, as explained above, the CLST takes the temperature-dependence of fluid properties into account, and is therefore inherently better suited to model a flow of varying temperature. As a consequence of this difference between the two solvers, the comparisons in figure 5.17 can provide no decisive answer when it comes to the importance of isolated compressibility effects in the modeling of the current flows. This may well be due to the quality of the data recorded in this experiment, which will be elaborated on in chapter 7.

Figure 5.18 includes all values of N^* found at both stations on the cooled insert. What stands out from figure 5.18a, is that the solution provided by the CLST grows closer to the factors derived from the experimental data as the wall temperature goes down. It should be noted that the absolute values of the latter are highly dependent on the estimate for A_0. The method of computing A_0 is sensitive to error, as it is not a given that the peak amplitudes from the solver are correct at $x = 340$ mm. An error in the reference amplitude naturally affects the reliability of the N-factors calculated at stations further downstream. A different estimate could cause the order of the plots to flip, and their relative difference to reverse. What should also be noted, is that figure 5.18b contains three negative values of N^*. This implies that perturbations of the velocity will be damped out again at this station, which is not physically possible is this case, considered that transition has already set on here.

Moreover, the anemometry is only performed at a single spanwise location. When looking at the infrared images in figure 5.7, it becomes clear that this location can be crucial for the amplification factor found. Since the locations of the streaks are time-invariant, there is no measurement time threshold that can cancel out this problem.

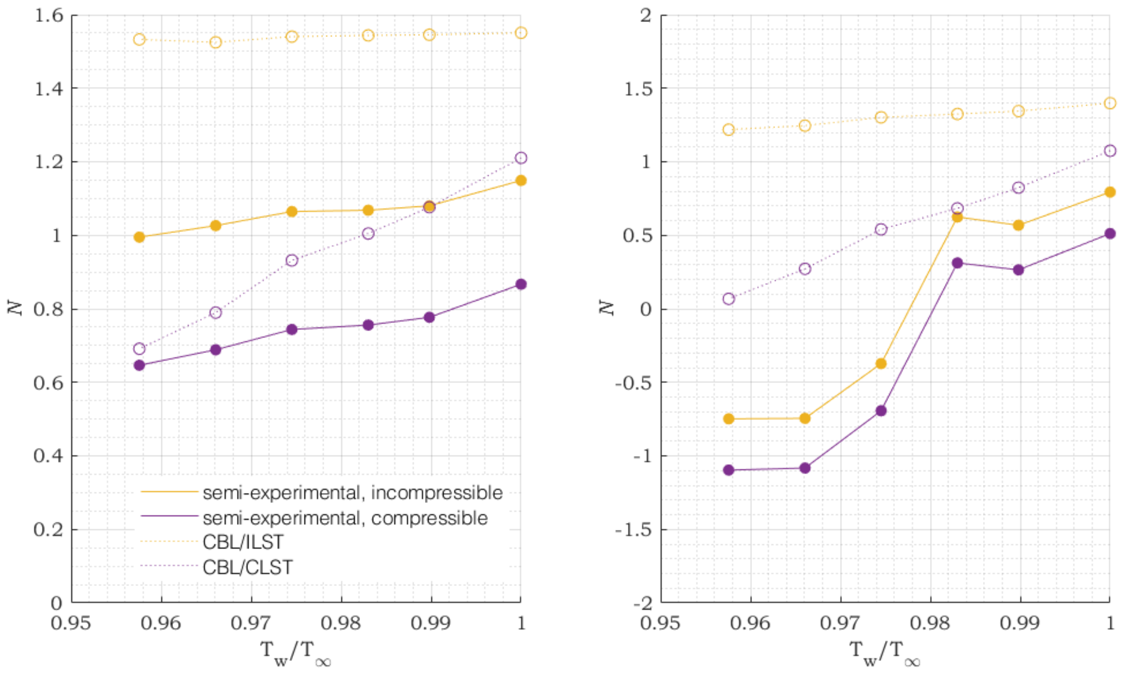

(a) x = 430 mm

(b) x = 530 mm

Figure 5.18: N-factors obtained from experimental data at the height of the T–S wave for different wall-to-freestream temperature ratios

An overview of all the streamwise locations are listed that were expected to be indicators for the boundary layer transition, can be found in table 1. In table 1. Model outcomes are denoted with a hat (ˆ).

T_w/T_∞	$x_{\nabla_{\max}}$	$x_{.99}$	$\hat{x}_{\text{max. } N}$		$\hat{x}_{N=0}$	
			incomp.	comp.	incomp.	comp.
1	—	—	466.8	461.9	650.1	650.5
0.9898	521.7	603.4	457.4	442.7	645.3	632.5
0.9839	522.3	611.1	447.9	433.2	643.5	621.5
0.9745	519.2	611.8	447.9	420.8	641.6	607.1
0.9661	522.5	608.0	447.9	396.2	636.9	571.5
0.9576	524.1	619.3	438.4	375.7	634.0	552.8

Table 1: Characteristic streamwise locations resulting from the experiment and the model computations for the different cooling cases. All locations are in mm, measured from the plate leading edge.

6 Conclusions

A combined experimental and computational study was carried out to identify the effects of surface cooling on the stability of the boundary layer on a flat plate in an incompressible, uniform freestream. The methodology and results of a wind tunnel experiment and a discrete computational model were compared. Emphasis was put in particular on the influence of compressibility effects on the stability of a non-adiabatic wall flow, and on the consequences of the non-adiabatic wall condition for the accuracy of the computational model and for the practicalities regarding the experiment.

The computational model used, consists of a compressible Navier–Stokes solver to provide the velocity and temperature field solutions for the boundary layer, combined with two versions of a linear stability solver: one incompressible and one compressible formulation. The latter takes the temperature dependence of the fluid's density, viscosity and heat capacity into account, whereas the incompressible solver assumes these properties to be constant.

The N-factors resulting from the two different stability models deviate increasingly as the wall-to-freestream temperature ratio moves away from 1, when the Mach number is kept at 0.05. Since no significant compressibility effects can be expected at this very low Mach number, the discrepancy is attributed to the temperature dependence of the aforementioned fluid properties.

The experiment was conducted in an anechoic, low-turbulence wind tunnel at the same Mach number of 0.05. Five wall-to-freestream temperature ratios were compared using infrared thermography in an attempt to identify the laminar-turbulent transition front. At the same temperature ratios, plus the supplementary case of equal wall and freestream temperature, velocity and temperature measurements were recorded by means of constant-current and constant-temperature anemometry, respectively.

The identification of the transition front turned out not to be feasible on the basis of two-dimensional infrared thermography images under the experimental conditions. The uncertainty of the measurements is large, and due to the appearance of streaks taking up a substantial part of the field of view, the transition front is poorly defined by the thermal data. The computation of a spanwise mean wall temperature increase in combination with a smoothing procedure of the data, however, does provide insight into the modification of the transition front location. A slight downstream movement of the front is observed as the wall-to freestream temperature ratio decreases. Caution is advised though, as the data smoothing method is somewhat artificial, and the significance of the correlation is rather weak.

The procedure to correct for measurement errors caused by conductive heat transfer at the wall that was applied to the anemometry data, yields accurate results. The boundary layer was reconstructed based on the corrected velocity and temperature data, showing that T–S waves occur outside the thermal boundary layer. As soon as the transition is overtaken by higher modes of instability, the linear stability solver is no longer an accurate predictor for the shape functions, as was expected. Comparisons of the velocity and temperature fluctuations in the form of shape functions, have shown that the velocity perturbations are paired with convective heat transfer for all flow structures observed in the thermal boundary layer.

The amplitudes of the measured velocity fluctuations at the wall-normal location of a T–S wave, as well as the maximum amplitudes throughout the boundary layer, decrease as the the wall-to-freestream temperature ratio is lowered. This effect becomes more pronounced as the flow moves downstream. Although the N-factors estimated from the experimental data do not agree very well with either solver prediction, the best correspondence is found with the compressible stability model. This is most likely to be attributes to its variable fluid property feature. The N-factors predicted by the solvers were theoretically too low to cause transition to turbulence. This can be an explanation for the discrepancy between solver and experimental results downstream. Furthermore, it is not excluded, that more extensive measurements will lead to better overall correspondence with the solver outcomes.

The velocity perturbation amplitudes and N-factors were shown to decrease with the wall-to-freestream temperature ratio, both just downstream of the beginning of the cooled plate insert and at the x-station where transition has well set on. At the latter station, T–S waves are no longer distinguishable in the velocity shape functions. Wall-cooling thus stabilizes the boundary layer both in the linear and in the non-linear region. It is therefore concluded, that the cooling of a flat plate has the potential to delay transition initiated by T–S waves.

7 Recommendations for future research

7.1 Improvements of the current methodology

Various shortcomings of the methodology employed were encountered in the course of the research. These were often inherent to the methods and could not be overcome on the spot. This subsection lists the changes to the methodology recommended to come closer to achieving the current research goal.

A few adaptations to the computational model are proposed, that are expected to make them either more accurate or more user-friendly.

Firstly, as was emphasised before, the assumption of constant fluid properties poses a problem for the modeling of a non-adiabatic wall flow, even when it can be considered incompressible. For this reason, the incompressible model does not provide an accurate solution for this type of flow. A hybrid code featuring this temperature-dependence without computing the full compressible equations might serve as an alternative. The simplest approximation would be the solution to the Orr–Sommerfeld equation at discrete streamwise stations, where the fluid properties are at the estimated average temperature in the boundary layer. It can, however, be argued that this is not the most effective upgrade to the model, since the wall-normal gradient of the temperature is especially large for a cooled-wall flow. Another option would be to use the compressible perturbation equations, but to make significant simplifications in the energy equation. For low Mach numbers, all terms containing the factor M^2 may be neglected, so that the remaining equation is quickly evaluated. Furthermore, the variable fluid properties can be assumed to be linearly dependent on the temperature for small temperature changes, which somewhat simplifies all five perturbation equations from a computational point of view.

Suggested improvements to the code in terms of convenience of use, include the establishment of handles for the numerical input parameters. Examples of these are parameters governing the Chebyshev collocation process and the grid resolution. These inputs determine strongly on a combination of physical variables, such as the freestream Mach number and the body's pressure distribution, but are known to have an optimum value. Wrong choices result in erroneous representation of the stability, because amplified modes may remain undetected. Carefully mapping the consequences of the choice of parameters will help shape a pattern for successful modeling and prediction of stability measures.

The quality of the experimentally found data could have been improved in a number of ways. First and foremost, more effort should be put in the recording of reference measurements, which were now left out mainly due to time constraints. At the reference location upstream of the cooled insert in the flat plate, anemometry data was only acquired with the cooling system off. For proper reference data, measurements should have been done at all wall temperature settings. Moreover, the streamwise location of the reference point could have been chosen more usefully. When looking at the stability solutions from the computational models, it is easily seen that the N-factor is already larger than zero at x = 340 mm. This means that there is already considerable amplification of instabilities happening here. Therefore, the reference perturbation amplitude A_0 inevitably needs to be derived from the model prediction, causing possible errors in the resulting (semi-)experimental N-factors. The velocity fluctuation amplitude measured in the freestream at x = 340 mm was tested as a candidate for A_0, but this yielding rather unphysical estimations for the N-factor. A measurement at the plate leading edge is therefore proposed for future experiments.

The formation of long streaks was shown to obstruct the transition front on the cooled insert during infrared thermography measurements. Although not directly visible, these streaks also quite certainly affect the data obtained by anemometry. Because the streaks are an inherent characteristic of the onset of turbulence, they can never be fully omitted. It is, however, worth a try to shorten them by using a different forcing mechanism. Acoustic forcing poses another difficulty for the understanding of the recorded data, namely the presence of a Stokes wave during the recordings. The influence of the Stokes wave on the amplification of perturbations is not inhabited in the numerical solver, and cannot be distinguished in a spectral analysis of the experimental results. Examples of alternative transition forcing methods include tripping wire and other roughness elements, plasma actuators and adaptations made to the streamwise pressure gradient. The latter is often achieved only by changing the geometry of the model or test section, which may come with little freedom in their form. Roughness elements offer a wider range of geometry and placement options, but these are not quickly altered during a wind tunnel experiment in a closed test section. Plasma actuators thus turn out to be the most practical forcing method: they are remotely controllable and minimally affect the test setup.

A particular and yet unresolved problem was encountered in the measurement of the boundary layer temperature: the thermal boundary layer profile did not meet the temperatures measured simultaneously by infrared thermography when extrapolated to the wall. This is especially peculiar, since both the constant-current anemometer and the infrared camera were calibrated by means of the same Pt100 sensor. The difference between the filmed wall temperature and the extrapolated value ran up to 5 K for the lowest wall temperature, implying an uncertainty of nearly 2% in the wall-to-freestream temperature ratio. Because the profiles were used for the determination of air properties and for the correction procedure for heat transfer from hot wire to wall, measurement errors will have propagated in the velocity and stability results—albeit to a very small extent.

Lastly, a better understanding of the flow's transition behaviour would have been possible if particle image velocimetry (PIV) was employed to obtain two-dimensional velocity fields. This would have enabled visualization of the T–S waves, the occurrence of which is now derived from shape functions at single streamwise stations. The development of the boundary layer and its inhabited flow structures leaves some room for guesswork now. PIV measurements would also provide information on the phase velocity of the amplified modes. Nevertheless, sufficient data was collected to draw valid conclusions from and thereby answer the research question.

7.2 Extensions toward applicability to aircraft design

As discussed before, the current research focuses on what is regarded the simplest case of a cooled-wall flow, in terms of stability. It is intended to pave the way for the study of gradually more complex flow conditions, eventually leading to an understanding of the effects of cooling of aerodynamic surfaces in aircraft under cruise conditions. A pathway is proposed of the research steps towards this understanding and the challenges that they entail.

The objective of the train of researches as a whole, is to map how certain characteristics of the flow translate to the transition behaviour of the boundary layer. In the most ideal case, the effects of these characteristics on the stability are independent of each other, so that each one of them comes with a separate change or addition to the numerical model. Three key extensions of the flow to cruise conditions are highlighted: Mach number increase, three-dimensional flow and temperature decrease. It will become clear that not all effects of these adaptations can be isolated.

The real consequences of air compressibility as modeled by the compressible flow equations, can only be verified by means of an experiment at a higher Mach number. Cruise conditions for modern aircraft often involve Mach numbers in the transonic regime, e.g. above 0.8. Apart from the highly compressible flow that this brings about, it also means that air accelerations due to geometry may cause locally (super)sonic flow. These two characteristics are closely related to temperature when it comes to stability. The share of influence of the temperature-dependence of fluid properties with respect to compressibility will change in the perturbations equations. It was already discussed in chapter 2, that the consequences for the stability of a cooled-wall flow in the supersonic case may be opposite to those holding in the subsonic regime. This asks for a customised discretization of the modeled domain.

The geometry of the cooled body will affect the stability situation in more ways than by inducing possible supersonic regions alone. It is well known in the study of aircraft aerodynamics, that the streamwise pressure distribution over a surface is of large influence on the transition and separation of the boundary layer. What might play an even larger role in the case of surface-cooling, are the three-dimensional flow phenomena that occur over swept wings. At a certain sweep angle, crossflow instabilities will replace T–S waves and overtake the onset of transition. The non-adiabatic wall condition is expected to change this angle. Crossflow instabilities and T–S waves do not have an equal effect on transition and viscous drag. For accurate flow modeling, it is important to know what the relation between wall-cooling and ”critical” sweep angle is, so that the correct instability type and transition location are predicted.

Last but definitely not least, the thermal cruise conditions are yet to be mimicked to validate the numerical model under these circumstances. It is important to note, that not only a lower wall-to-freestream temperature is desired, but the freestream temperature itself also drops significantly at cruise altitude. The latter makes it especially difficult to simulate the flow in a wind tunnel experiment. Temperature controlled low-turbulence tunnels that go down to far below 0^oC are rare. Moreover, the humidity of air at sea level is much higher than that of air at cruise altitude, so that condensation and ice formation will occur in a wind tunnel at temperatures that pose no significant problems up in reality. A dehumidification installation can provide a solution, but it is yet to be found out whether a truly accurate simulation of combined temperature and humidity can be achieved. The more feasible way to go might be to extend experimenting to a point when a correlation between wall-to-freestream temperature ratio and transition delay can be established with sufficient certainty, and to extrapolate this correlation in a numerical model.

In conclusion, transition delay by cooling of the aerodynamic surfaces of operating aircraft proves to depend on many factors. The actual drag reduction resulting from the transition delay requires, again, a different type of model or experiment. Once a drag reduction goal can be coupled to a surface cooling strategy, practical considerations remain. There is quite a wide range of challenges to overcome, ranging from the weight penalty of the cooling installation to the safety regulations around hydrogen. It is this long way ahead, that asks for a pressing continuation of the research on this subject world-wide.

References

[1] Clean Sky 2 Joint Undertaking, “Hydrogen-powered aviation,” 2020.

[2] International Air Transport Association, “Annual review 2022, Environment and sustainability,” 2022, pp. 30–34.

[3] International Civil Aviation Organization Secretariat, “Electric, hybrid, and hydrogen aircraft—state of play,” 2019, pp. 124–130.

[4] J. G. Speight, *Handbook of petroleum product analysis.* John Wiley & Sons, 2015.

[5] D. Cecere, E. Giacomazzi, and A. Ingenito, “A review on hydrogen industrial aerospace applications,” *International journal of hydrogen energy*, vol. 39, pp. 10 731–10 747, 20 2014.

[6] E. Reshotko, “Drag reduction by cooling in hydrogen fueled aircraft,” *Journal of Aircraft*, vol. 16, pp. 584–590, 9 1979.

[7] J. G. Theisen, G. D. Brewer, and L. R. Miranda, “Laminar flow stabilization by surface cooling on hydrogen fueled aircraft,” *AIAA Aircraft Systems and Technology Meeting*, p. 1863, 1979.

[8] G. D. Brewer, R. E. Morris, G. W. Davis, E. F. Versaw, and G. R. Cunnington Jr., “Study of fuel systems for LH_2 fueled subsonic transport aircraft. Volume 1. Final report, September 1976–December 1977,” Lockheed-California Co., Tech. Rep. N-78-31085, 1978.

[9] G. D. Brewer and L. R. Miranda, “Experimental study of achieving laminar flow control by cryogenic wall cooling,” Lockheed-California Co., Tech. Rep. LG29012, 1979.

[10] G. R. Cunnington Jr. and R. T. Parmley, “Aerodynamic surface cooling for laminar flow control for hydrogen-fueled subsonic aircraft,” *SAE Transactions*, vol. 89, pp. 3496–3502, 1980.

[11] L. Lees and C. C. Lin, “Investigation of the stability of the laminar boundary layer in a compressible fluid,” National Advisory Committee for Aeronautics, Tech. Rep. 1115, 1946.

[12] L. Lees, “The stability of the laminar boundary layer in a compressible fluid,” National Advisory Committee for Aeronautics, Tech. Rep. NACA-TR-876, 1947.

[13] G. B. Schubauer and H. K. Skramstad, “Laminar boundary-layer oscillations and transition on a flat plate,” *Journal of research of the National Bureau of Standards*, vol. 38, p. 251, 1947.

[14] J. L. van Ingen, “A suggested semi-empirical method for the calculation of the boundary layer transition region,” *Technische Hogeschool Delft, Vliegtuigbouwkunde, Rapport VTH-74*, 1956.

[15] L. M. Mack, “Boundary layer stability theory,” Jet Propulsion Laboratory, California Institute of Technology, Pasadena, CA, USA, Tech. Rep. JPL Rep. 900-277, 1984.

[16] D. B. Landrum and J. M. Macha, “Influence of a heated leading edge on boundary layer growth, stability, and transition,” in *AIAA 19th Fluid Dynamics, Plasma Dynamics and Lasers Conference*, 1987.

[17] A. V. Dovgal, V. Y. Levchenko, and V. A. Timopeev, “Boundary layer control by a local heating of the wall,” in *Laminar-Turbulent Transition. International Union of Theoretical and Applied Mechanics*, Springer, Berlin, 1990, pp. 113–121.

[18] M. R. Head, “The boundary layer with distributed suction,” Tech. Rep. ARC-RM-2783, 1955.

[19] J. M. Kay, “Boundary layer along a flat plate with uniform suction,” Tech. Rep. ARC-RM-2628, 1948.

[20] J. Wiedemann and K. Gersten, “Drag reduction due to boundary-layer control by combined blowing and suction.,” *AGARD-CP-365*, pp. 14-1–14-10, 1984.

[21] M. H. Bertram, A. M, and A. H. W. Cary Jr., “Experiments with hypersonic turbulent boundary layers on flat plates and delta wings,” AGARD, Tech. Rep. N69-10186 01-01, 1968.

[22] F. Oz, T. E. Goebel, J. S. Jewell, and K. Kara, “Local wall cooling effects on hypersonic boundary-layer stability,” *Journal of Spacecraft and Rockets*, vol. 60, pp. 412–426, 2 2023.

[23] J. D. Anderson Jr., *Introduction to Flight*, 8th ed. McGraw-Hill Education, 2016.

[24] K. O. W. Ball, “Similarity solutions for the compressible laminar boundary layer with heat and mass transfer,” *Physics of Fluids*, vol. 10, pp. 1823–1826, 8 1967.

[25] Y. H. Kuo, “On the flow of an incompressible viscous fluid past a flat plate at moderate reynolds numbers,” *Journal of Mathematics and Physics*, vol. 32, pp. 83–101, 1–4 1953.

[26] H. Schlichting, “Nach. ges. wiss. göttingen,” *Math.-Phys. Klasse*, pp. 181–201, 1933.

[27] H. B. Squire, “On the stability for three-dimensional disturbances of viscous fluid flow between parallel walls,” *Proceedings of the Royal Society of London. Series A, Containing Papers of a Mathematical and Physical Character*, vol. 142, pp. 621–628, 847 1933.

[28] W. Tollmien, “Ein allgemeines kriterium der instabilitat laminarer geschwindingkeitsverteilungen,” *Nachr. Ges. Wiss. G¨ottingen, Math. Phys. Klasse, Fachgruppe I*, vol. 1, pp. 79–114, 1935.

[29] Lord Rayleigh, “On the stability or instability of certain fluid motions,” *Proc. London Math. Soc. and Scientific Papers*, vol. 9, pp. 57–70, 1880.

[30] W. Heisenberg, “Uber stabilität und turbulenz von flüssigkeitsströmen,” *Ann. d. Phys., Vierte Folge, Bd. 74*, no. 15, pp. 577–627, 1924.

[31] W. Tollmien, “Grenzschichttheorie,” in *Handbuch der Experimentalphysik, IV*, 1931, pp. 239–287.

[32] H. Schlichting, “Zur enstehung der turbulenz bei der plattenströmung,” *Nachrichten der Gesellschaft der Wissenschaften – enshaften zu Göttingen, Mathematisch – Physikalische zu Göttingen, Mathematisch – Physikalische Klasse*, pp. 21–44, 1929.

[33] P. J. Schmid and D. S. Henningson, *Stability and Transition in Shear Flows.* Springer, 2001.

[34] M. Amitay, B. A. Tuna, and H. Dell’Orso, “Identification and mitigation of ts waves using localized dynamic surface modification,” *Physics of Fluids*, vol. 28, 6 2016.

[35] M. Gad-el-Hak, “Introduction to flow control,” in *Flow Control. Lecture Notes in Physics*, vol. 53, 1998, pp. 1–107.

[36] K. Bussmann and H. Münz, “Die stabilität der laminaren reibungsschicht mit absaugung,” *Jb. dt. Luftfahrtforschung I, 36–39*, pp. 458–459, 1942.

[37] E. G. Hauptmann, “The influence of temperature dependent viscosity on laminar boundary-layer stability,” *International Journal of Heat and Mass Transfer*, vol. 11, pp. 1049–1052, 1968.

[38] C. Dunn and C. Lin, “On the stability of the laminar boundary layer in a compressible fluid,” Massachusetts Institute of Technology, Department of Mathematics, Tech. Rep., 1953.

[39] L. I. Boehman and M. C. Mariscalco, “The stability of highly cooled compressible laminar boundary layers,” University of Dayton Research Institute, Tech. Rep. AFFDL-TR-76-148, 1976.

[40] B. S. Ng, “Uniform asymptotic approximations to the solutions od the dunn-lin equations,” *Quarterly of Applied Mathematics*, 1976.

[41] F. T. Smith, “On the non-parallel flow stability of the blasius boundary layer,” *Proceedings of the Royal Society of London. A. Mathematical and Physical Sciences*, vol. 366, pp. 91–109, 1979.

[42] K. Gersten and H. Herwig, “Impuls- und wärrmeübertragung bei variablen stoffwerten für die laminare plattenströmung,” *Wärme- und Stoffübertragung*, vol. 18, pp. 25–25, 1984.

[43] H. Herwig and P. Schäfer, “Influence of variable properties on the stability of two-dimensional boundary layers,” *Journal of Fluid Mechanics*, vol. 243, pp. 1–14, 1992.

[44] A. R. Wazzan, G. Keltner, T. T. Okamura, and A. M. O. Smith, “Spatial stability of stagnation water boundary layers with heat transfer,” *Physics of Fluids*, vol. 15, pp. 2114–2118, 1972.

[45] J. A. Weideman and S. C. Reddy, "A MATLAB differentiation matrix suite," *ACM Transactions on Mathematical Software*, vol. 26, pp. 465–519, 2000.

[46] M. R. Malik, S. Chuang, and M. Y. Hussaini, "Accurate numerical solution of compressible, linear stability equations," *Journal Applied Mathematics and Physics (ZAMP)*, vol. 33, pp. 189–201, 1982.

[47] S. A. Orszag, "Accurate solution of the orr–sommerfeld stability equation," *Journal of Fluid Mechanics*, vol. 50, pp. 689–701, 4 1971.

[48] J. H. Wilkinson, *The algebraic eigenvalue problem.* Oxford University Press, 1965.

[49] M. Gaster, "On the effects of boundary-layer growth on flow stability," *Journal of Fluid Mechanics*, vol. 66, pp. 465–480, 1974.

[50] T. Herbert, "Parabolized stability equations," *Annual Review of Fluid Mechanics*, vol. 29, pp. 245–283, 1 1997.

[51] F. P. Bertolotti and T. Herbert, "Analysis of the linear stability of compressible boundary layers using the pse," *Theoretical Computational Fluid Dynamics*, vol. 3, pp. 117–124, 1991.

[52] F. P. Bertolotti, T. Herbert, and P. R. Spalart, "Linear and nonlinear stability of the blasius boundary layer," *Journal of Fluid Mechanics*, vol. 242, pp. 441–474, 1992.

[53] F. P. Bertolotti, "Linear and nonlinear stability of boundary layers with streamwise varying properties," Ph.D. dissertation, Ohio State University, 1991.

[54] W. Huang and D. M. Sloan, "The pseudospectral method for solving differential eigenvalue problems," *Journal of Computational Physics*, vol. 111, pp. 399–409, 2 1994.

[55] R. Zhao, C. Y. Wen, X. D. Tian, T. H. Long, and W. Yuan, "Numerical simulation of local wall heating and cooling effect on the stability of a hypersonic boundary layer," *International Journal of Heat and Mass Transfer*, vol. 121, pp. 986–998, 2018.

[56] M. Cogo, F. Salvadore, F. Picago, and M. Bernardini, "Direct numerical simulation of supersonic andhypersonic turbulent boundary layers atmoderate-high reynolds numbers andisothermal wall condition," *Journal of Fluid Mechanics*, vol. 945, 2022.

[57] V. R. Guschin and A. V. Fedorov, "Excitation and development of unstable disturbances in supersonic boundary layer," *Fluid Dynamics*, vol. 25, 3 1990.

[58] H. W. Liepmann and G. H. Fila, "Investigations of effects of surface temperature and single roughness elements on boundary-layer transition," National Advisory Comittee for Aeronautics, Tech. Rep. 890, 1947.

[59] L. V. King, "On the convection of heat from small cylinder in a stream of fluid: Determination of the convectional constants of small platinum wires with applications to hot-wire anemometry," *Phil. Trans. Roy. Soc. (London), ser. A*, vol. 214, pp. 373–432, 914.

[60] H. W. Liepmann, "Investigations on laminar boundary-layer stability and transition on curved boundaries," NACA ACR, Tech. Rep. 3H30, 1943.

[61] L. H. Back, R. F. Cuffel, and P. F. Massier, "Effect of wall cooling on the mean structure of a turbulent boundary layer in low-speed gas flow," *International Journal of Heat and Mass Transfer*, vol. 13, pp. 1029–1047, 6 1970.

[62] N. S. Dougherty Jr. and D. F. Fisher, "Boundary-layer transition on a 10-degree cone: Wind tunnel/flight data correlation (invited paper, 1 hour)," *AIAA 18th Aerospace Sciences Meeting*, 1980.

[63] M. Costantini, S. Hein, U. Henne, C. Klein, S. Koch, W. Sachs, L. Schojda, H. Rosemann, L. Koop, and V. Ondrus, "The effect of pressure gradient and a non-adiabatic surface on boundary layer transition investigated by means of tsp," *51st AIAA Aerospace Sciences Meeting including the New Horizons Forum and Aerospace Exposition 2013*, 2013.

[64] M. Costantini, S. Hein, U. Henne, C. Klein, S. Koch, L. Schojda, V. Ondrus, and W. Schröder, "Pressure gradient and nonadiabatic surface effects on boundary layer transition," *AIAA Journal*, vol. 54, pp. 3465–3480, 11 2016.

[65] M. Costantini, S. Risius, and C. Klein, "Surface temperature effects on boundary-layer transition at various subsonic mach numbers and streamwise pressure gradients," *Notes on Numerical Fluid Mechanics and Multidisciplinary Design*, vol. 142, pp. 155–164, 2020.

[66] F. Meyer and L. Kleiser, "Fluid dynamics of three-dimensional turbulent shear flows and transition," 1989, pp. 16-1–16-17.

[67] C. B. Cohen and E. Reshotko, "Similar solutions for the compressible laminar boundary layer with heat transfer and pressure gradient," Tech. Rep. NACA-TN-3325, 1955.

[68] E. Reshotko and I. E. Beckwith, "Compressible laminar boundary layer over a yawed infinite cylinder with heat transfer and arbitrary prandtl number," Tech. Rep. NACA-TN-3986, 1957.

[69] I. Beckwith, "Similar solutions for the compressible boundary layer on a yawed cylinder with transpiration cooling," Tech. Rep. NACA-4345, 1958.

[70] J. Ren and M. Kloker, "Instabilities in three-dimensional boundary-layer flows with a highly nonideal fluid.," *Journal of Fluid Mechanics*, vol. 951, 2022.

[71] M. Barahona, "Go/no-go report: Stability and transition of swept boundary layers in non-adiabatic wall conditions," Faculty of Aerospace Engineering, Delft University of Technology.

[72] R. Merino-Martínez, A. Rubio Carpio, L. T. Lima Pereira, S. van Herk, F. Avallone, D. Ragni, and M. Kotsonis, "Aeroacoustic design and characterization of the 3D-printed, open-jet, anechoic wind tunnel of delft university of technology," *Applied Acoustics*, vol. 170, 2020.

[73] T. Michelis, C. de Koning, and M. Kotsonis, "On the interaction of Tollmien–Schlichting waves with a wall-embedded Helmholtz resonator," *Physics of Fluids*, vol. 35, 2023.

[74] N. Lin, H. L. Reed, and W. S. Saric, "Effect of leading-edge geometry on boundary-layer receptivity to freestream sound," *Instability, Transition, and Turbulence*, pp. 421–440, 1992.

[75] *Optris PI 640i*, DS-EN2021-06-A (datasheet), Optris GmbH. [Online]. Available: `https://www.optris.com/en//download/26290/?tmstv=1695218473`.

[76] *Genauigkeit von Pt100 - Widerstandsthermometern*, Pt100 Messtechnik. [Online]. Available: `https://www.pt100.de/genauigkeit.htm`.

[77] A. J. Smits and M. V. Zaragola, "Applications of dense gases to model testing for aeronautical and hydrodynamic applications," *Measurement Science and Technology*, vol. 16, pp. 1710–1715, 2005.

[78] M. Hultmark and A. J. Smits, "Temperature corrections for constant temperature and constant current hot-wire anemometers," *Measurement Science and Technology*, vol. 21, 2010.

[79] Y. Ikeya, R. Örlü, K. Fukagata, and P. H. Alfredsson, "Towards a theoretical model of heat transfer for hot-wire anemometry close to solid walls," *International Journal of Heat and Fluid Flow*, vol. 68, pp. 248–256, 2017.

[80] P. Welch, "The use of fast fourier transform for the estimation of power spectra: A method based on time averaging over short, modified periodograms," *IEEE Transactions on audio and electroacoustics*, vol. 15, 2 1967.

A Compressible perturbation equations

x-momentum:

$$\begin{aligned}
&\left[i\rho(\alpha U+\beta W-\omega)+\frac{\mu}{Re}\left(\lambda\alpha^2+\beta^2\right)\right]\overline{u}+\left(\rho\frac{\partial U}{\partial y}-\frac{i}{Re}\frac{\partial\mu}{\partial y}\alpha\right)\overline{v}+i\alpha\overline{p}\\
&+\frac{(\lambda-1)}{Re}\mu\alpha\beta\overline{w}-\frac{1}{Re}\left\{\frac{\partial}{\partial y}\left(\mu'\frac{\partial U}{\partial y}\right)\overline{T}+\frac{\partial U}{\partial y}\frac{\partial\overline{u}}{\partial y}\right.\\
&\left.+i(\lambda-1)\mu\alpha\frac{\partial\overline{v}}{\partial y}+\mu'\frac{\partial U}{\partial y}\frac{\partial\overline{T}}{\partial y}+\mu\frac{\partial^2\overline{u}}{\partial y^2}\right\}=0
\end{aligned}\tag{39}$$

y-momentum:

$$\begin{aligned}
&\left[i\rho(\alpha U+\beta W-\omega)+\frac{\mu}{Re}\left(\alpha^2+\beta^2\right)\right]\overline{v}+\frac{\partial\overline{p}}{\partial y}\\
&-\frac{1}{Re}\left\{i(\lambda-2)\frac{\partial\mu}{\partial y}[\alpha\overline{u}+\beta\overline{w}]+i\mu'\left(\alpha\frac{\partial U}{\partial y}+\beta\frac{\partial W}{\partial y}\right)\overline{T}\right.\\
&\left.+i(\lambda-1)\mu\left[\alpha\frac{\partial\overline{u}}{\partial y}+\beta\frac{\partial\overline{w}}{\partial y}\right]+\lambda\frac{\partial\mu}{\partial y}\frac{\partial\overline{v}}{\partial y}+\lambda\mu\frac{\partial^2\overline{v}}{\partial y^2}\right\}=0
\end{aligned}\tag{40}$$

z-momentum:

$$\begin{aligned}
&\left[i\rho(\alpha U+\beta W-\omega)+\frac{\mu}{Re}\left(\alpha^2+\beta^2\right)\right]\overline{v}+\frac{\partial\overline{p}}{\partial y}\\
&-\frac{1}{Re}\left\{i(\lambda-2)\frac{\partial\mu}{\partial y}[\alpha\overline{u}+\beta\overline{w}]+i\mu'\left(\alpha\frac{\partial U}{\partial y}+\beta\frac{\partial W}{\partial y}\right)\overline{T}\right.\\
&\left.+i(\lambda-1)\mu\left[\alpha\frac{\partial\overline{u}}{\partial y}+\beta\frac{\partial\overline{w}}{\partial y}\right]+\lambda\frac{\partial\mu}{\partial y}\frac{\partial\overline{v}}{\partial y}+\lambda\mu\frac{\partial^2\overline{v}}{\partial y^2}\right\}=0
\end{aligned}\tag{41}$$

continuity:

$$i\rho(\alpha\overline{u}+\beta\overline{w})+i(\alpha U+\beta W-\omega)\overline{\rho}+\frac{\partial}{\partial y}(\rho\overline{v})=0\tag{42}$$

energy:

$$\begin{aligned}
&\left[i\rho(\alpha U+\beta W-\omega)-\frac{(\gamma-1)M^2}{Re}\mu'\left\{\left(\frac{\partial U}{\partial y}\right)^2+\left(\frac{\partial W}{\partial y}\right)^2\right\}\right.\\
&\left.+\frac{1}{Re\ \sigma}\left\{\mu\left(\alpha^2+\beta^2\right)-\frac{\partial^2\mu}{\partial y^2}\right\}\right]\overline{T}\\
&+\left[\rho\frac{\partial T}{\partial y}-\frac{2i(\gamma-1)M^2}{Re}\mu\left(\alpha\frac{\partial U}{\partial y}+\beta\frac{\partial W}{\partial y}\right)\right]\overline{v}\\
&-\mathrm{i}(\gamma-1)M^2(\alpha U+\beta W-\omega)\overline{p}\\
&-\frac{2(\gamma-1)M^2}{Re}\mu\left(\frac{\partial U}{\partial y}\frac{\partial\overline{u}}{\partial y}+\frac{\partial W}{\partial y}\frac{\partial\overline{w}}{\partial y}\right)\\
&-\frac{1}{Re\ \sigma}\left[2\frac{\partial\mu}{\partial y}\frac{\partial\overline{T}}{\partial y}+\mu\frac{\partial^2\overline{T}}{\partial y^2}\right]=0
\end{aligned}\tag{43}$$

B Images of the experimental setup

Test section overview

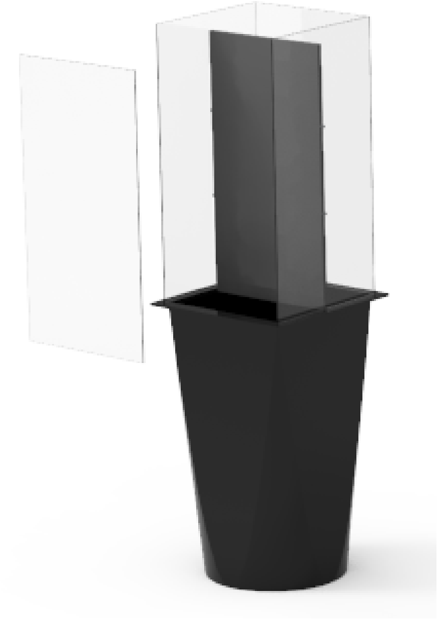

Figure B.1: Placement of the model in the test section

Figure B.2: Overview of the test section with model and measurement equipment in place

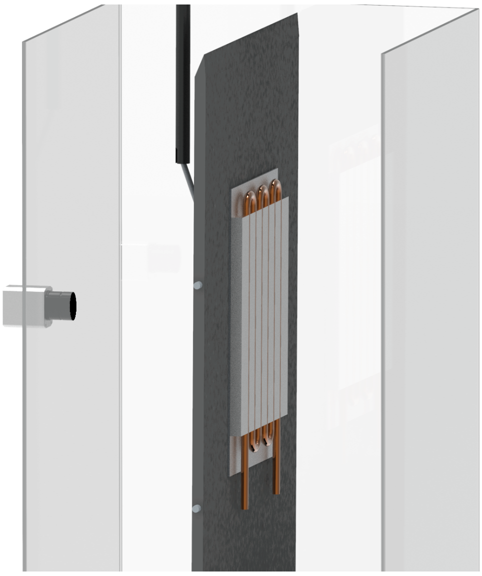

Figure B.3: Close-up of the model in test section as seen from the rear side

Figure B.4: Side view of the test section with model and measurement equipment in place

Details of the flat-plate cross section

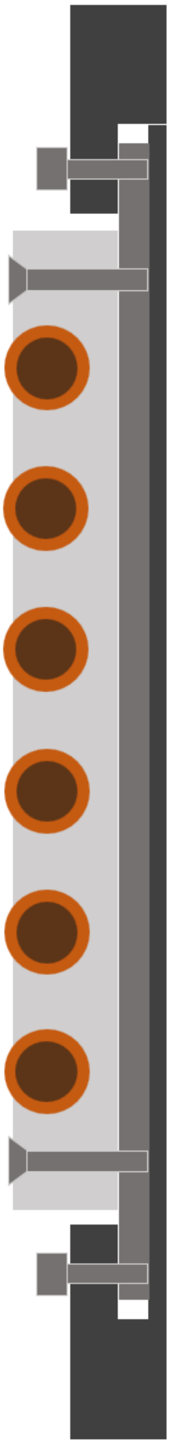

Figure B.5: Cross-sectional view of the layers of the flat-plate cooling system (axes and velocity direction analogous to figure B.6)

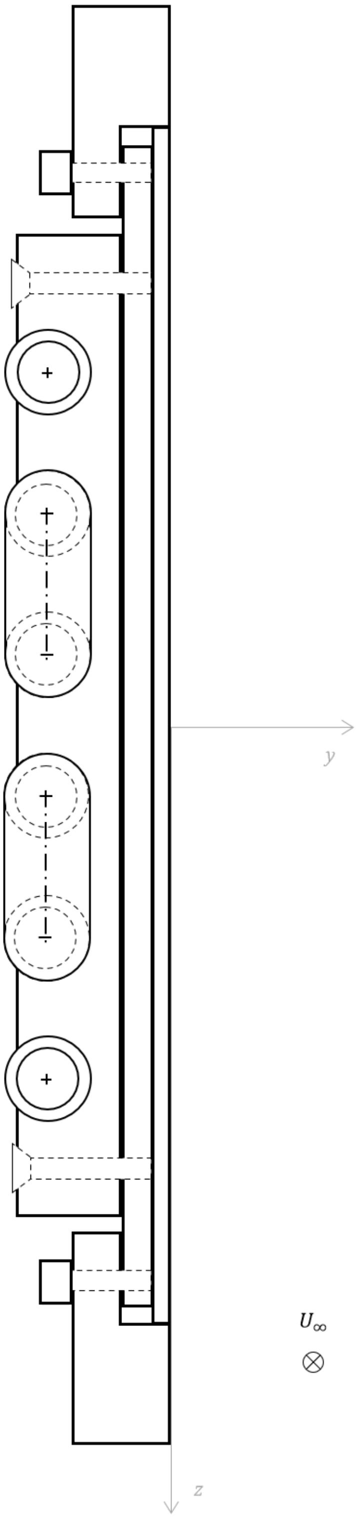

Figure B.6: Schematic top view of the flat-plate cooling system with the freestream velocity indicated

Cooling and measurement equipment

Figure B.7: The Huber Unichiller circulation cooler
© Peter Huber Kältemaschinenbau SE

Figure B.8: The Optris PI 640i infrared camera
© Optris GmbH

Figure B.9: The TSI IFA-300 constant temperature anemometer
© Kenelec Scientific Pty Ltd

Calibration set-up and data visualization

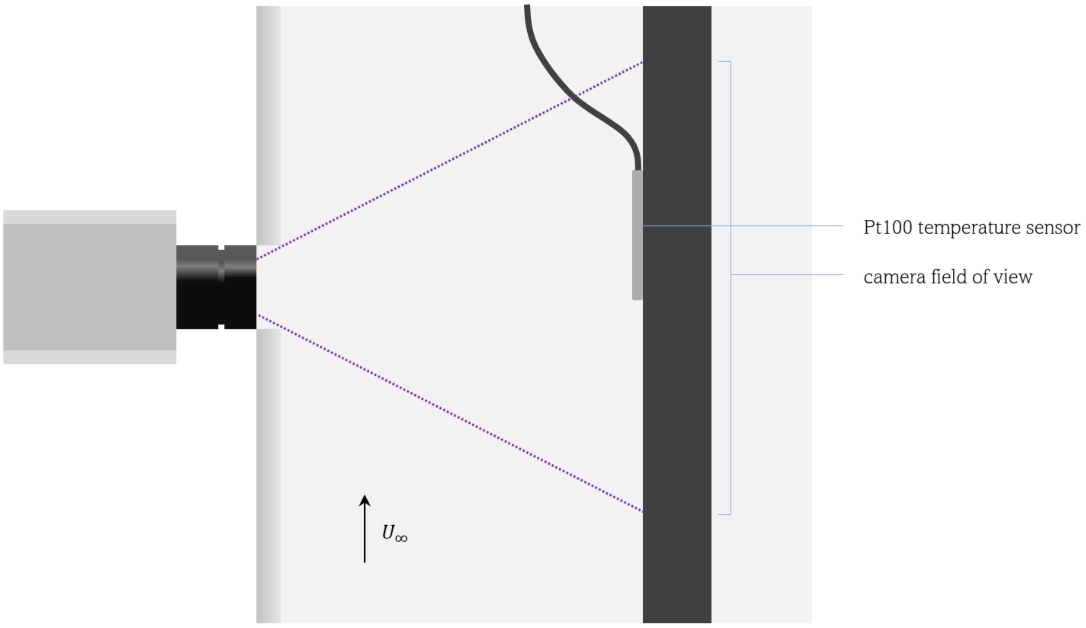

Figure B.10: Setup for the calibration procedure of the infrared camera (left). The Pt100 sensor takes on the temperature of the adjacent flat plate in a thermal equilibrium. Its temperature is registered by both the infrared camera and the Pt100 device itself

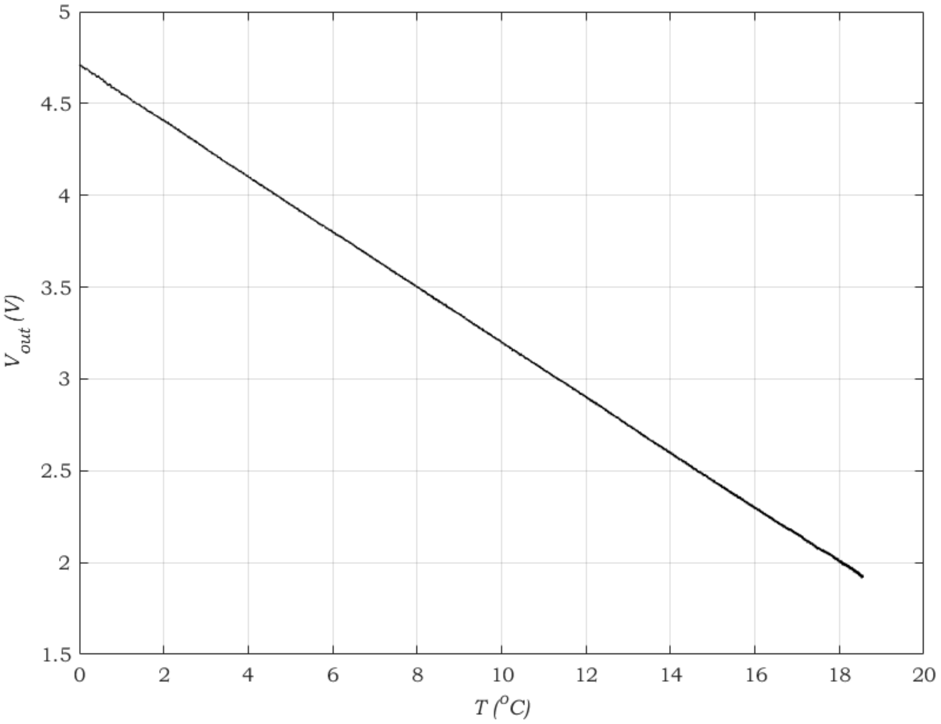

Figure B.11: Voltage output of the CCA plotted against temperatures simultaneously recorded by a Pt100 sensor. The maximum error in T is 3.0%; the mean error is 1.3%

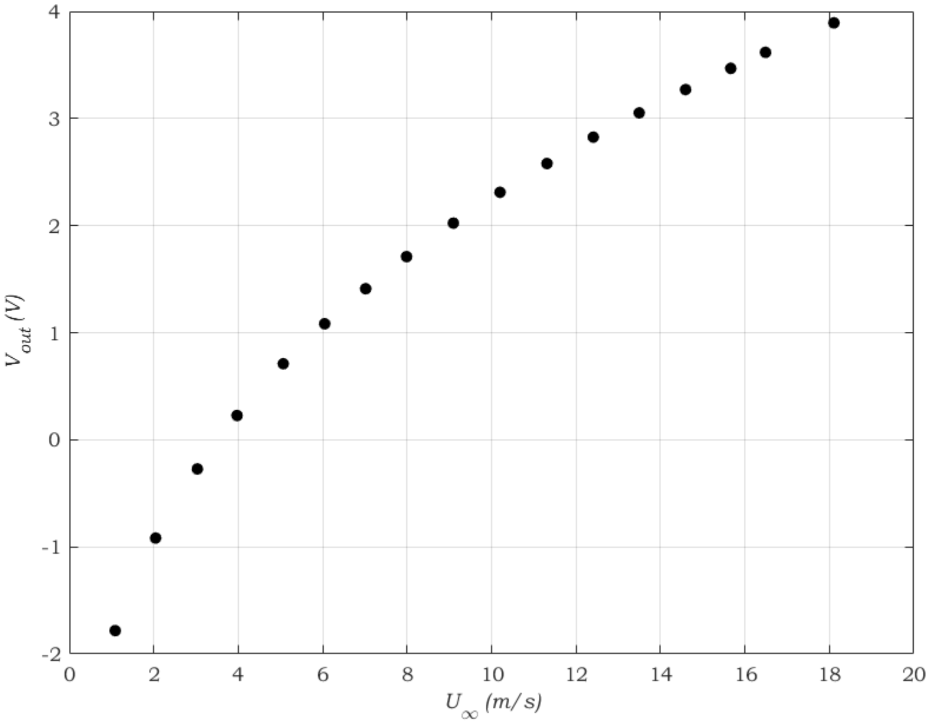

(a) Voltage output of the CTA at corresponding tunnel setting velocities, measured in the freestream

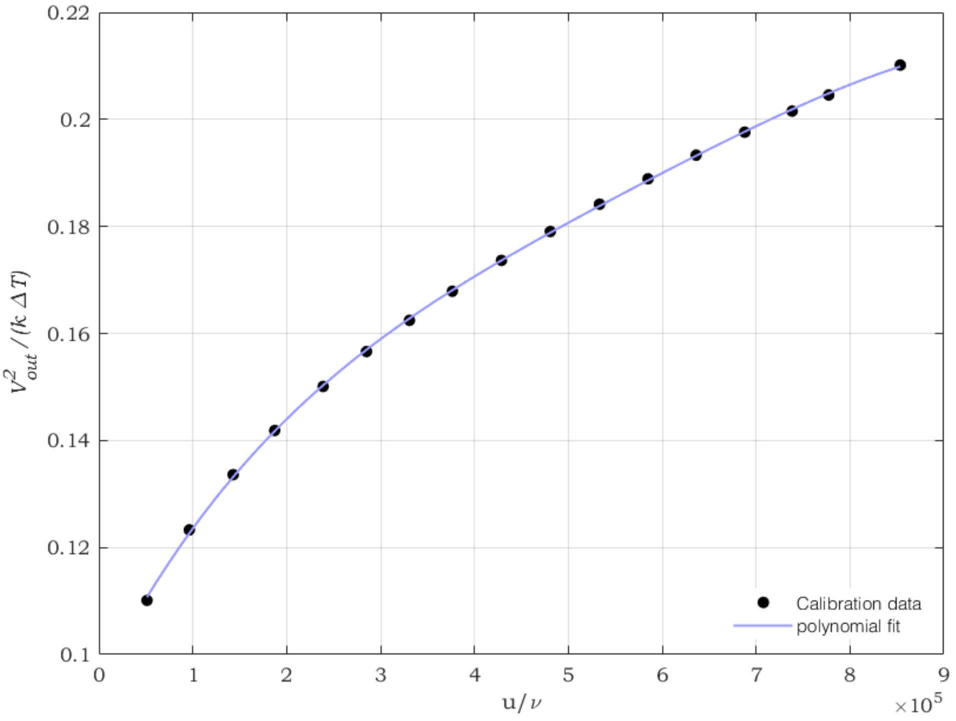

(b) CTA calibration data points fitted to a fourth-order polynomial, axis quantities from [78] and air property calculation method from [77]. The maximum error in u/ν is 2.7%; the mean error is 0.70%

Figure B.12: CTA calibration data

C Constant-current anemometer manual (short version)

This instruction is a short version of the DISA 55M manual written during the research, to be used when operating the machine as a constant-current anemometer (CCA).

Working principle of the CCA

The resistance of the anemometer's tungsten wire changes with its temperature. When a constant current is applied to the circuit, the output voltage will change with the total circuit resistance. If all other resistances are kept constant, the output voltage is thus a direct measure of the wire temperature.

Conversion formulas

In the linear range, the probe resistance changes with temperature according to:

$$R_p - R_{20} = \alpha_{20}(T_p - T_{\text{ref}}) \tag{44}$$

with

R_p: probe resistance [Ω]
R_{20}: probe resistance at 20 ^{o}C [Ω]
α_{20}: temperature coefficient at 20 ^{o}C [^{o}C^{-1}]
T_p: probe temperature [^{o}C]
T_{ref}: reference temperature [^{o}C]

For commonly used wires, a linear region extends from approximately 0^{o}C to 100^{o}C. Within this region, the probe resistance and temperature coefficient remain nearly constant. Their standard values are taken at 20^{o}C. Therefore, the smallest error occurs when the reference temperature is chosen at 20^{o}C. The temperature coefficient α_{20} is a material property (circa .0036 ^{o}C^{-1} for the tungsten wire). It is recommended to (re-)establish the probe resistance R_{20} before each experiment.

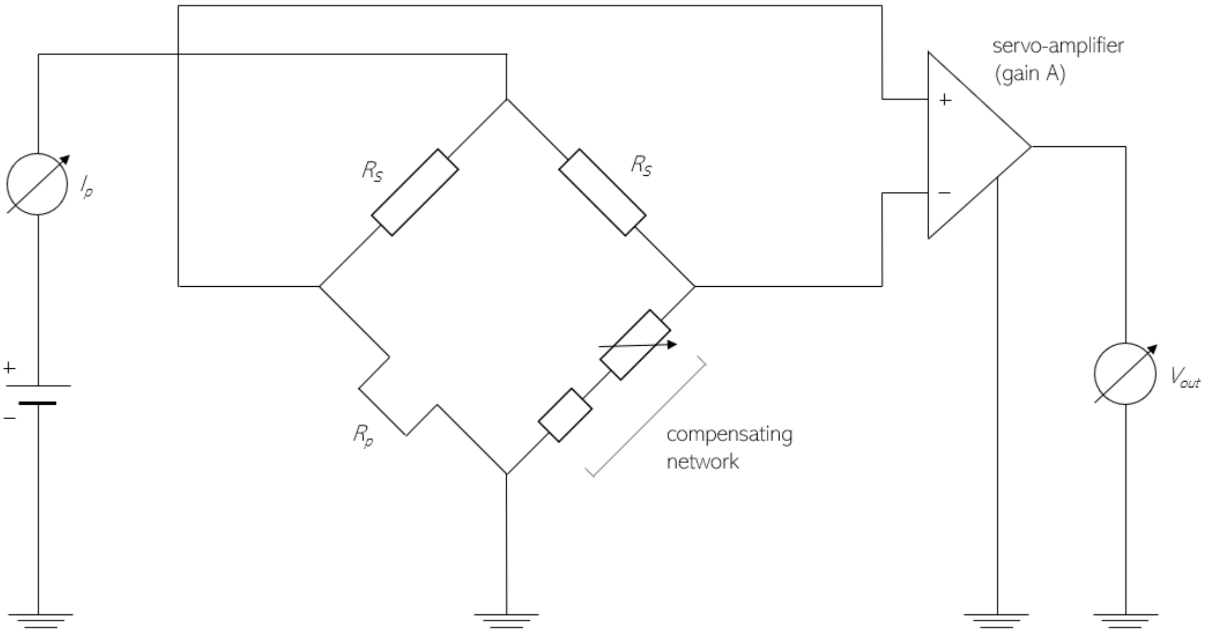

Figure C.1: Simplified electrical circuit of the DISA 55M anemometer in constant current mode

Figure C.1 shows the relevant components of the CCA circuit. From this circuit, it can be derived that the total resistance in the left bridge arm equals:

$$R_{\text{l.a.}} = \frac{1}{\frac{1}{R_p}\frac{1}{R_S}} = \frac{R_p R_S}{R_p + R_S}, \tag{45}$$

where R_S represents the (constant) ratio resistance on the upper side of the bridge. Combining (45) with Ohm's law ($V = RI$) gives the CCA's output voltage step per ^{o}C:

$$\Delta V_{\text{out}} = \alpha_{20} I_p A \frac{R_p R_S}{R_p + R_S} \tag{46}$$

with

I_p: probe current [A]
A: amplifier gain [-]

When inserted in (44), the measured temperature is found through:

$$T_p = T_{\text{ref}} + \frac{V_{\text{out}} - V_{\text{ref}}}{\Delta V_{\text{out}}} \tag{47}$$

The current is kept constant throughout the anemometer circuit, so that the probe current Ip is a constant. The amplifier gain, on the other hand, is subject to high uncertainty: it depends on both the input signal frequency and the output voltage magnitude. It is therefore convenient to select a fixed gain setting for which the output voltage resolution is acceptable in the entire temperature range of the experiment. The setting and its magnitude are found by acquiring two data points featuring temperature and output voltage, while all other variables remain unchanged. The two temperature points are chosen close to respectively the minimum and maximum temperature to be measured in the experiment.

Temperature measurements using the DISA 55M system

Initial settings

Plug the power cable in the socket and check the initial settings before flipping the power switch (fig. C.2):

SQUARE: OFF
HF FILTER: 1
VOLTS: 10
FUNCTION: STD. BY
GAIN: 1
Decade resistance: 00.00
PROBE CURRENT: OFF
If all settings are set accordingly, turn on the power switch at the back of the housing.

Lead resistance compensation

Connect the probe cable to the PROBE socket and install the shorting probe (55H30). Set the FUNCTION switch to RES. MEAS. Turn the ZERO OHMS switch so that the meter is on the red mark. Replace the shorting probe with the wire probe (55P11).

Figure C.2: Initial settings for the DISA 55M constant-current anemometer

Probe current selection

In order to find the highest current for which the anemometer is not sensitive to the flow velocity, the sensor resistance is measured for several probe current values. This is done by applying a certain current, selecting the highest possible gain (NB: voltage gain in dB) and balancing the circuit by means of the decade resistance. Steps are as follows:

Place the probe in a flow (in the velocity range of the experiment). Move the following switches:
FUNCTION: OPERATE
Meter switch (VOLTS): 3
PROBE CURRENT: CURRENT ADJ.

Adjust the current potentiometer (CURRENT ADJ.) so that the meter is on 3 mA. Move the following switches:
PROBE CURRENT: OFF
Meter switch (VOLTS): 10
GAIN: 11

Adjust the voltage potentiometer (DC OUTPUT ADJ.) so that the meter is on the red scale mark. Set the PROBE CURRENT switch to ON. Turn the decades so that the meter is on the red scale mark again and note the sensor resistance found. For better accuracy, the latter can be repeated for PROBE CURRENT: OFF. Repeat the process for different velocities and decreasing currents, until the error in sensor resistance becomes impermissibly large.

Output voltage and gain adjustment

During the experiment, the output voltage can be adjusted from the default setting to give a convenient output value in the following cases:

- measurements of $\Delta T > 0$ in the right-hand half of the meter scale;
- measurements of $\Delta T < 0$ in the left-hand half of the meter scale;
- measurements of both $\Delta T > 0$ and $\Delta T < 0$ close to the centre of the meter scale.

The decade setting should be altered with the voltage output. The gain can be adjusted separately to increase sensitivity. A high-gain switch can be found on the top-side of the CCA unit and is operated with a screwdriver.

D Supplementary images of the results

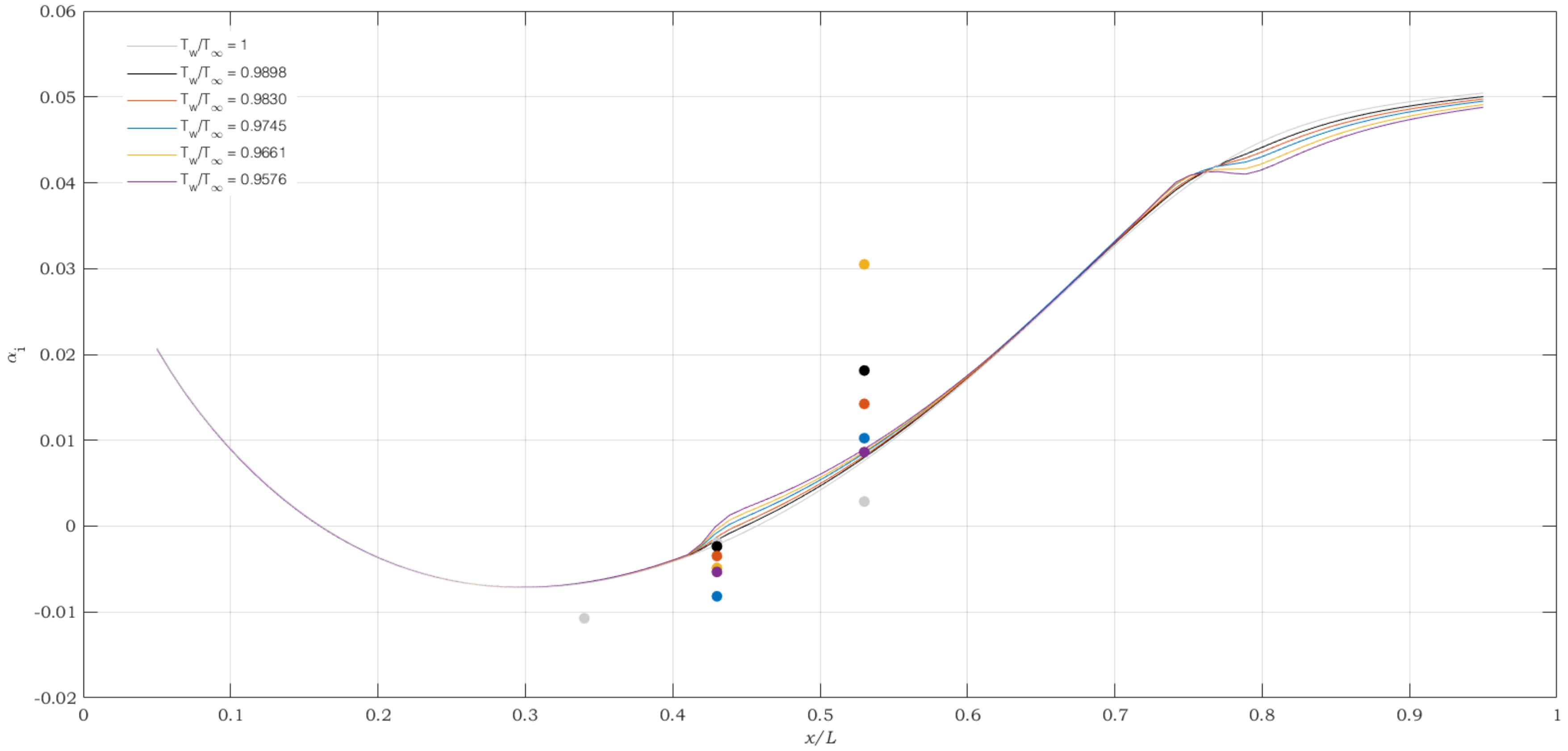

Figure D.1: Perturbation amplitude growth rates as predicted by the CBL/CLST solver compared to the growth rates found by local linear stability analysis of the experimental data (dots)

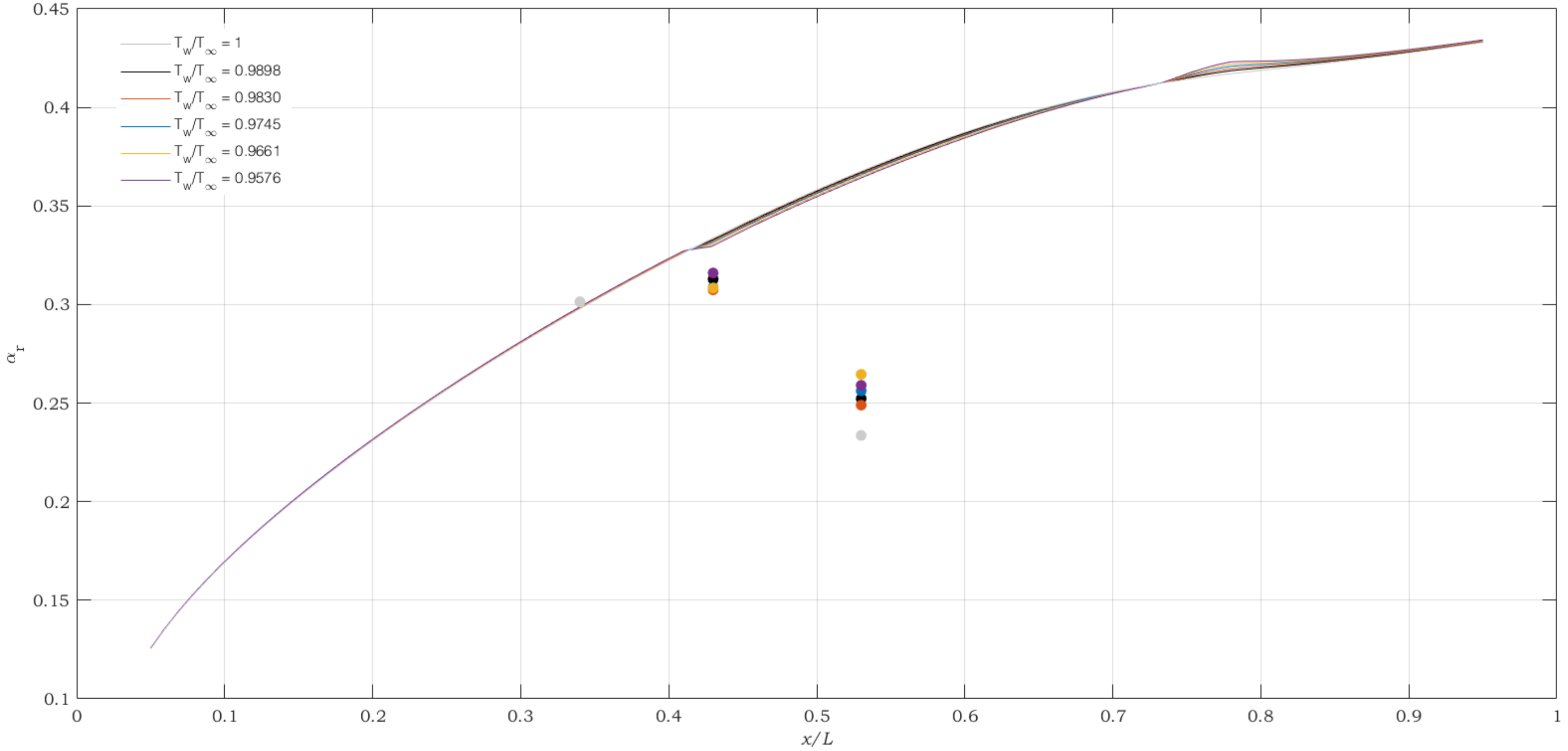

Figure D.2: Perturbation wavenumbers as predicted by the CBL/CLST solver compared to the wavenumbers found by local linear stability analysis of the experimental data (dots)

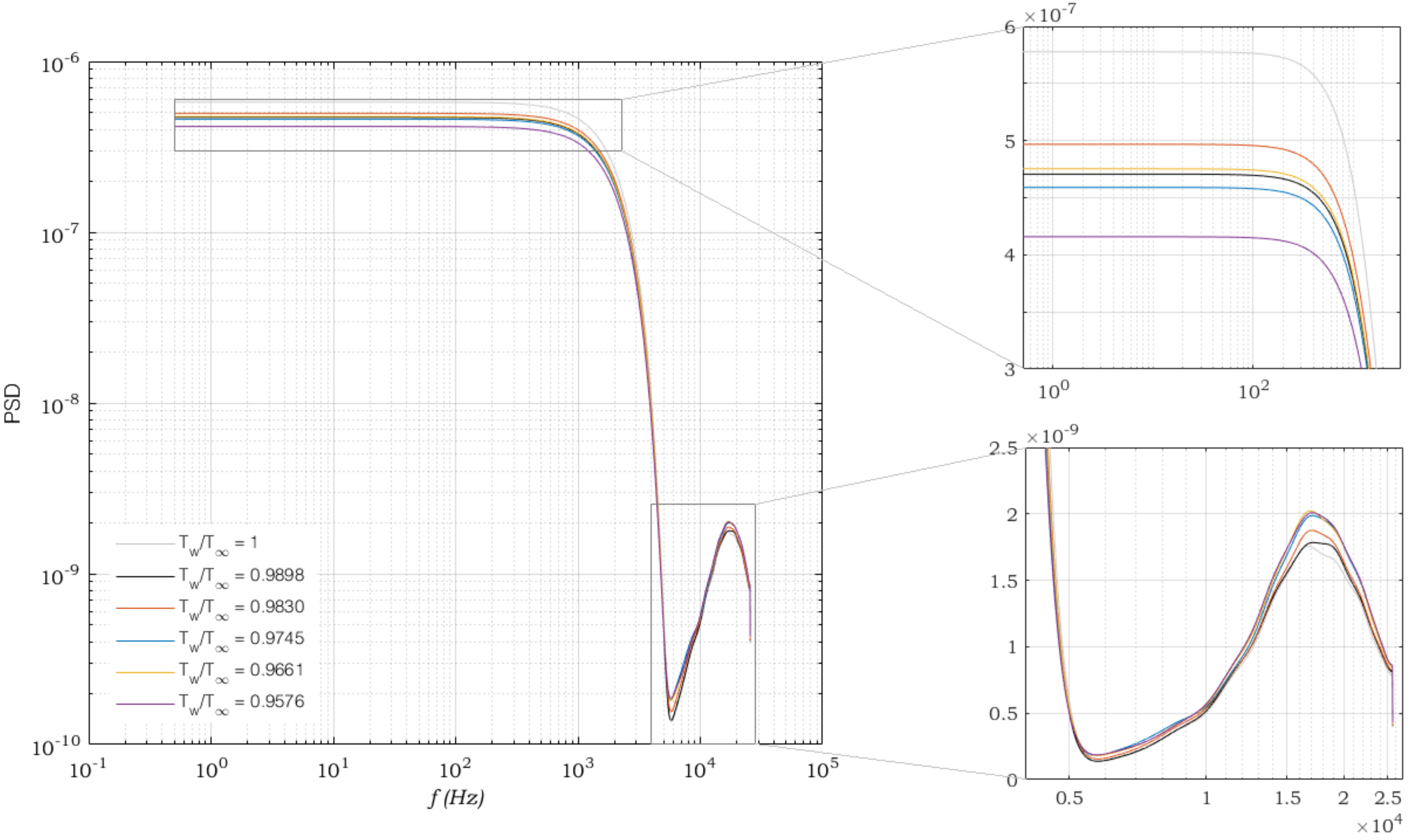

Figure D.3: Spectral density estimates of the measured velocity data x = 430 mm, at the height of the T–wave

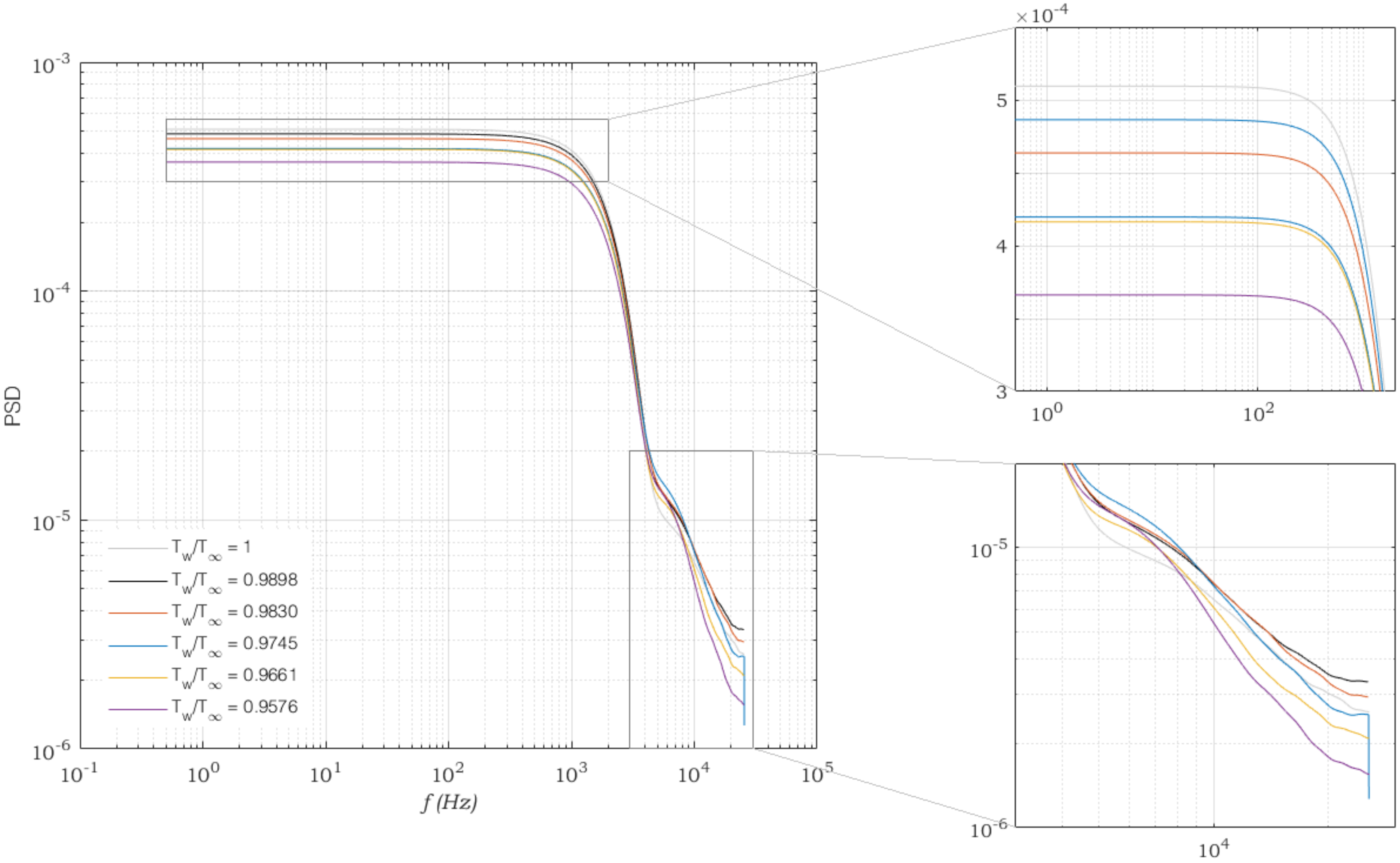

Figure D.4: Spectral density estimates of the measured velocity data x = 530 mm, at the height of the largest velocity fluctuation

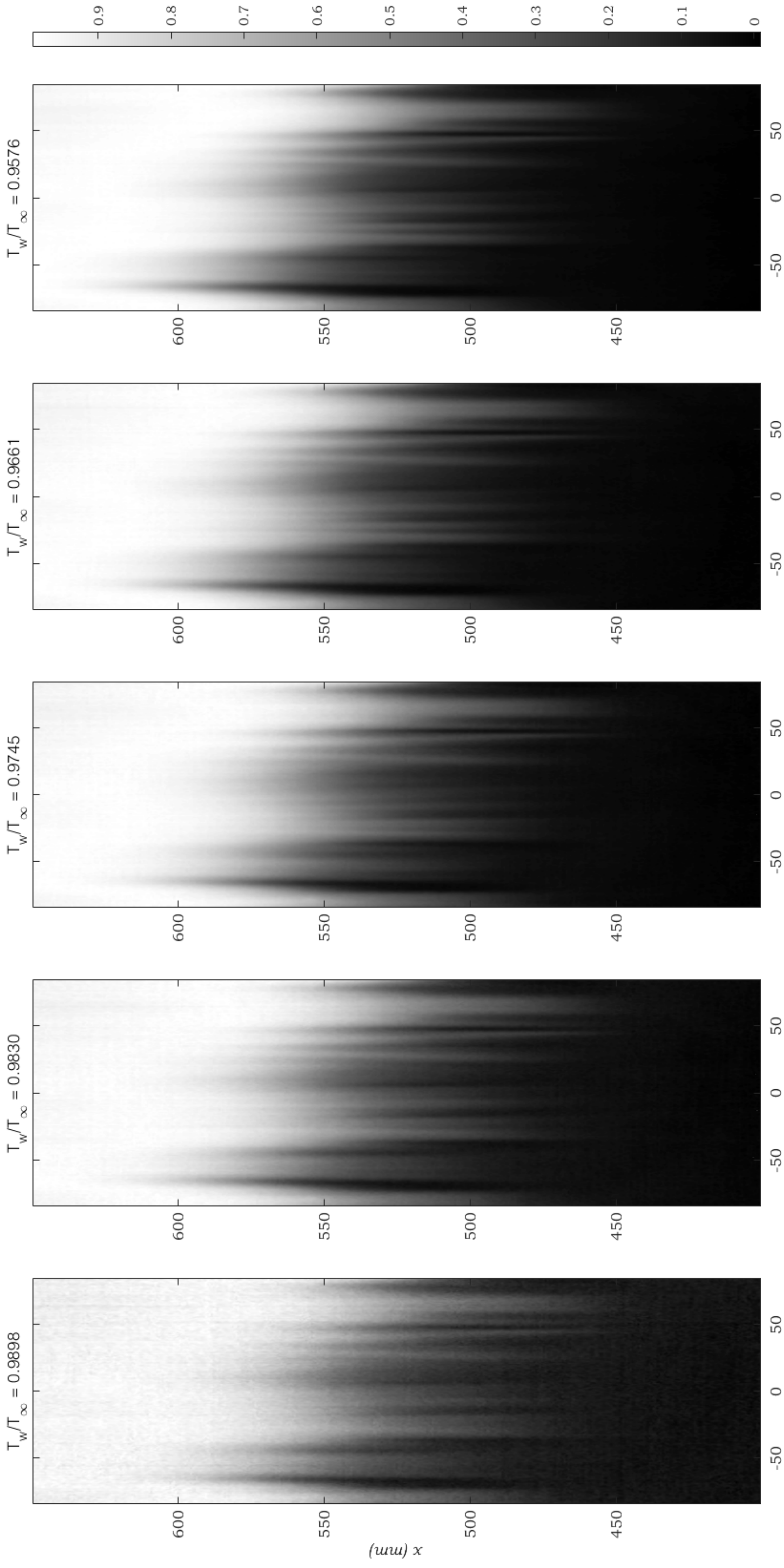
T_w/T_∞ = 0.9898
T_w/T_∞ = 0.9830
T_w/T_∞ = 0.9745
T_w/T_∞ = 0.9661
T_w/T_∞ = 0.9576
x (mm)
600
550
500
450
z (mm)
-50
0
50
0.9
0.8
0.7
0.6
0.5
0.4
0.3
0.2
0.1
0

f = 280 Hz

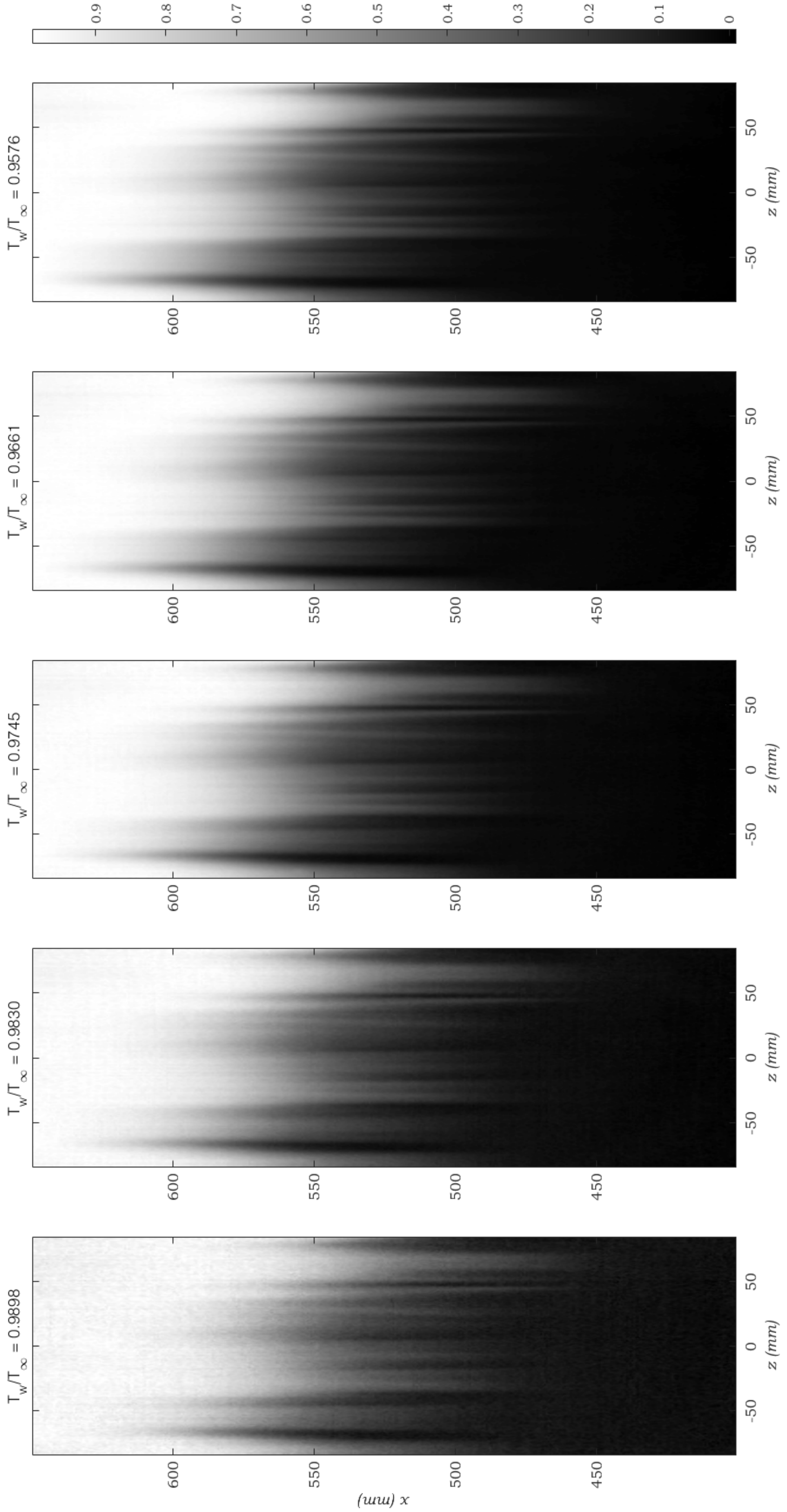
T_w/T_∞ = 0.9898
T_w/T_∞ = 0.9830
T_w/T_∞ = 0.9745
T_w/T_∞ = 0.9661
T_w/T_∞ = 0.9576
x (mm)
600
550
500
450
z (mm)
-50
0
50
0.9
0.8
0.7
0.6
0.5
0.4
0.3
0.2
0.1
0

$f = 285$ Hz

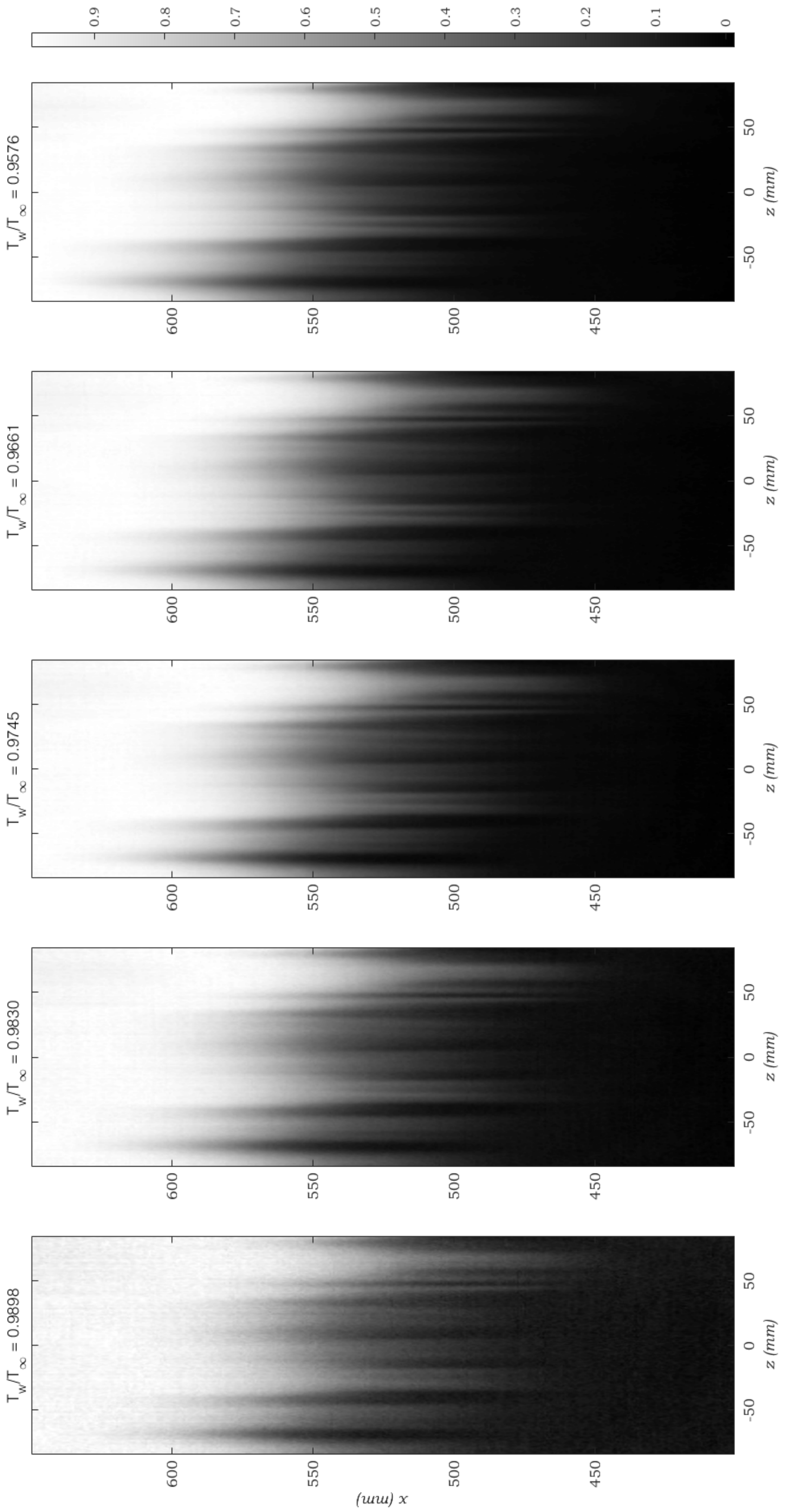
T_w/T_∞ = 0.9898
T_w/T_∞ = 0.9830
T_w/T_∞ = 0.9745
T_w/T_∞ = 0.9661
T_w/T_∞ = 0.9576
x (mm)
600
550
500
450
z (mm)
-50
0
50
0.9
0.8
0.7
0.6
0.5
0.4
0.3
0.2
0.1
0

f = 290 Hz

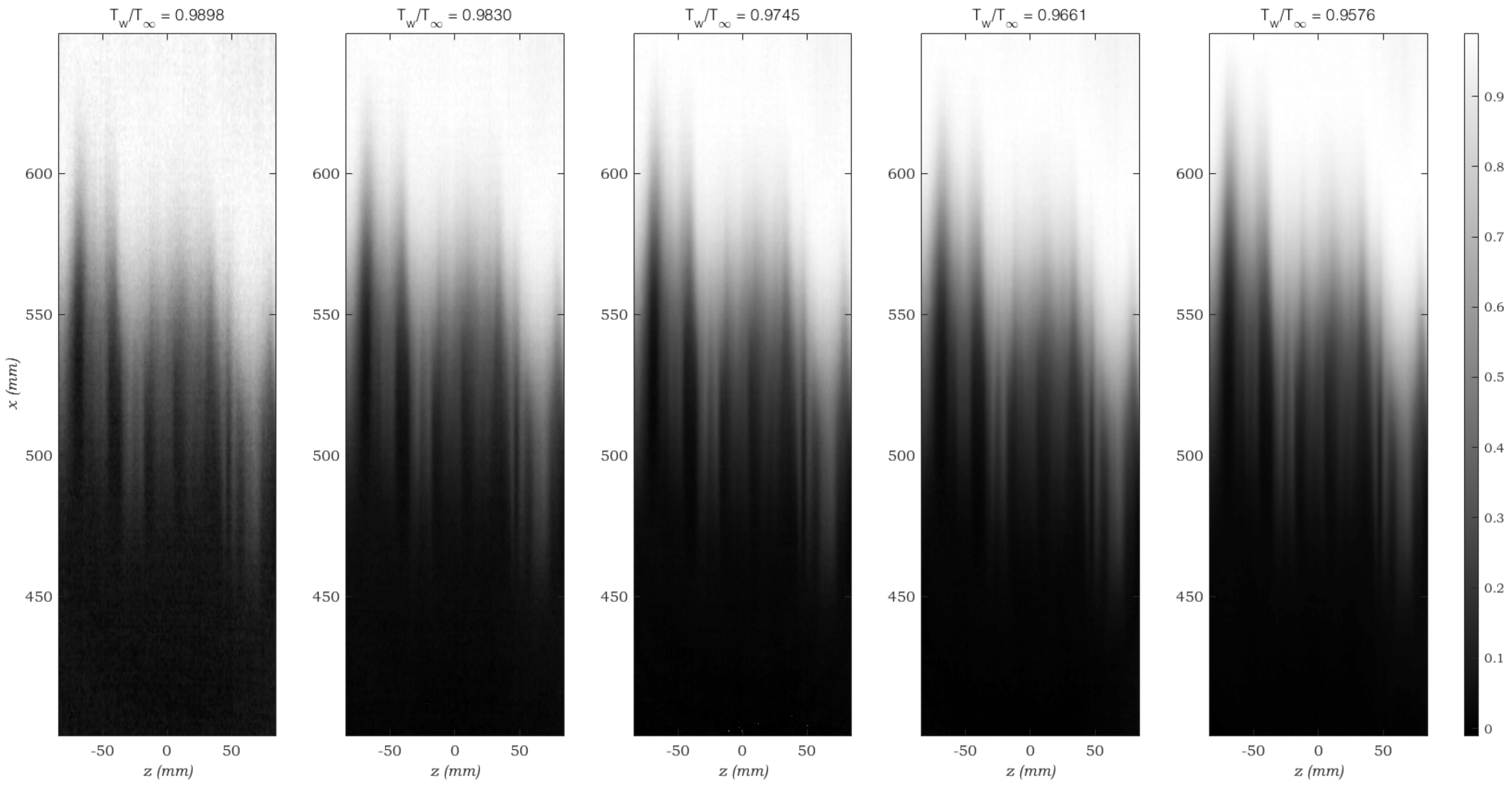
T_w/T_∞ = 0.9898
T_w/T_∞ = 0.9830
T_w/T_∞ = 0.9745
T_w/T_∞ = 0.9661
T_w/T_∞ = 0.9576
x (mm)
600
550
500
450
z (mm)
-50
0
50
0.9
0.8
0.7
0.6
0.5
0.4
0.3
0.2
0.1
0

f = 295 Hz

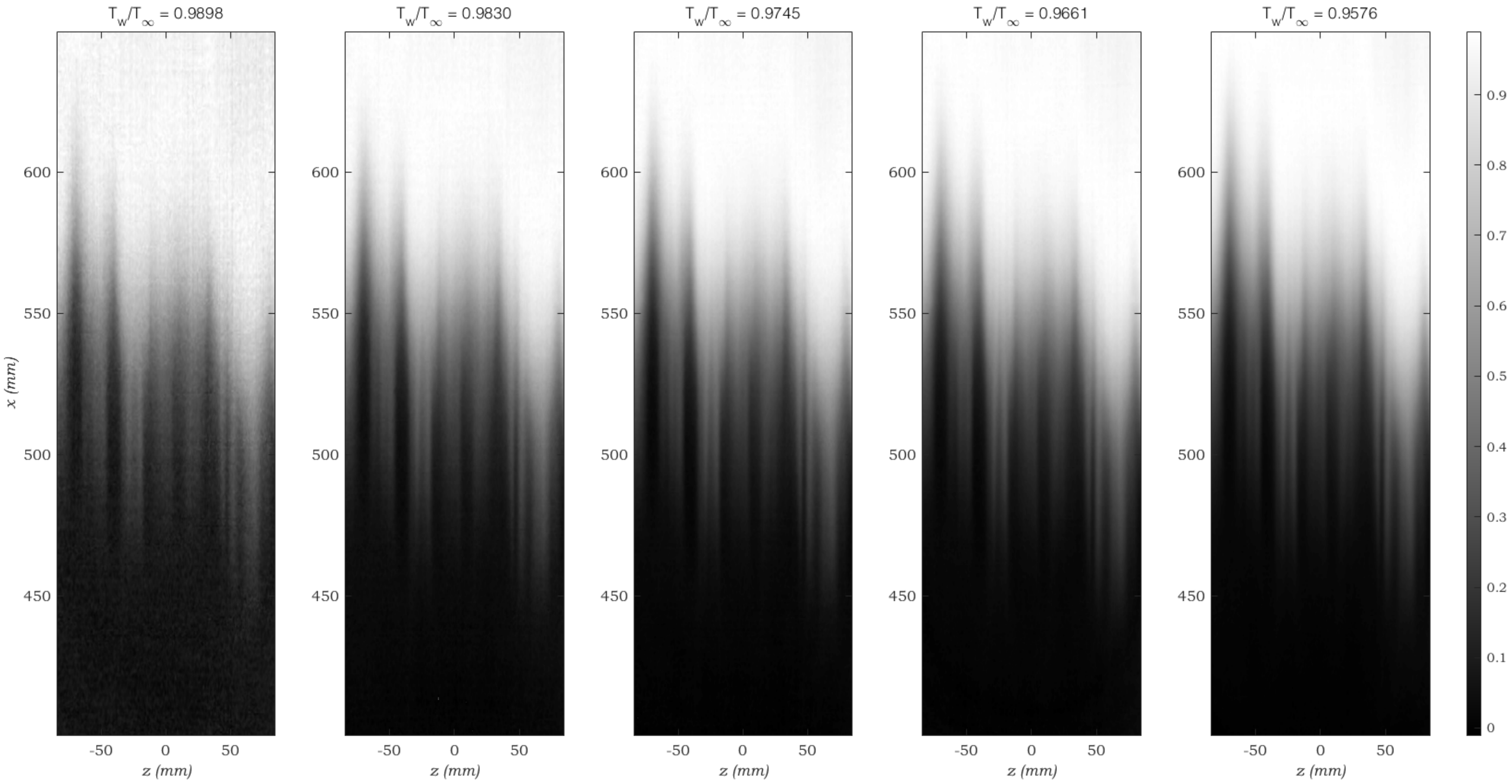
$T_w/T_\infty = 0.9898$
$T_w/T_\infty = 0.9830$
$T_w/T_\infty = 0.9745$
$T_w/T_\infty = 0.9661$
$T_w/T_\infty = 0.9576$
x (mm)
600
550
500
450
z (mm)
-50
0
50
0.9
0.8
0.7
0.6
0.5
0.4
0.3
0.2
0.1
0

f = 300 Hz

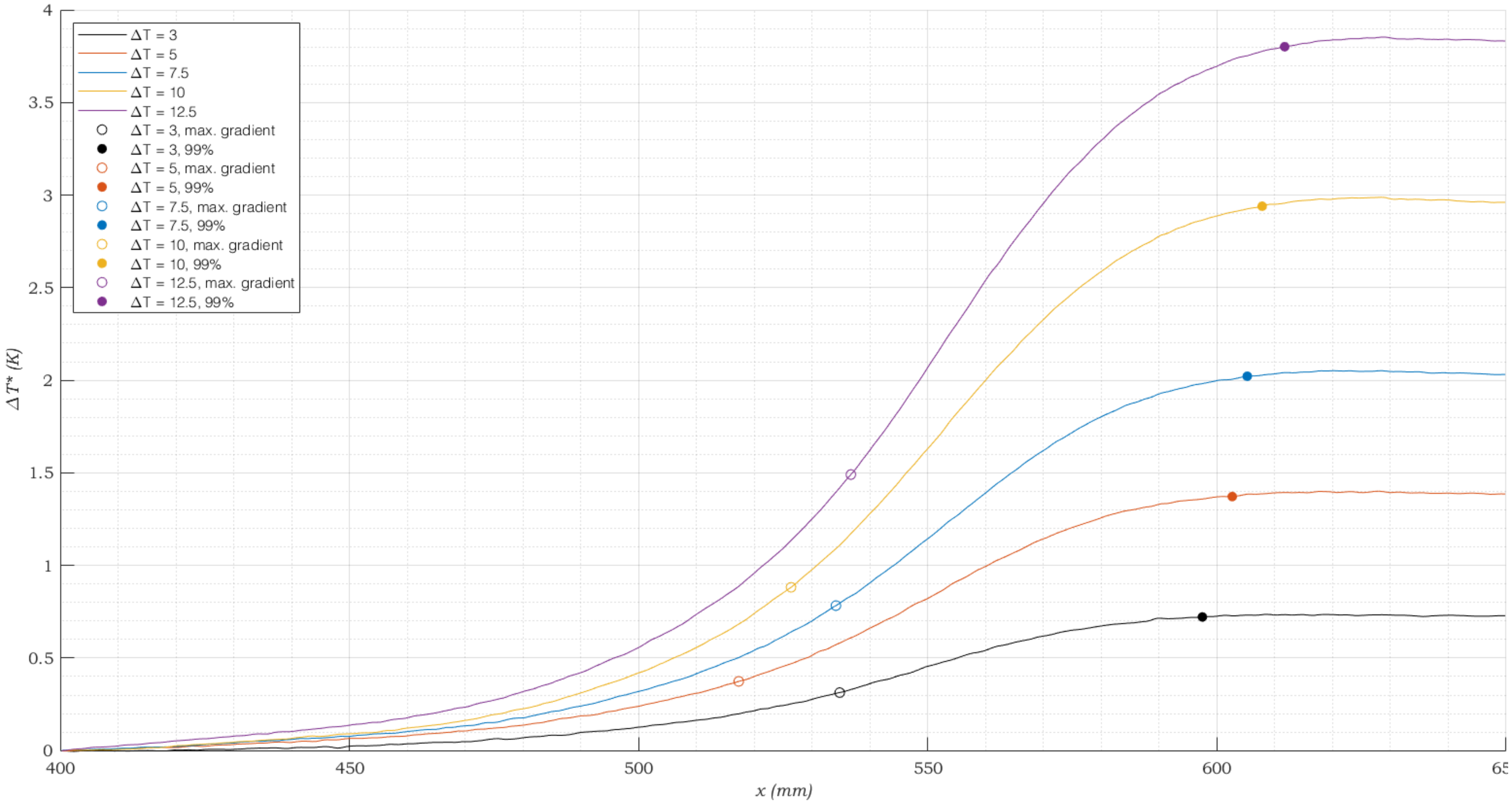
4
3.5
3
2.5
2
1.5
1
0.5
0
ΔT^* (K)
400
450
500
550
600
65
x (mm)
ΔT = 3
ΔT = 5
ΔT = 7.5
ΔT = 10
ΔT = 12.5
ΔT = 3, max. gradient
ΔT = 3, 99%
ΔT = 5, max. gradient
ΔT = 5, 99%
ΔT = 7.5, max. gradient
ΔT = 7.5, 99%
ΔT = 10, max. gradient
ΔT = 10, 99%
ΔT = 12.5, max. gradient
ΔT = 12.5, 99%

f = 280 Hz

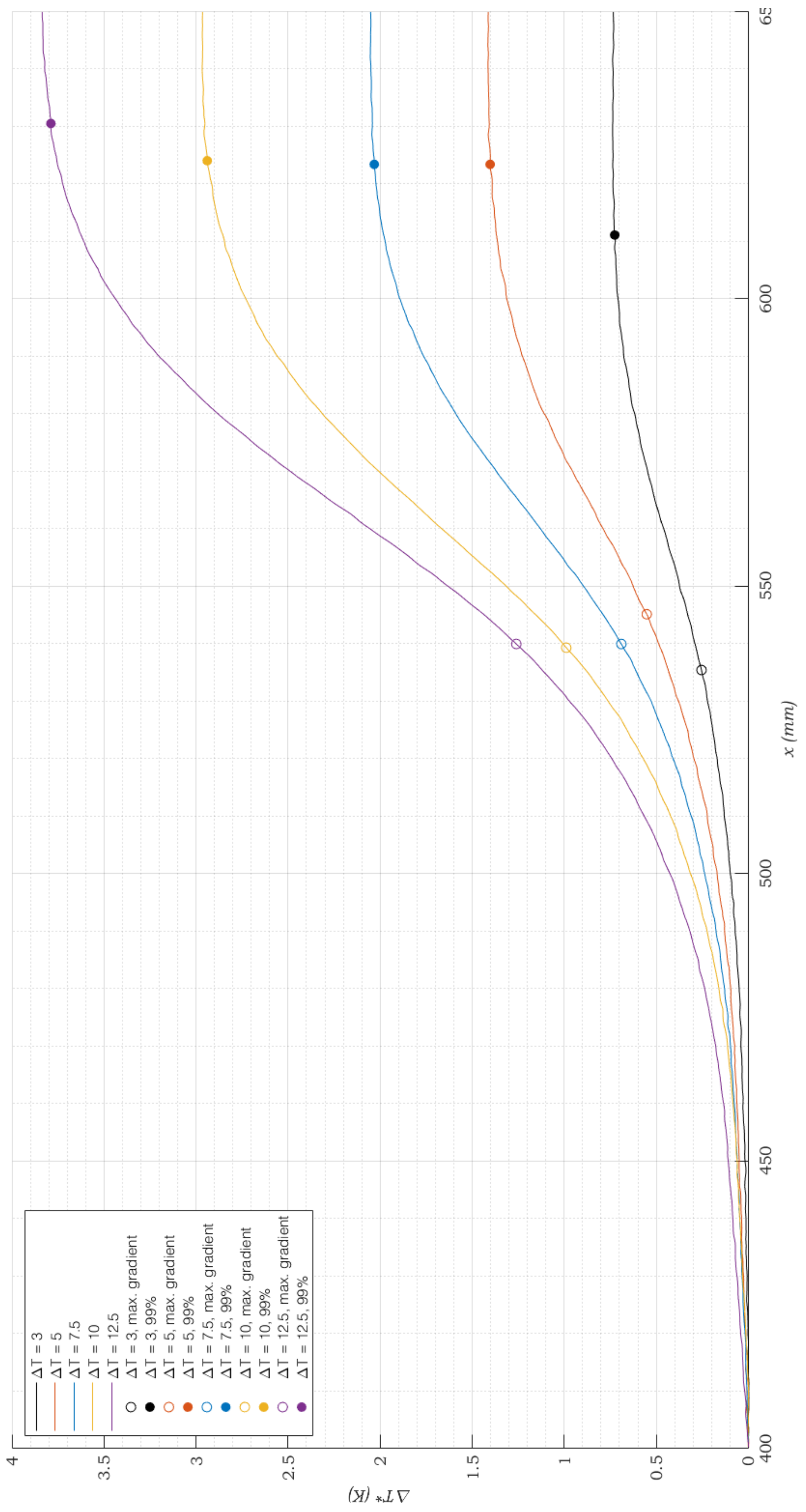

ΔT = 3
ΔT = 5
ΔT = 7.5
ΔT = 10
ΔT = 12.5
ΔT = 3, max. gradient
ΔT = 3, 99%
ΔT = 5, max. gradient
ΔT = 5, 99%
ΔT = 7.5, max. gradient
ΔT = 7.5, 99%
ΔT = 10, max. gradient
ΔT = 10, 99%
ΔT = 12.5, max. gradient
ΔT = 12.5, 99%
ΔT* (K)
0
0.5
1
1.5
2
2.5
3
3.5
4
x (mm)
400
450
500
550
600
65

f = 285 Hz

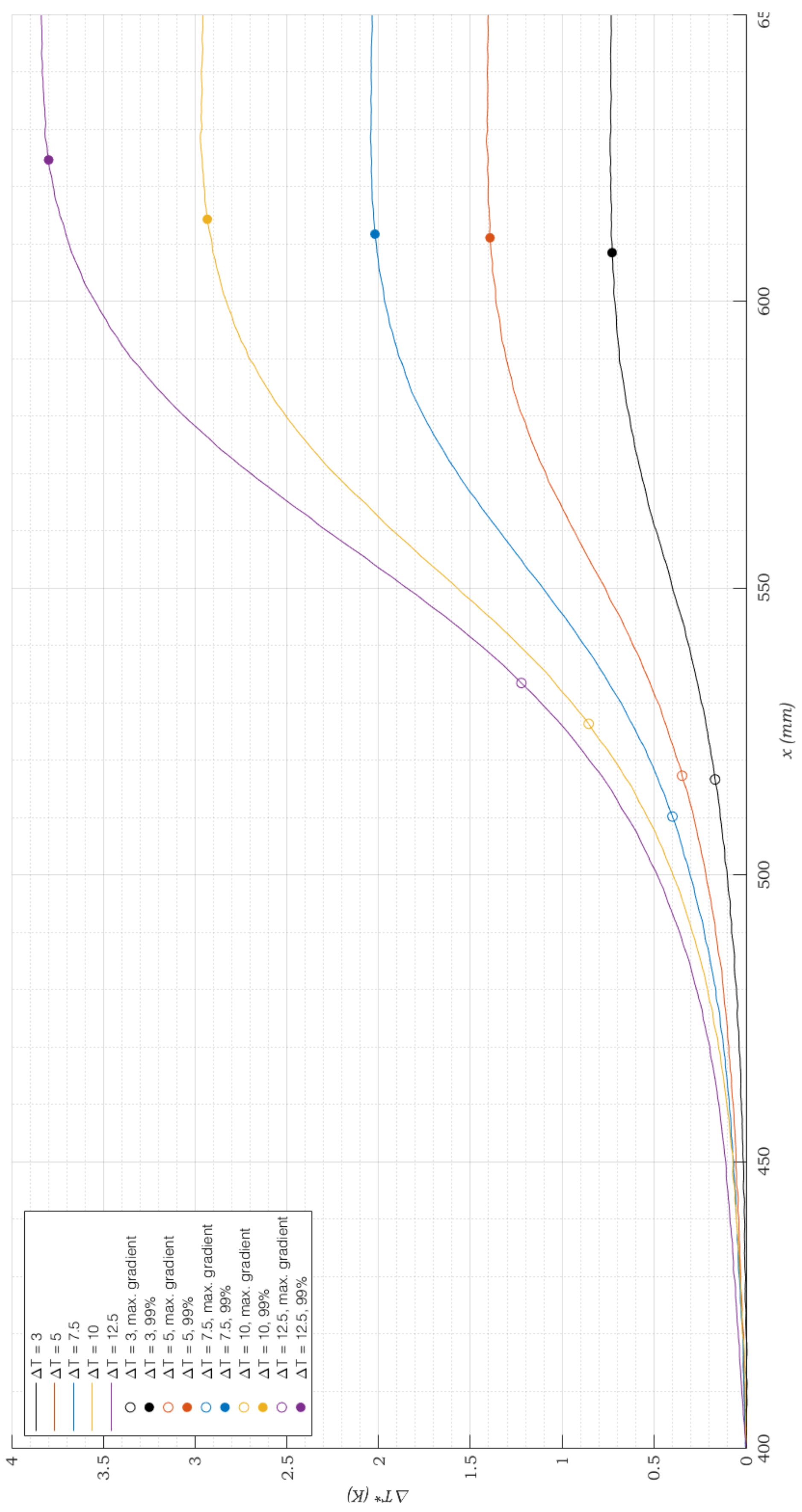
ΔT = 3
ΔT = 5
ΔT = 7.5
ΔT = 10
ΔT = 12.5
○ ΔT = 3, max. gradient
● ΔT = 3, 99%
○ ΔT = 5, max. gradient
● ΔT = 5, 99%
○ ΔT = 7.5, max. gradient
● ΔT = 7.5, 99%
○ ΔT = 10, max. gradient
● ΔT = 10, 99%
○ ΔT = 12.5, max. gradient
● ΔT = 12.5, 99%
ΔT^* (K)
0
0.5
1
1.5
2
2.5
3
3.5
4
x (mm)
400
450
500
550
600
65

f = 290 Hz

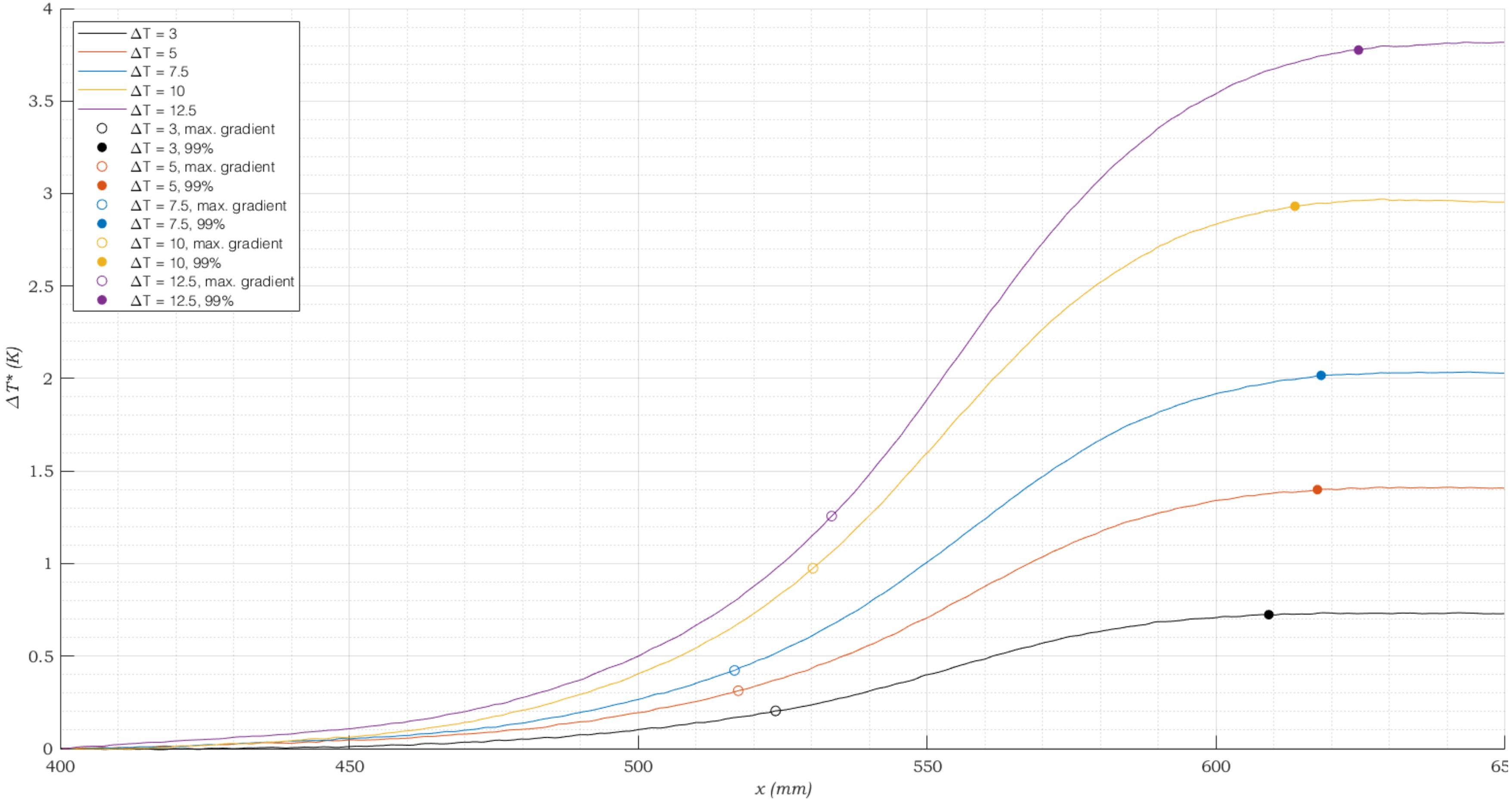
4
3.5
3
2.5
2
1.5
1
0.5
0
ΔT* (K)
400
450
500
550
600
65
x (mm)
ΔT = 3
ΔT = 5
ΔT = 7.5
ΔT = 10
ΔT = 12.5
ΔT = 3, max. gradient
ΔT = 3, 99%
ΔT = 5, max. gradient
ΔT = 5, 99%
ΔT = 7.5, max. gradient
ΔT = 7.5, 99%
ΔT = 10, max. gradient
ΔT = 10, 99%
ΔT = 12.5, max. gradient
ΔT = 12.5, 99%

f = 295 Hz

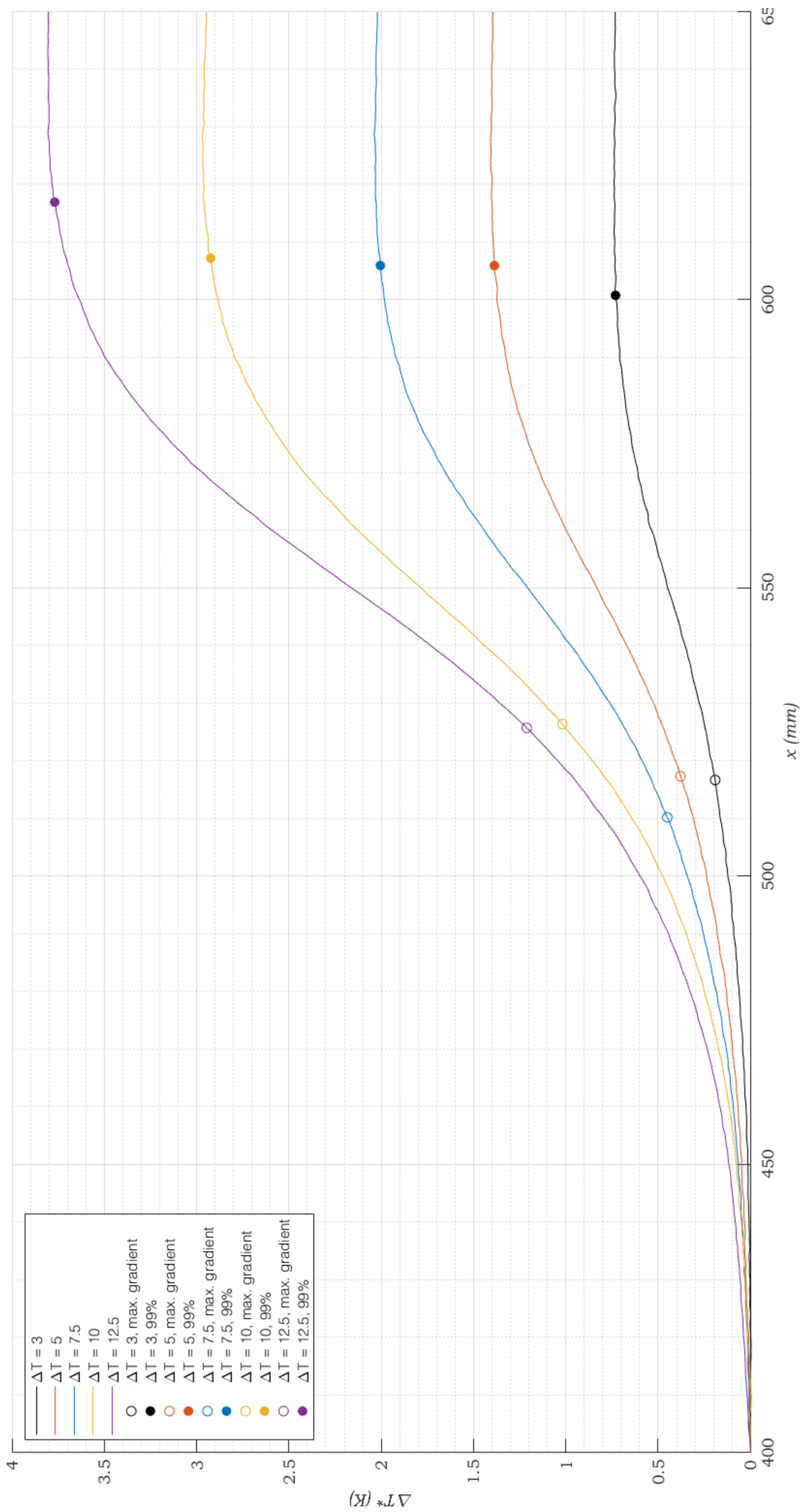
ΔT = 3
ΔT = 5
ΔT = 7.5
ΔT = 10
ΔT = 12.5
ΔT = 3, max. gradient
ΔT = 3, 99%
ΔT = 5, max. gradient
ΔT = 5, 99%
ΔT = 7.5, max. gradient
ΔT = 7.5, 99%
ΔT = 10, max. gradient
ΔT = 10, 99%
ΔT = 12.5, max. gradient
ΔT = 12.5, 99%
ΔT* (K)
0
0.5
1
1.5
2
2.5
3
3.5
4
x (mm)
400
450
500
550
600
65

f = 300 Hz

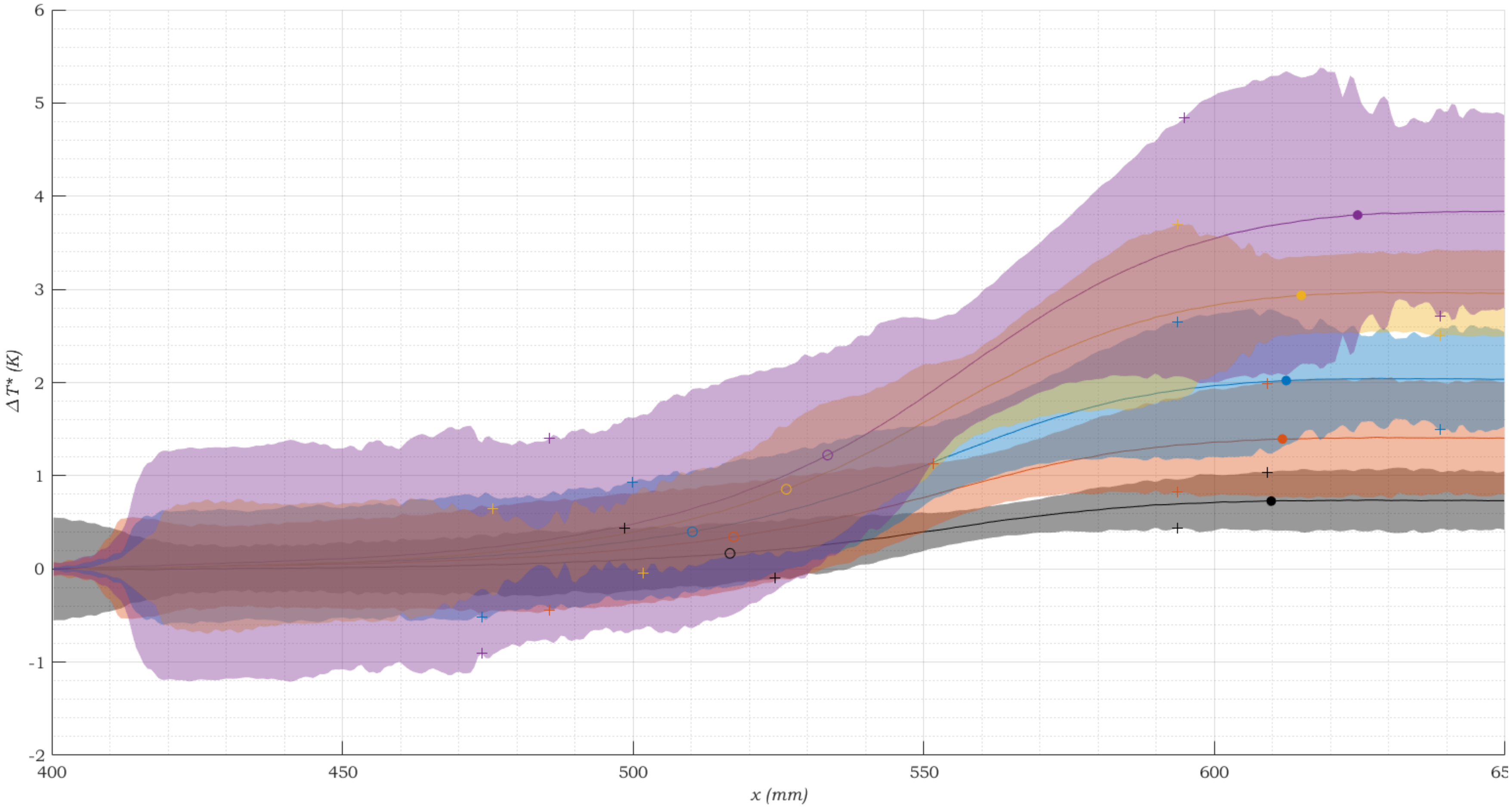

f = 290 Hz, including unit standard deviations